2013

Study Of Inas/Ga(In)Sb And Inasn/Ga(In)Sb Superlattices By Mbe For Very Long Wavelength Infrared Photodetectors

Adam S. Bowen
North Carolina Agricultural and Technical State University

Study of InAs/Ga(In)Sb and InAsN/Ga(In)Sb Superlattices by MBE for Very Long Wavelength Infrared Photodetectors

Adam S. Bowen

North Carolina A&T State University

A dissertation submitted to the graduate faculty

in partial fulfillment of the requirements for the degree of

DOCTOR OF PHILOSOPHY

Department: Electrical and Computer Engineering

Major: Electrical Engineering

Major Professor: Dr. Shanthi Iyer

Greensboro, North Carolina

2013

School of Graduate Studies
North Carolina Agricultural and Technical State University
This is to certify that the Doctoral Dissertation of

Adam S. Bowen

has met the dissertation requirements of
North Carolina Agricultural and Technical State University

Greensboro, North Carolina
2013

Approved by:

Dr. Shanthi Iyer Major Professor	Dr. L.R. Ram-Mohan Committee Member
Dr. Ward Collis Committee Member	Dr. Clinton Lee Committee Member
Dr. John Kelly Department Chair	Dr. Numan Dogan Committee Member

Dr. Sanjiv Sarin
Dean, The Graduate School

Biographical Sketch

Adam S. Bowen was born in Henrico, Virginia and was raised in Charles City County, Virginia. He holds Bachelors and Masters of Science degrees in Electrical Engineering from North Carolina Agricultural and Technical State University. He is currently a candidate for a Doctor of Philosophy degree in Electrical Engineering at North Carolina Agricultural and Technical State University.

Dedication

I would like to dedicate this thesis to my mother and father as they have been a constant source of inspiration and motivation throughout the entire process of both my professional and student career.

Acknowledgements

I would like to express my gratitude to those who have helped and influenced me in the process of completing this work. I would like to thank my advisor, Dr. Shanthi Iyer, for her continuous commitment towards the ongoing research. This work was supported by the U.S. Department of Education Title III.

Table of Contents

List of Figures

List of Tables

List of Symbols

α	Absorption coefficient
λ	Wavelength
2D	Two dimensional
3D	Three dimensional
AFM	Atomic Force Microscopy
at. %	Atomic percent
As	Arsenic
BAC	Band anti-crossing
BEP	Beam Equivalent Pressure
CB	Conduction band
cps	Counts per second
E_C	Conduction band energy
E_g	Band gap energy
E_V	Valence band energy
FTIR	Fourier Transform Infrared
FWHM	Full width half maxima
Ga	Gallium
GaSb	Gallium antimonide
GaInSb	Gallium indium antimonide
HgCdTe	Mercury cadmium telluride
HRXRD	High Resolution X-Ray Diffraction
In	Indium

InAs	Indium arsenide
InAsN	Indium arsenide nitride
IR	Infrared
LO	Longitudinal Optical
LWIR	Long wavelength infrared
MBE	Molecular Beam Epitaxy
MCT	Mercury cadmium telluride
MWIR	Mid wavelength infrared
N	Nitrogen
NRA	Nuclear Reaction Analysis
QW	Quantum Well
RHEED	Reflection High Energy Electron Diffraction
RBS	Rutherford Back Scattering
RF	Radio frequency
RLP	Reciprocal Lattice Point
RLU	Reciprocal Lattice Unit
RMS	Root mean square
RSM	Reciprocal Space Map
RT	Room temperature
Sb	Antimony
SL	Superlattice
SLs	Superlattices
SLS	Strained layer superlattice

T (%)	Transmission (%)
Te	Tellurium
TO	Transverse Optical
Ts	Substrate temperature
UHV	Ultra high vacuum
VLWIR	Very long wavelength infrared

Abstract

Infrared (IR) sensors are extremely important in missile defense as well as in satellite-based infrared detection systems. Long-range ballistic missile defense for incoming missile acquisition, tracking, and discrimination requires space-based infrared technology. Hence long wavelength and very long wavelength infrared regimes are extremely important for such applications. The focus of this work is on the investigation of superlattices (SLs) and in particular dilute nitride based SLs for such applications in this infrared region. A comprehensive study of InAs/GaSb, InAs/GaInSb, InAsN/GaSb and InAsN/GaInSb SLs grown by molecular beam epitaxy (MBE) has been carried out using different characterization techniques. Optimization of the structures with growth parameters such as interfacial layers, layer thickness, and material composition will also be discussed. The judicious selection of the above combination of parameters was abetted by theoretical simulation using OPTEL_ZB software. A systematic and detailed study has been made correlating the structural quality, vibrational modes, scanning transmission electron microscope (STEM) micrographs and optical properties of each of the optimized structure of the SL. All the SLs were defect free with sharp interfaces and well defined sublayers as attested by high resolution x-ray diffraction (HRXRD) and asymmetric reciprocal space mapping (RSM) spectra as well as STEM images. The unique feature of this work is the growth of InAsN/GaSb SL which has not been reported elsewhere to the best of our knowledge. This SL shows promise in that thinner layers of InAsN were used for the same strain balancing effect as thicker InAs. Hence the former would improve optical absorption. Since the N in InAsN reduces the overall lattice constant of the material system it added another degree of freedom in strain balancing the structure to the GaSb substrate. A cut off wavelength of ~20 μm was achieved with the InAsN/GaSb SL.

CHAPTER 1

Introduction

1.1 Motivation

Infrared (IR) detectors are extremely important in missile defense as well as in satellite-based infrared detection systems [1]. Being able to see in the dark is just as important, if not more important as being able to see in the daytime in wartime situations [1]. Space-based infrared technology is important to long-range ballistic missile defense for incoming missile acquisition, tracking, and discrimination [2]. Ballistic missile defense against various targets requires tactical and strategic sensors and sensor platforms [2]. Therefore, with IR technology users not only one can see the incoming targets, they can also track, discriminate, and determine the final aim point for firing [1]. In addition, because of the temperature range of objects in outer space scenarios, there is a strong need for a multicolor device (as shown in Figure 1) which encompasses the MWIR, LWIR and VLWIR regimes.

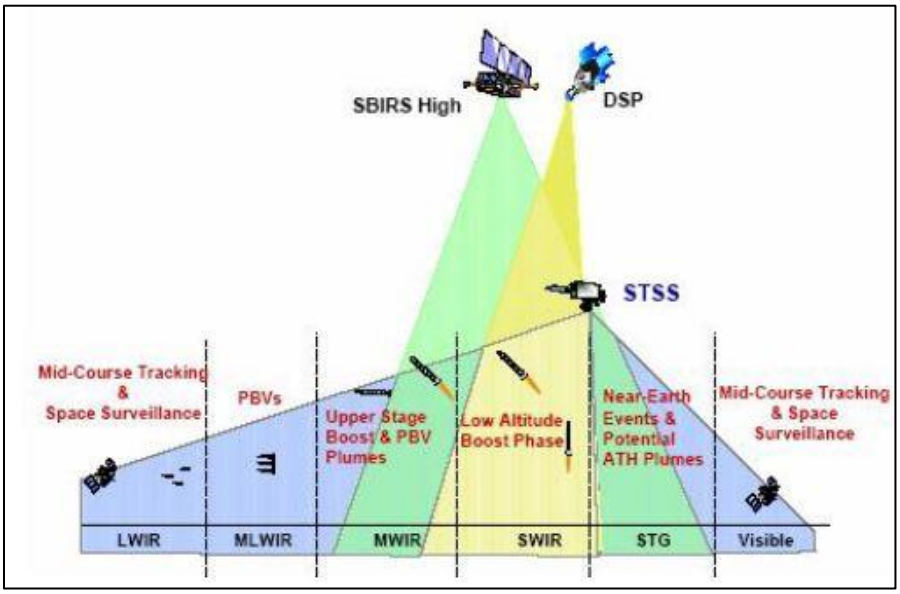

Figure 1 Space tracking and surveillance system [2]

Currently HgCdTe (MCT) is the material system of choice for infrared detectors for LWIR while Si and Ge are used in VLWIR[3]. However, there are some issues with MCT based detectors namely uniformity and degradation of the layers in the detector. III-V material systems provide a favorable alternative to MCT based detectors [4]. The use of III-V material systems namely InSb, GaAs, GaSb, and InAs for infrared detectors shows great promise, hence there is extensive ongoing research using these materials. In addition, related dilute nitride detectors [5-8] are also showing great promise in the LWIR and VLWIR regions.

1.2 Background

1.2.1 Infrared radiation. All objects above 0 K emit electromagnetic radiation (gamma, x-rays, UV, visible, IR, micro, and radio waves) with most of the objects on earth emitting IR light. IR radiation (shown in Figure 2) corresponds to a wavelength range of 750 nm to 1000 µm, and can be subdivided into NIR, SWIR, MWIR, LWIR, VLWIR, and FIR [9] (comparison shown in Figure 3 (a-d).

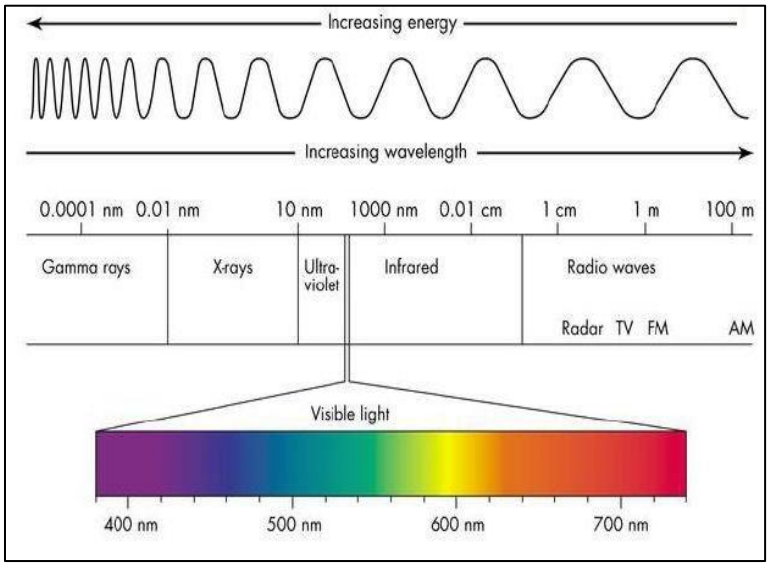

Figure 2 Electromagnetic spectrum [10]

The exploration of IR detectors is advantageous in that the information obtained on objects emitting IR radiation (< 2000 K) can be used to determine their geometry, temperature, surface quality, and chemical content [11]. The investigation of novel materials that can operate in the LWIR and VLWIR regimes, commonly defined as the wavelength region 8 to 12 μm and beyond 14μm [3] respectively, that can lead to future development of the efficient detectors [5, 7, 8, 12-19] are the main focus of this work because of their strategic space application. Hence these are ideally suited for identification of targets in the low temperature background [20].

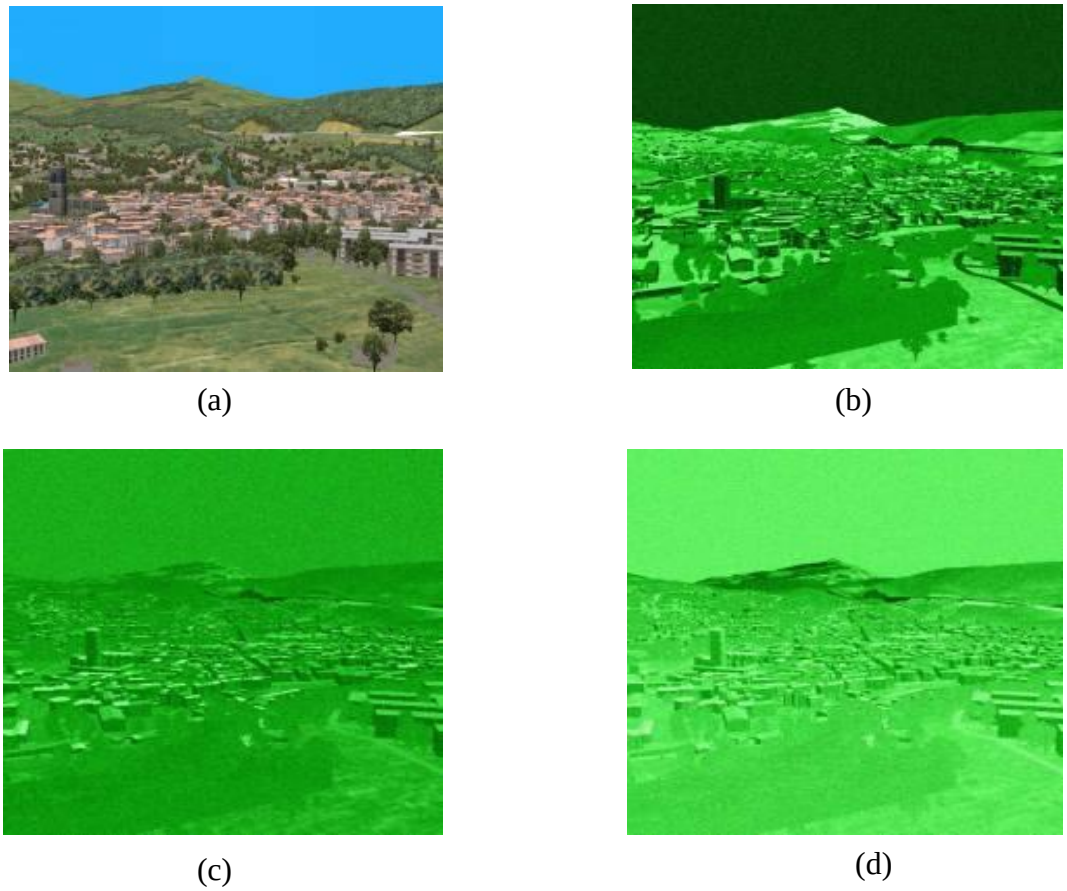

(a) (b)

(c) (d)

Figure 3 Identical image displayed in (a) visible regime (b) SWIR regime (c) MWIR regime (d) LWIR regime [21]

1.2.2 Blackbody radiation. The electromagnetic radiation, emitted by objects is proportional to its temperature. To quantify this, a theoretical perfect black body is used as a

reference, where it is an absorber of all radiant energy and a perfect emitter of electromagnetic radiation [11]. The spectral distribution of intensity is the dependence of the intensity of the blackbody radiation on the wavelength of light emitted (as shown in Figure 4) [11]. The spectral distribution of intensity is given by Planck's law shown in Equation 1

$$I(\lambda) = \frac{2\pi hc^2}{\lambda^5} \frac{1}{e^{\left(\frac{ch}{k_b T \lambda}\right)} - 1} \quad (1)$$

where *h* is Planck constant, *c* is the speed of light, λ is the wavelength, k_b is Boltzmann constant, and *T* is the temperature which measures the spectral radiation from a blackbody [11]. As shown in equation 1.1 the spectral distribution of intensity has an exponential dependence on temperature and wavelength. An example of this is an object whose temperature is around 300 K, which corresponds to a wavelength peak in the 8-14 μm range. Also the atmosphere absorbs weakly in the 8-14 μm [22] region, (as shown in Figure 5) which is ideal for space applications.

1.2.3 Detectors. A detector can be defined as a device that converts one type of signal into another [11] such as light to an electrical signal. IR detectors can be classified as either thermal or photon [23]. Thermal detectors work by the absorption of light which changes its temperature [23]. The change in temperature alters the electrical conductivity, which serves as a measurable output [23]. A photodetector operates by converting light signals that hit the junction to a quantifiable voltage or current. The junction uses an illumination window with an anti-reflecting coating to absorb the light photons. The result of the absorption of photons is the creation of electron-hole pairs in the depletion region. Examples of photo detectors are photodiodes and phototransistors. The type of detector that is of interest in this work is the photodiode.

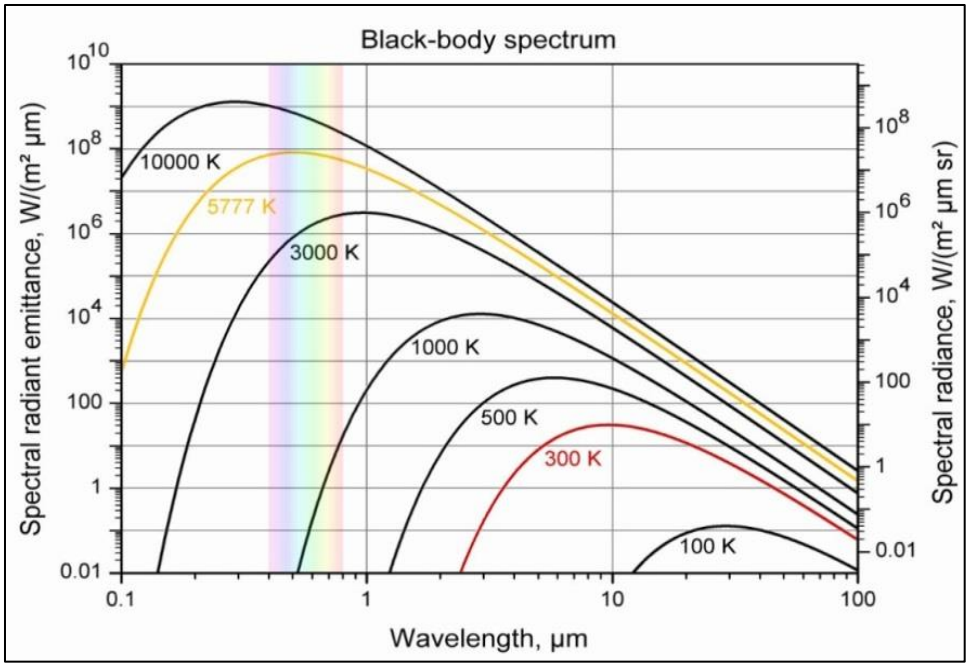

Figure 4 Spectral radiance as a function of wavelength [24]

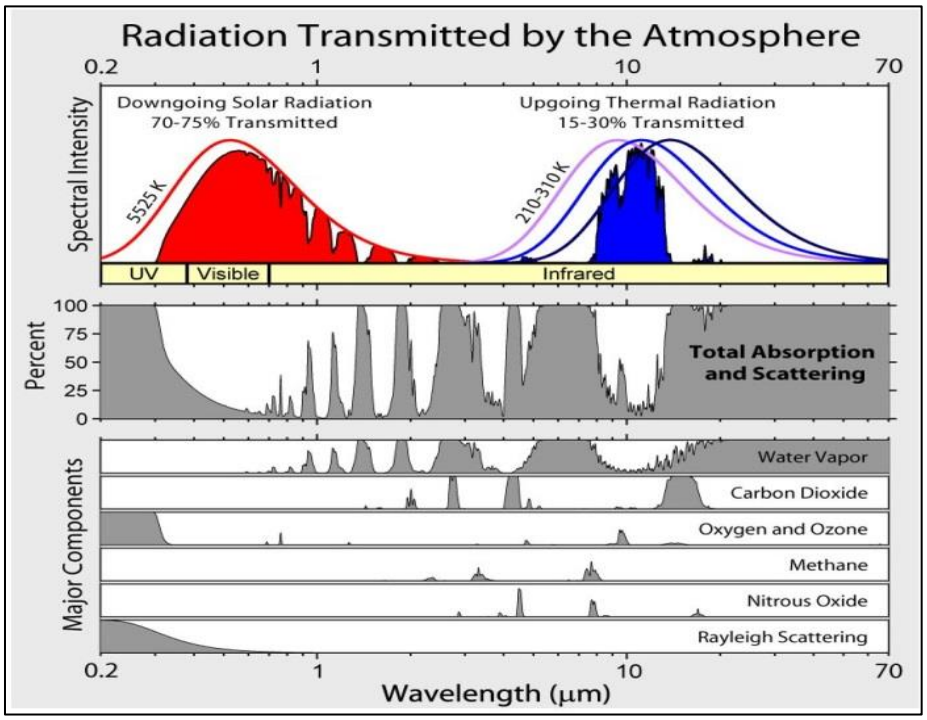

Figure 5 Atmospheric absorption from 1 to 70 µm [25]

1.3 Objectives

The focus of our work is to grow a novel III-V superlattice structure that would be suitable for fabrication into a photodetector capable of operating in the LWIR to VLWIR region. To achieve this first a literature review (Chapter 2) was done to give a background on work that has already been carried out. This was very important in determining where a new SL material system could be utilized. It was determined that in-plane strain was important in reducing the SL band gap and thus, shifting to a higher wavelength. It was also revealed that thinner SL layers obtained higher absorption. With this information dilute nitrides were of interest because of its inherent properties of lowering the band gap as well reducing the lattice parameter. The InAsN/GaInSb SLS shows promise in that thinner layers of InAsN might be used for the same strain balancing effect as thicker InAs which should improve optical absorption. Since the N in InAsN will reduce the overall lattice constant of the material system another degree of freedom is added in strain balancing the structure to the GaSb substrate. Further, incorporating N in the InAs layer as well as in the GaInSb layer should improve optical absorption because of the increase in effective mass. This will also allow for higher concentrations of In the GaInSb layer while managing to keep the structure stain balanced

1.4 Outline of the Dissertation

This dissertation consists of six chapters which are listed below in a chapter wise outline of this study.

Chapter 1 discusses the motivation behind this work, the background and the objectives. The motivation discusses the importance of infrared detectors and the need for a material system to replace HgCdTe (MCT). The background gives a brief introduction to infrared radiation, the

various wavelength regimes, blackbody radiation, and detectors. Lastly, the objectives of this work are discussed.

Chapters 2 gives a focused review of MCT detectors, III-V material systems, superlattices, and dilute nitrides. The benefits of MCT are mentioned as well as current limitations of this material as a LWIR and VLWIR detector. III-V materials are discussed, in particular InAs and GaSb. Chapter 2 also gives a background on the types of superlattices, lattice matching, and the influence of interfaces. Finally, dilute nitride SLs will be reviewed as well as InAsN bulk epilayers.

In Chapter 3 a description of the SL growth and optimization by MBE is given. This chapter includes theoretical modeling from Optel_ZB software which aided in the MBE growths. The MBE system configuration used for the growth is presented and the in-situ characterization techniques are described. The MBE growth procedure which includes ramping of the temperature, opening and closing of the shutter sequences and growth rate determination by reflection high energy electron diffraction (RHEED) for four different types of SLs are also presented.

Chapter 4 presents the material characterizations used in this work. Various techniques were used namely high resolution x-ray diffraction (HRXRD), reciprocal space mapping (RSM) and Raman spectroscopy for the SL structural quality, stress and strain, atomic force microscopy (AFM) for surface morphology, Rutherford backscattering spectrometry (RBS) and nuclear reaction analysis (NRA) for elemental composition of the constituent layers, scanning transmission electron microscope (STEM) imaging for visualization of the anion-cation dumbbells, accurate measurement of the layer as well as interfacial layer thickness and any intermixing and Fourier transform infrared (FTIR) spectroscopy for optical absorption.

Chapter 5 discusses results and analysis in this work. Results from each of the characterization technique is presented and analyzed. Finally, these were used to correlate and provide a greater insight into the different characteristics of the SLs and have provided the characteristics that SL need to exhibit to achieve SL of good structural and optical quality with smooth interface.

In conclusion, Chapter 6 discusses the key accomplishments made in this study. Finally, a suggestion of future work has been made including the next steps using the InAsN/Ga(In)Sb SLs.

CHAPTER 2

Literature Review

2.1 Introduction

This literature review gives an overview of historical background of superlattices and the various configurations of material systems. As mentioned in the introduction, the LWIR and VLWIR regions are of interest. Hence most of the background given is focused on material systems tuned to absorb in these regimes.

Currently HgCdTe or (MCT) is the materials system of choice achieving a cut-off wavelength in the range of 1 to 30 μm which provides excellent band gap tune-ability [26]. However, due to uniformity and degradation issues associated with this material system, the III-V system is being extensively investigated as an alternative to MCT [4]. The choice of the III-V material system due to several advantages that it offers over MCT will be presented. Advantages of incorporating nitrogen in the III-V material system and the heterostructures will be discussed.

2.2 MCT Detectors

The variable band gap $Hg_{(1-x)}Cd_{(x)}Te$ alloys was introduced in a 1959 publication by Lawson [27]. This started the development providing an unprecedented degree of freedom in MCT infrared detector designs [27]. MCT is an alloy of CdTe and HgTe, and is considered by many as the third semiconductor of technological of importance after Si and GaAs. MCT crystallizes in the zinc blende structure and is referred to as a pseudobinary alloy semiconductor [28].

MCT detectors exhibit an adjustable energy band gap over the 1-30 μm range [28] by altering the composition of Cd. The other advantages include large optical coefficients that enable high quantum efficiency and favorable inherent recombination mechanisms that lead to

high operating temperature [28]. The band gap tuneability of MCT covers the entire IR range which makes it an important material in detector applications [28]. There are many applications for this material system that range from SWIR (1 to 3 μm) to VLWIR (14 to 30 μm) [26].

Considerable research is still in progress to improve MCT detectors, which are plagued by its native defect and incorporation of impurities [28]. The relatively low effective mass of MCT detectors causes tunneling which leads to excessive dark currents [29]. The other issues with MCT are the compositional non-uniformity [30], mechanical strains and thickness non-uniformity [28, 30, 31]. The MCT band gap is extremely sensitive to any small changes in the alloy composition and hence the emission wavelength. Due to the low band gap short lifetime of the carriers due to large Auger recombination rates [29, 32] pose a challenge. Even though long wavelength (8-12 μm) detector technology is predominantly based on the MCT material system, difficulties still remain, particularly for wavelengths exceeding 10 μm where device performance is limited by large tunneling dark current and a sensitive dependence on precise composition control to accurately determine the energy gap.

2.3 III-V Material Systems

2.3.1 Introduction. Given the maturity of III-V growth and processing technology, these have been investigated as an alternative to MCT. Amongst the III-V materials InSb and InAs based bulk detectors emerged as the possible competitors due to the development of the crystal growth technique in the early 1950's [33]. Single crystals can be grown with relatively high purity and low dislocation density. The III-V material system exhibits zinc-blende structure and direct energy gap at the Brillouin zone center. The shape of the electron band and the mass of the light hole are commonly determined by the k.p. theory. The III-V materials have a typical negative

temperature coefficient of the energy band gap which is well explained by the Varshni relation [34] (as shown in equation 2)

$$Eg\ (T) = \ E_0 - \frac{\alpha T^2}{T+\beta} \quad (2)$$

where, α and β are fitting parameter characteristics of a given material.

2.3.2 The 6.1 Å semiconductor family. The three semiconductors, besides GaAs and AlAs, in the III-V materials system that are closely lattice matched are InAs (a= 6.0584 Å), GaSb (a= 6.0959 Å), and AlSb (a= 6.1355 Å) which are close to the 6.1 Å lattice parameter, with (room temperature) energy gaps ranging from 0.36 eV (InAs) to 1.61 eV (AlSb) [35]. The availability of high quality GaSb substrates and progress in the growth of antimonide based semiconductors has led to significant strides in the optical and electrical heterostructures and their applications. [36]. The heterostructures combining InAs with GaSb and InSb and their alloys are of principle interest [35]. This combination offers band lineups that are drastically different from those of the more widely studied (Al, Ga)As system, and the lineups are one of the principal reasons for interest in the 6.1 Å family [35].

An interesting alignment is that of InAs/GaSb heterojunctions, which was discovered in 1977 by Sakaki et al. [37]. This novel structure exhibited a broken gap lineup at the interface, where the bottom of conduction band of InAs lines up below the top of the valence band of GaSb, with a gap of about 150 meV [35] (as shown in Figure 6). There has been significant work reported in the literature on InAs and the antimonide heterostructures [29, 36, 38-48] which included AlSb [36], GaSb and their alloys (Al, Ga)Sb, (Ga, In)Sb, or Al(Sb, As) [35].

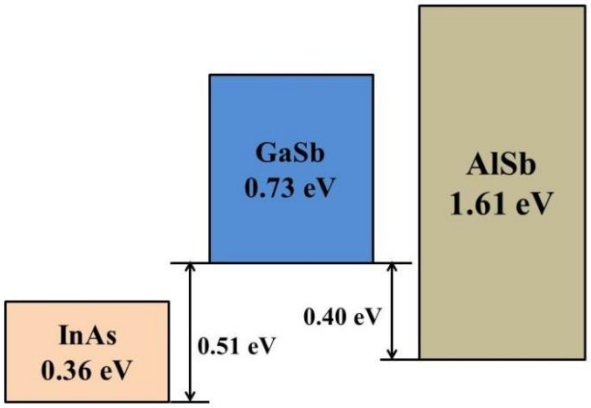

Figure 6 InAs, GaSb, and AlSb energy band lineups. Colored rectangles represent the forbidden band gap.

2.4 Superlattice

2.4.1 Superlattice band alignment and structure. The concept behind QW's, MQW's and SLS's is similar in that they all exhibit quantum confinement and create discrete subband levels. They differ in well interaction, which is controlled by the barrier thickness (as shown in Figure 7). A one dimensional periodic potential (superlattice) was introduced as man-made quantum structures to engineer the quantum states for electrical and optical applications [49]. Some typical superlattice characteristics are:

- Allows band structure engineering (suppress Auger related dark current / higher operating temperature)
- Large electron effective mass (smaller leakage current / higher detectivity)
- Interband transitions (normal incidence absorption / high quantum efficiency)
- Adjustable band gap (tunable cutoff 3 to 30 μm / multicolor capability)

In addition III-V semiconductor based SLs has the advantage of being highly uniform, cheap and robust.

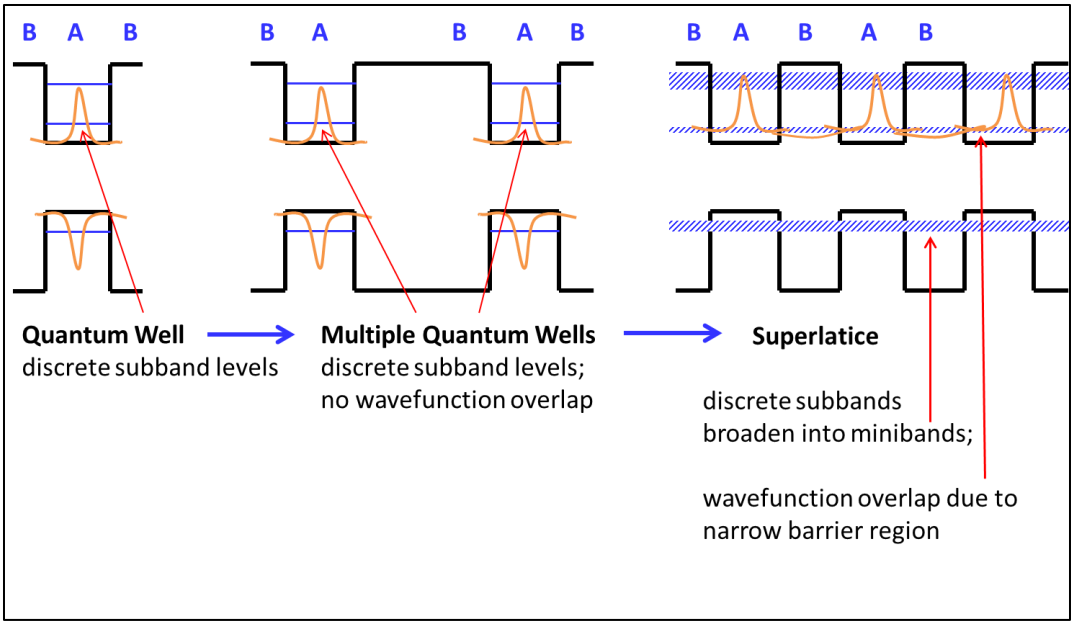

Figure 7 Comparison of quantum wells, multiple quantum wells and superlattices

2.4.1.1 Type I. In type I heterojunctions, one material has lower energy for both the electrons and the holes. Therefore, in this configuration both the electrons and holes are confined in the same layer. For example layer 'A' in Figure 8 is the potential well for both holes and electrons. The material system GaAs/AlGaAs [50] is a well-known example (as shown in Figure 8).

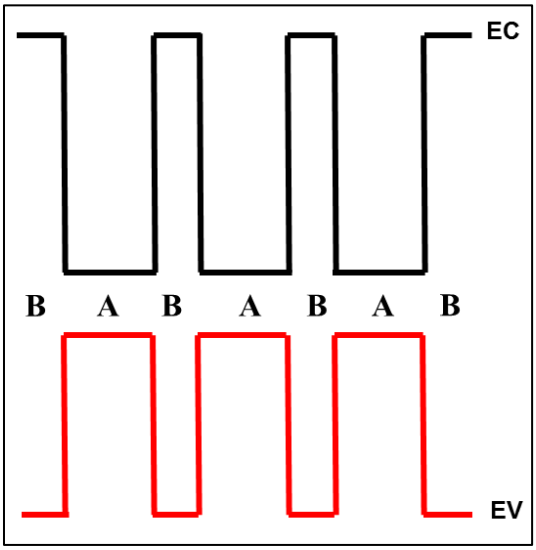

Figure 8 Type-I SL band-structure

2.4.1.2 Type II. In the superlattice of the broken gap alignment configuration, the wave functions of the lowest conduction subband and the highest valence subband are localized in the two different host semiconductors (spatially separated). Therefore, the positions of the CB edge and the VB edge can be tuned independently. It was proposed that this type of superlattice could be realized by using the closely lattice-matched semiconductor material systems InAs/GaSb [38, 51]. It was also pointed out in particular that based on the known electron affinity values, the CB edge of InAs was expected to be 0.14 eV lower than the VB edge of GaSb [51]. This (broken-gap band alignment) lead to an interesting behavior since the superlattice CB and VB states are close in energy and could consequently, interact [51]. This novel type of superlattice, in which the band gaps of the two semiconductors are in either a staggered or a broken-gap alignment, which was later referred to as "type II" (as shown in Figure 9 a and b) [38] to distinguish it from the "type I" (as shown in Figure 8) superlattice originally proposed by Esaki et al. [49] In type I SL the host band gaps are in a nested alignment and the wavefunctions of the lowest conduction subband and the highest subband are located in the same material system as opposed to the carrier confinements in the two different material systems in type II heterostructures resulting in a band gap lower than both of the individual materials systems.

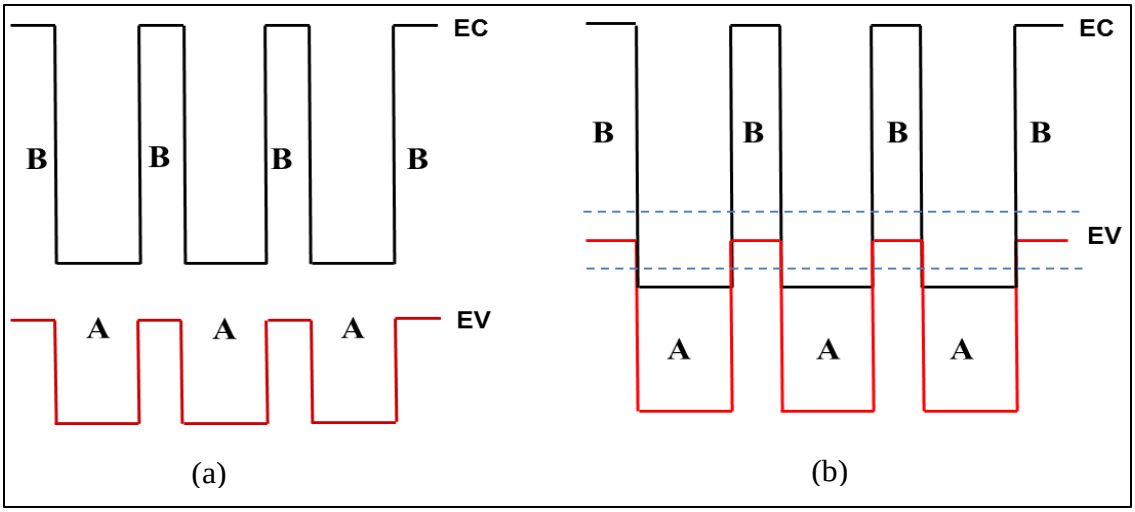

Figure 9 Type II SL band-structure: (a) staggered alignment and (b) broken alignment

2.4.1.3 Type III. HgTe/HgCdTe [52] belongs to the third category is referred to as a type III SL. This SL is composed of a semiconductor and a zero-band gap semiconductor. The HgTe/CdTe SL system was the first design from a new class of quantum-size structures for IR photoelectronics. This system was proposed as a promising new alternate structure for the LWIR detectors, which would replace detectors of HdCdTe alloys (as shown in Figure 10).

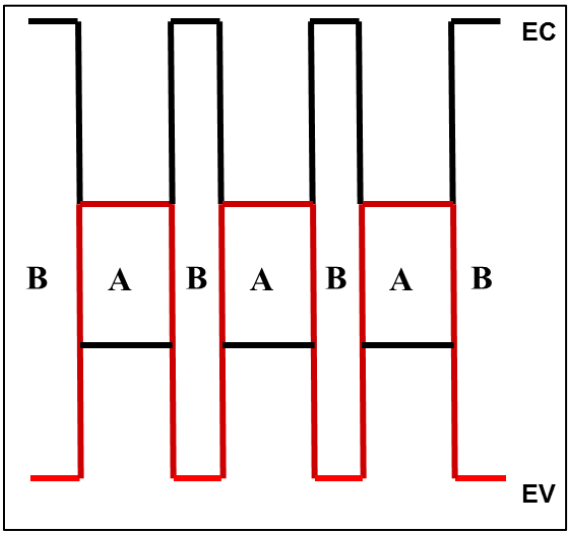

Figure 10 Type III SL band-structure

2.4.2 Lattice matching. When the thickness of the epi-layer exceeds a critical value, strain is relieved through threading dislocations (as shown in Figure 11). Performance of infrared photodetectors is strongly affected by threading dislocations which are scattering centers for minority carriers which in turn degrades the signal-to-noise ratio of the detector [29]. Hence, lattice matching the constituent layers to the substrate is very important and suitable materials are chosen from the phase diagram (as shown in Figure 12).

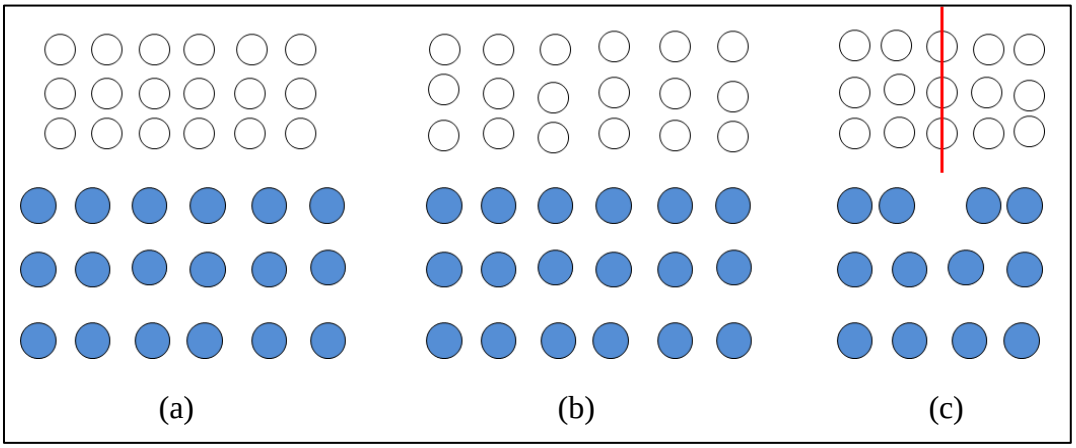

Figure 11 (a) Mismatched layers, (b) lattice mismatch accommodated by tensile strained epilayer and (c) epilayer is relaxed due to misfit dislocations

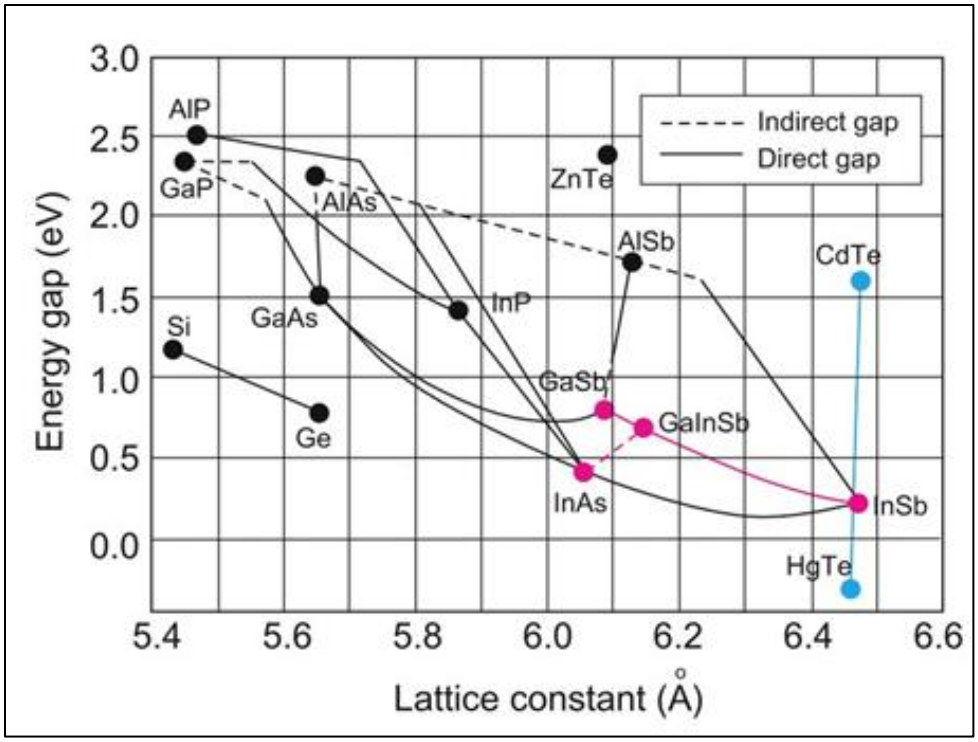

Figure 12 Energy gap vs. lattice constant [53]

2.4.3 Significance of strain balancing. For a strained layer superlattice (SLS) one of the materials will be in biaxial tension and the other will be in biaxial compression, which will yield the energy level split of light holes and heavy holes. For the material in biaxial compression, its band gap will increase, the heavy hole will move up and the light hole will move down. For the material in biaxial tension, its band gap will decrease, the light hole will move up and the heavy hole will move down (as shown in Figure 13). The more significant features of SL design is not just tailoring the energy band gap but engineering the SL energy band structure [44]. SL energy bands can be structured such that there is a larger energy separation between the heavy and light hole bands than the SL band gap energy, this suppresses Auger recombination mechanisms and thereby enhances carrier lifetime [44].

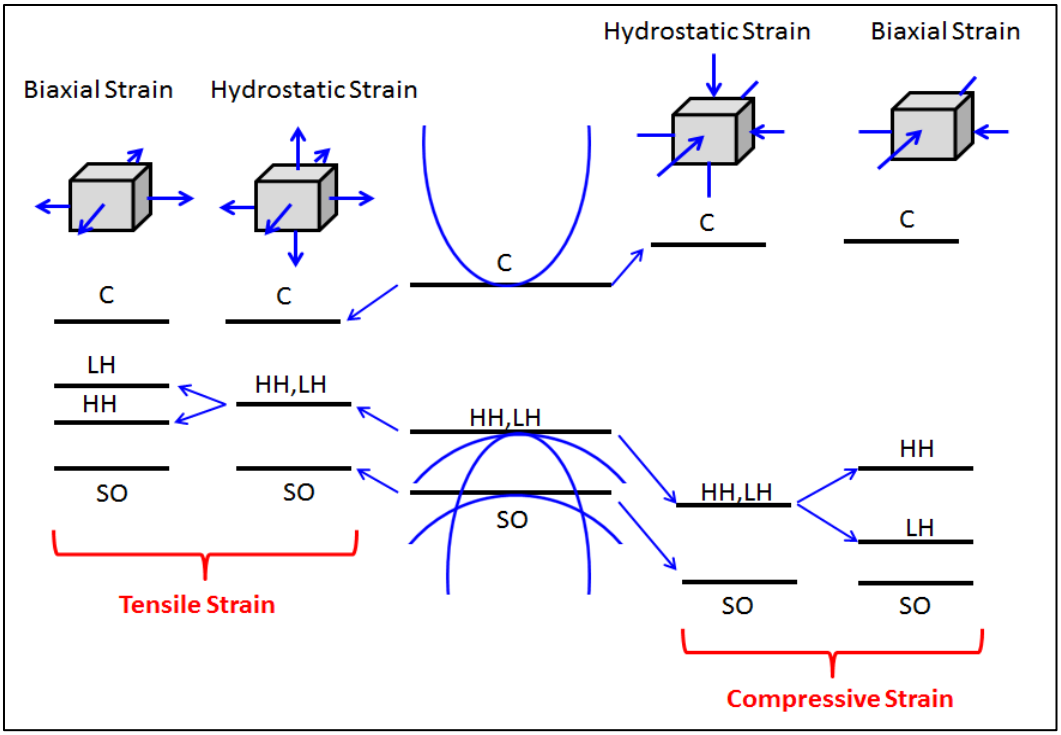

Figure 13 Effects of tensile and compressive strain on band gap (reproduced from ref. [54])

2.4.4 InAs/GaSb SLS. The energy level of electrons and holes in the QW determines the electronic band structures of the SL [36]. The formation of the electronic band structures is also affected by carriers in the adjacent wells [36]. The position of the conduction band is determined by the thickness of the well and barrier as well as the interface type and material composition. It was reported by M. Razeghi et al. [36] that as an empirical rule, the carrier energy level is almost inversely proportional to its effective mass. In addition, for a type II SL, the band gap is determined by the position of the conduction band, since the valance band almost remains constant.

InAs/GaSb is a misaligned type II SL, electrons and holes are located in adjacent layers, and therefore behave like a semimetal. Another characteristic in which it acts like a semimetal is that the hole confinement is at a higher level than the electron confinement. Because of the large effective mass of the GaSb, changes in the width of the barrier have no effect on the energy level

of the hole as discussed above. The large effective mass also prevents any tunneling of the hole through the InAs layer (well).

2.4.4.1 Effects of InAs well in a type II SL. The InAs layer is a QW in which the electrons are confined in one period of the SL. With thicker layers of InAs the conduction band shifts to a lower level. As the InAs layer becomes thicker the energy level of the conduction band shifts to a lower energy level than the valance band of the GaSb layer (barrier). Because of this, electrons can directly tunnel from one well to another via the valence band of the GaSb barrier, thus rendering a semi-metallic character to the SL.

2.4.4.2 Effects of GaSb barrier in a type II SL. The GaSb layer is a QW in which the holes are confined in one period of the SL. In addition, the GaSb layer functions as the barrier isolating electrons in the adjacent InAs wells. It is to be noted that since the effective mass of holes in the valence band is much heavier than that of electrons, the hole energy level relative to the bottom of the well is small [36]and also dependence of the energy on the barrier width becomes much weaker. However, the thickness of the GaSb barrier strongly affects the energy gap of the SL through the conduction band. Similar to the formation of bulk band structures, the conduction band of the SL is the broadening of individual energy levels of electrons in InAs wells due to the interaction between wells [36]. This interaction is determined by how far the InAs wells are separated from each other, and by the height of the barrier, which is impeding the electrons [36]. When the GaSb barrier layer is too thick, the SL is actually a system of non-interacting MQW's [36]. Therefore, the electron energy level is only determined by the layer thickness of the InAs wells in which electrons are confined[36]. With thinner layers of the GaSb barrier the electron wavefunctions start overlapping, causing an interaction between the electrons which causes the energy level to spilt into mini-bands [36]. The broadening of the mini-bands

shifts the lowest conduction level downward, closer to the conduction band edge [36]. Hence the thinner the GaSb barrier, the more the mini-bands broaden, which in turn reduces the energy band gap [36].

2.4.5 InAs/GaInSb SLS. InAs/GaInSb is a staggered type II SL, which means the offset, is so large that the electrons and holes are separated into different layers. However, there is an indirect weak spatial transition between the electrons and holes in adjacent layers. Because of this indirect nature of the inter-subband transition, thinner layers are used to increase the electron hole wave function overlap and thereby increasing the oscillator strength of the optical transition [44].

The effective band gap of the InAs/GaInSb SLSs can be tailored from 3 to 30 μm by varying thickness of constituent layers thus allowing fabrication of devices with operating wavelengths spanning the entire IR region [29].The InAs/GaInSb SLS is less sensitive to the compositional non-uniformities in the ternary layer than the MCT alloys with the same band gap [29]. For example, it has been reported [55] that a compositional ratio fluctuation of $\Delta x = 0.004$ would shift cutoff wavelength of MCT detector from 19 to 17 μm, whereas the corresponding ratio change for SLS is $\Delta x = 0.03$. The thin constituent layers in the SLS provide good electron-hole overlap, as well as optical matrix elements comparable to those of bulk MCT [29]. The GaInSb layers of the SLS are subjected to biaxial compression causing splitting of light hole and heavy hole mini-bands in the SLS band structure [29]. Therefore, Auger recombination rates are strongly suppressed relative to bulk MCT [56] leading to improved temperature limits of spectral detectivities as compared to MCT detectors [57]. In addition, the larger effective mass in SLS leads to a reduction in tunneling currents [29].

Amongst the two SLS systems binary (InAs/GaSb) and ternary (InAs/$Ga_{1-x}In_xSb$) SLS discussed above, theoretical predictions [29] seem to favor the InAs/$Ga_{1-x}In_xSb$ system due to the additional strain provided by the GaInSb layer, to extend detector cutoff wavelength into LWIR and VLWIR regions. Despite favorable predictions on the ternary system, most of the experimental results in the past 5 years have been on the binary InAs/GaSb system [29] due to its simplicity.

In lattice mismatched systems, when the thickness of epilayer exceeds the critical value, strain caused by lattice mismatch of epilayer to the substrate is relieved by formation of threading dislocations [58]. These threading dislocations play the role of scattering centers for minority carriers thus degrading the signal-to-noise ratio of the detector [29] affecting the performance of the IR detector. Long-wavelength detection can be achieved with thicker InAs and $Ga_{1-x}In_xSb$ layers with smaller In content [29]. However, detectivity of such devices is expected to be lower because of reduced spatial matrix element [29]. With an increase in the x value in In, the thickness of both integral layers required to achieve the same cutoff wavelength decreases [29]. This is attributed to the upward shift of $Ga_{1-x}In_xSb$ heavy-hole band due to larger compressive strain in $Ga_{1-x}In_xSb$ layers with subsequent reduction in SLS band gap allowing thinner layers for realization of the same cutoff wavelength [29], thus alleviating the problem associated with the dislocations induced by lattice mismatch. Thus lattice bilateral tension in InAs and compression in GaInSb layers leading to reduced SL band gaps can be achieved by narrowing the layers which also improves absorption [59].

2.4.5.1 Slow progress of InAs/GaInSb SLS. Only a few reports on InAs/ $Ga_{1-x}In_x$ Sb SLS for optoelectronic applications such as photodetectors [60-65] have been published. A reason for this is the sensitivity of the narrow energy gap to the variation of thicknesses of the

constituent layers [29, 66] though it is less sensitive to the compositional variation as discussed above in section 2.2. Using the three-band envelope-function model it was shown [67] that monolayer fluctuations in layer thickness of InAs and $Ga_{1-x}In_xSb$ would not shift the cutoff wavelength significantly. However, E. Plis et al. [29] using the modified bond orbital mode (EBOM) predicted sub-monolayer thickness fluctuations changing the cutoff wavelength by 50%.

The other problem with this system is the ternary composition of higher In (x). Though it was shown [66] that the electron-hole wavefunctions overlap and its associated oscillator strength also increase with the increasing x the growth of these layers is still challenging as this composition lies in the miscibility gap and also the limitations imposed due to critical thickness by the strained material[29]. Thus the InAs/GaInSb material system is still in a very early stage of development [26] with problems still existing with material growth, processing, substrate preparation, and device passivation [68].

2.5 GaAs / InSb / GaInSb / GaInAs – like interfaces (IF)

Besides controlling the composition, thickness and quality of the individual layers, control of the composition and roughness of the interfaces between the layers is also important [69]. The shutter sequence is critical since both groups III and V constituents change at the transition from InAs to GaInSb and then back to InAs [69]. At these transitions or interfaces Ga-As like or In-Sb like interfaces [69] can occur which can be intentional (forced) or unintentional (random). Since the transition is from InAs to GaInSb and vice versa ternary and quaternary alloys can also be formed. The InSb-like interface has been found to be preferable over a GaAs-like interface for infrared detector applications [70].

Early calculations comparing these two interface types found that a smaller band gap and higher optical absorption occurred with InSb-like interfaces due to the compressive strain generated in the SL [71]. Later experiments confirmed that the interface composition affected the band alignment between the InAs and GaSb layers [72]. The results confirmed that the band offset was 30 meV larger for the InSb-like interfaces [69]. The interface roughness depends on a number of factors, namely the interface type and growth procedure which can also cause disorder [69]. The InSb-like interfaces are smoother than GaAs-like, on both SL layers, and they are more abrupt [73, 74]. InSb interface between both layers also serves the most important function to strain balance the structure to keep it closely lattice matched to GaSb.

Since random interfaces diffuse, the most commonly used interface is InSb-like at both interfaces [69]. With that being said, the most important function among others of the forced interface is to help strain balance the structure to keep it lattice matched to the host (GaSb) substrate [69]. It has been reported in the literature that to keep the thick superlattice stacks from relaxing and forming dislocations, the residual lattice mismatch must be below $\pm 5 \times 10^{-3}$ relative to the substrate [69, 75]. For this reason, there are some SL structures employing a combination of GaAs-like and InSb-like interfaces [75, 76]. More recently the use of ternary interfaces of $Ga_{1-x}In_xSb$ (As or Sb) depending on which layer of the SL the interface is grown on have been used [77, 78].

Forced interfaces between 0.5 to 1.35 monolayers (ML) thick have been reported [29, 79]. By controlling the interface thickness and composition(s), a lattice mismatch of less than 0.0043% has been achieved, as reported by G. Brown et al. [77]. InSb-like interface is smoother than GaAs-like interface and a smaller band gap and higher optical absorption occurs due to the

compressive strain generated in the SL so grow 1 ML of InSb between InAs to GaSb transition [69, 80].

2.6 Dilute Nitride

2.6.1 InAs/GaInSbN strained-layer superlattice. A design approach adopted by Aina et al. [7] was to use GaInSbN layers in SLS structures to mitigate the effects of the lattice mismatch. It was shown that by properly selecting the optimum GaInSbN composition to strain balance the InAs in the SLS, it is possible to achieve LWIR and VLWIR cut-off wavelengths without degrading detector material properties [7]. Therefore, for the InAs/$Ga_{1-x}In_xSb_{1-y}N_y$ SLS higher concentrations of *x* can be incorporated since N reduces the lattice constant.

Current state-of-the-art VLWIR lasers and detectors made of MCT but antimonide-based semiconductor materials have lower detectivity and quantum efficiencies [28]. The disadvantages with the MCT IR detectors include large tunneling current (because of low band gap), compositional imprecision causing variation in band gaps, and high Auger recombination leading to dark current [69]. Theoretical studies suggest that dilute nitrides SLS have shown good spatial uniformity with improved overall optical, transport and confinement properties that can operate at higher temperatures [7]. Other than Aina et al [7] there has been no study on dilute nitride SLS carried out ,which is capable of higher performance and can potentially operate at higher temperatures [7].

The band-gap reduction in the dilute nitride occurs due to the localized interaction between the host conduction band and the resonant level, which arises from the substitution of highly electronegative nitrogen for a few percent of the host anions [81, 82] can be described by the band anti-crossing (BAC) model [81, 82]. The electronegativity mismatch between nitrogen and antimony is greater than for any other combination of commonly used group V elements [83].

Subsequently, the band-gap reduction in dilute antimonide nitrides is expected to be more extreme than for dilute arsenide nitrides, such that the addition of a small percentage of nitrogen to GaSb or InSb is predicted to move their response wavelengths into the long or even very long wavelength IR ranges [5, 8].

2.6.2 InAsN bulk. InAs /GaSb SLS have been extensively studied in the wavelength region 8-14 μm since the proposal of Smith and Mailhiot [84]. Tunneling currents in the SLS has been reduced due to large effective mass [52]. Auger recombination has been reduced, carrier lifetime has been enhanced, and signal-to-noise ratio at high temperature operation has been improved over the past decade [4, 26, 85]. Since N increases the effective mass, the Auger recombination should be further reduced in an InAs(N)/GaInSb SLS. The InAsN/GaInSb SLS shows promise in that thinner layers of InAsN might be used for the same strain balancing effect as thicker InAs which should improve optical absorption. Since the N in InAsN will reduce the overall lattice constant of the material system another degree of freedom is added in strain balancing the structure to the GaSb substrate. Further, incorporating N in the InAs layer as well as in the GaInSb layer should improve optical absorption because of the increase in effective mass. This will also allow for higher concentrations of In the GaInSb layer while managing to keep the structure stain balanced. The most currently used material system for IR detection MCT is compared to the upcoming III-V's and novel dilute nitrides in Table 1.

Table 1

Comparison of MCT, III-V and Dilute Nitride

	MCT	III-V	Dilute Nitride
Large electron effective mass (smaller leakage current / higher detectivity)		X	X
suppress Auger dark current / higher operating temperature)	X	X	X
Interband transitions (normal incidence absorption /high quantum efficiency)		X	X
Tunable cutoff	X	X	X
Multicolor capability	difficult	X	X
Highly uniform /cheap and robust		X	X
Currently most used	X		
Adds degree of freedom in lattice matching			X
Increases effective mass			X

CHAPTER 3

SL Growth and Optimization by MBE

3.1 Introduction

In this chapter a brief description of the SL growth and optimization by MBE is given. This chapter includes theoretical modeling from Optel_ZB software which aided in the MBE growths. The MBE system configuration is described and the in-situ characterization techniques are mentioned. In this chapter the MBE growth procedure is discussed as well as RHEED, which allowed in-situ monitoring of the growth and determination of the growth rate.

3.2 Growth Parameters from Theoretical Modeling

OPTEL_ZB simulation software was used as a guide for quick growth turn around by providing the SLS band gap based on layer thickness, material system and composition. As an example, for an InAs/$Ga_{.84}In_{.16}Sb$ SLS with a well thickness of 49 Å and a barrier thickness of 23 Å the simulated band gap was 513 meV while the experimental band gap on our test structure not reported in this work was 510 meV close to the predicated band gap.

Hence, OPTEL_ZB simulation software designed by Quantum Semiconductor Algorithms was used as a guide for quick growth turn around by providing the SLS band gap based on layer thickness, material system and composition. The two material systems simulated in this work were InAs/GaInSb and InAsN/GaInSb. The process began by verifying the results of the software using GaAs/AlAs quantum wells. This material system was chosen because its behavior is well understood, which aided with the learning curve using the software as well as tailoring the parameters in the software to the material systems of interest. The outputs of the GaAs/AlAs QW's were confirmed by comparing our data to those found in the literature. Various parameters of this material system were tested to determine the effects it had on the band

gap of the material system. These tests included (1) changing the length of the wells (InAs and InAsN), (2) changing the composition of In within the barrier (GaInSb) of the superlattice and another factor that was a main focus was (3) turning the strain "*off*" and "*on*" in the material as discussed in the following sections.

3.2.1 Effect of change in well length. The first test conducted was used to determine the effects of a change in well length (measured in angstroms). The simulated band gap of the InAs/$Ga_{.80}In_{.20}Sb$ material system was around 231 meV when the well and barrier were of the same length of 20 Å, as seen in Figure 14. Another simulation was performed where the well (InAs) length was increased to 30 Å while the barrier ($Ga_{.80}In_{.20}Sb$) length remained fixed at 20 Å.

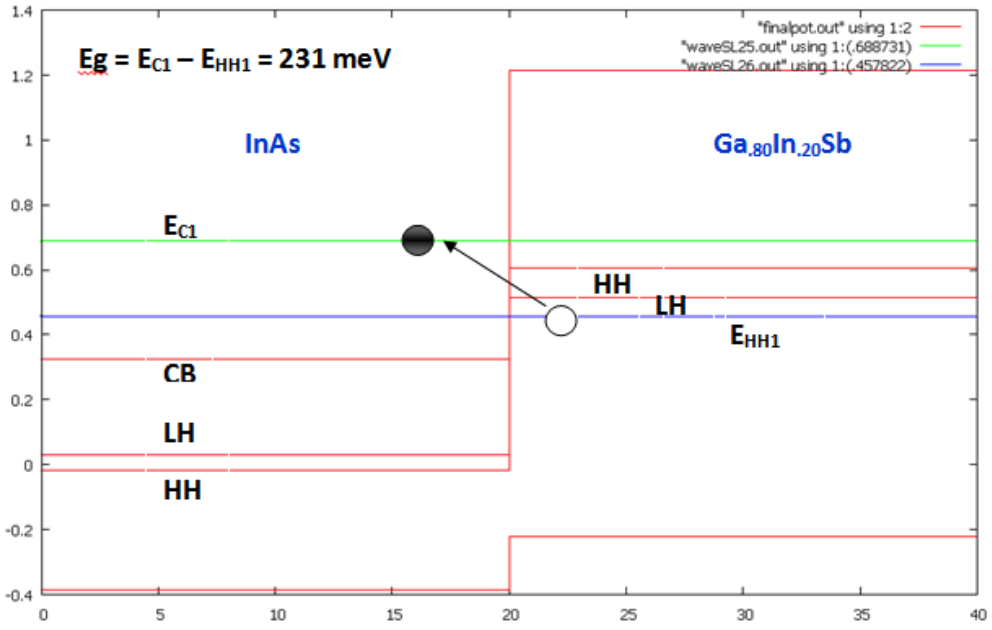

Figure 14 Simulated SLS band alignment of InAs/$Ga_{.80}In_{.20}Sb$, the length of the well and barrier are both 20 Å

The output results of this simulation showed a decrease in the SLS band gap by almost 100 meV to around 139 meV, as shown in Figure 15.

3.2.2 Effect in change of In content. This test was conducted to observe the effect of In composition on the SLS band gap. The In composition in the barrier material ($Ga_{(1-x)}In_{(x)}Sb$) was tested at 15% and 25% which was a 10% change in In content within the material system. The SLS band gap for 15% In ($Ga_{.85}In_{.15}Sb$) with the barrier and well length set at 20 Å is around 247 meV, as shown in Figure 16. With an increase in In content to 25% there is a decrease in the band gap to 215 meV, which is a relatively small change of 32 meV, as shown in Figure 17.

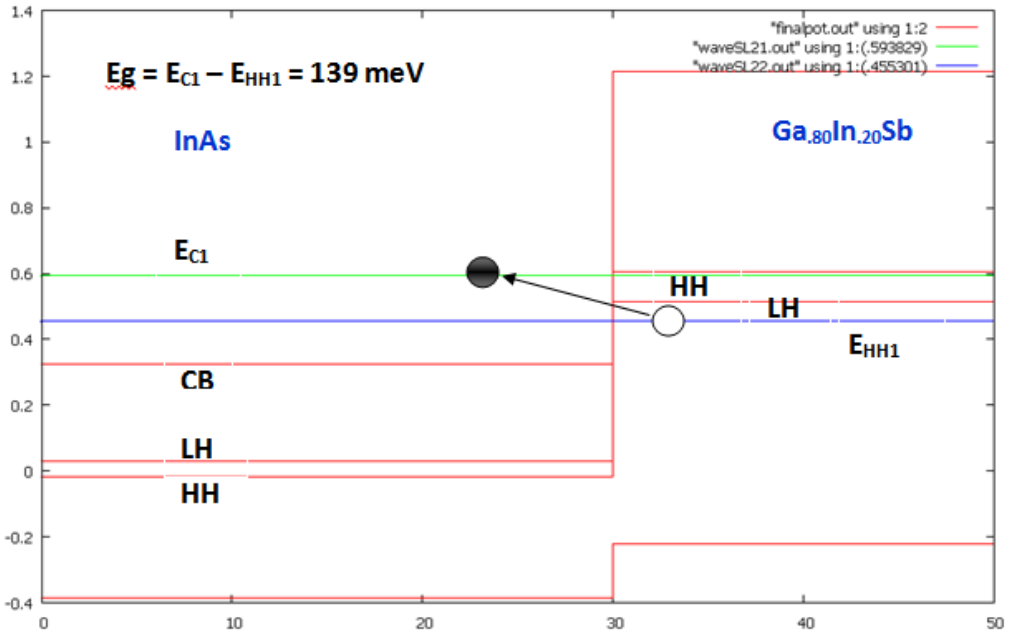

Figure 15 Simulated SLS band alignment of InAs/$Ga_{.80}In_{.20}Sb$, the length of the well is 30 Å and the length of the barrier is 20 Å

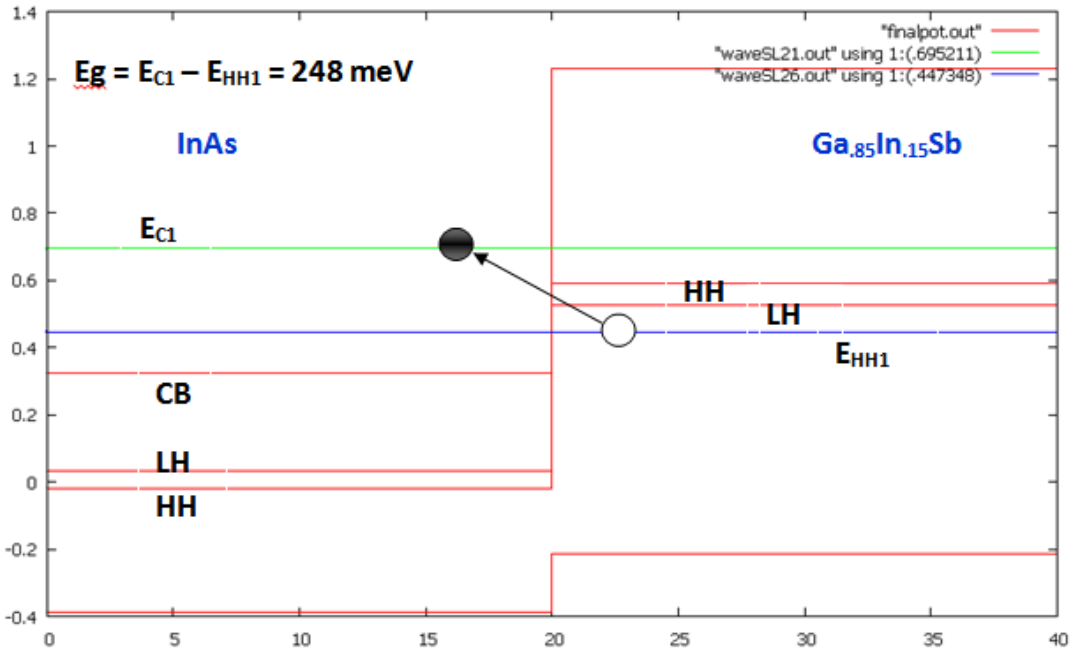

Figure 16 Simulated SLS band alignment of InAs/$Ga_{.85}In_{.15}Sb$, the length of the well is 20 Å and the length of the barrier is 20 Å

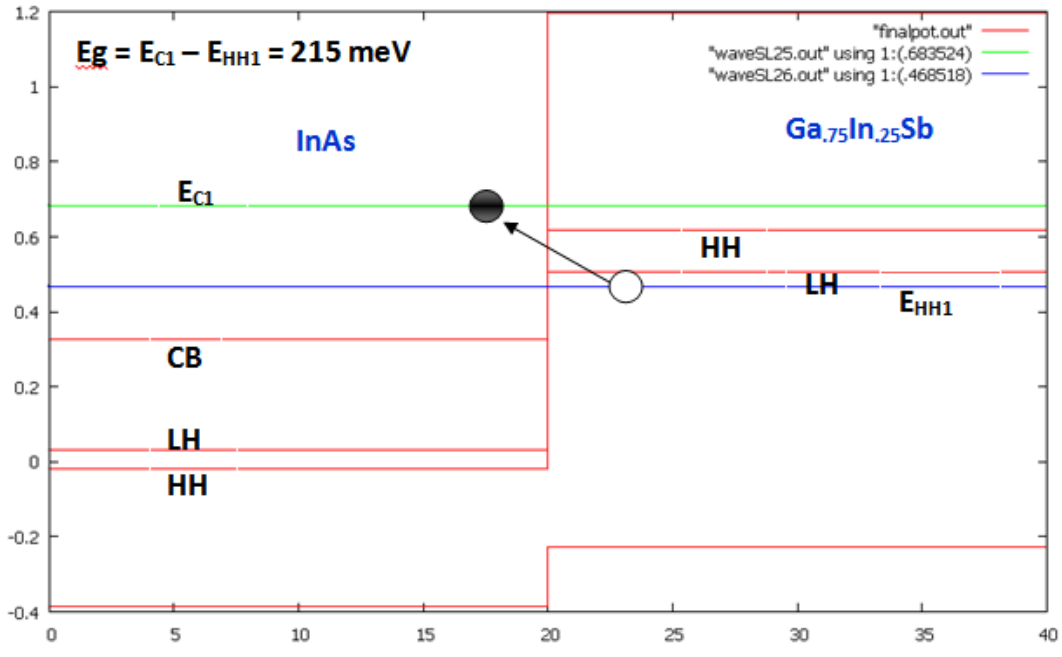

Figure 17 Simulated SLS band alignment of InAs/$Ga_{.75}In_{.25}Sb$, the length of the well is 20 Å and the length of the barrier is 20 Å

3.2.3 Effect in changing the strain parameter "on" and "off". One of the final tests conducted using the InAs/GaInSb material system was varying the strain parameter of the system. The strain could be turned *on* and *off* in the software which in turn changes the splitting of heavy hole (HH) and light hole (LH) bands within the system. There is an increase in band gap when the strain parameter was turned *off* which was 149 meV. When strain was *off*, one could easily observe the conduction band (CB) and the valence band (VB) on the graphs as there is no splitting of the HH and LH as shown in Figure 18. Figure 19 shows the effect of the split in HH and LH for resulting in the reduction of the SLS band gap to about 110 meV.

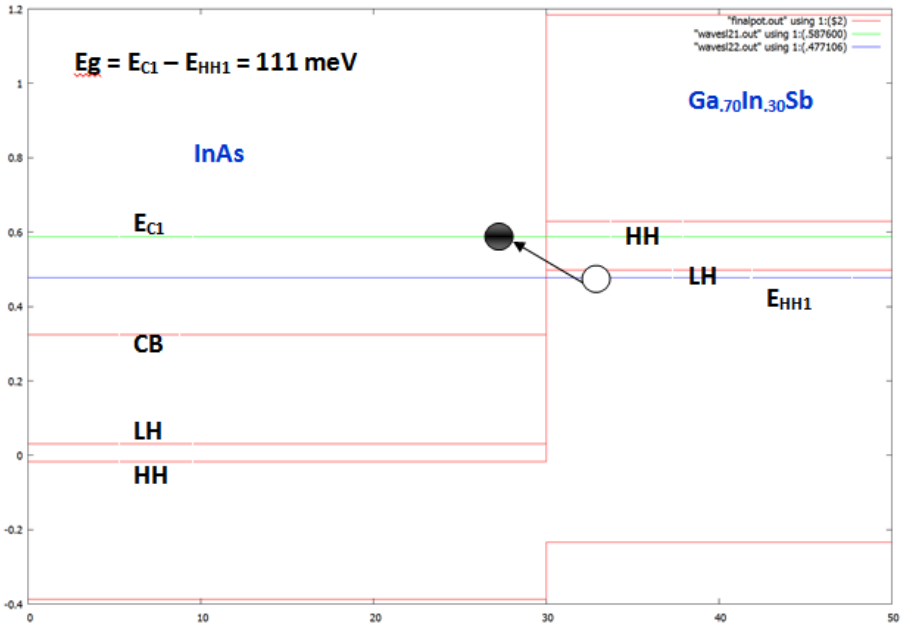

Figure 18 Simulated SLS band alignment of InAs/$Ga_{.70}In_{.30}Sb$, with strain parameter "off" the well length is 30 Å and the barrier length is 20 Å

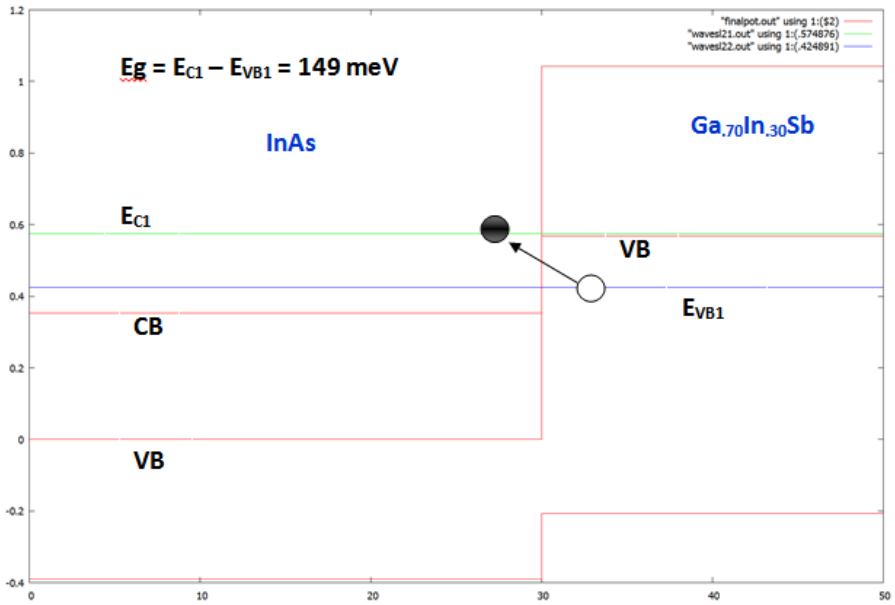

Figure 19 Simulated SLS band alignment of InAs/$Ga_{.70}In_{.30}Sb$, with strain parameter "on" the well length is 30 Å and the barrier length is 20 Å

3.2.4 Simulation with InAsN. The most recent simulation that has been conducted was on InAsN with 1 % N composition at 4K to reduce the overlapping of the bands occurring at higher temperatures (300K). The band gap values of the material similar variation with well thickness as discussed above. For instance, for 20 Å well/barrier thickness the band gap of $InAs_{.99}N_{.01}/Ga_{.75}In_{.25}Sb$ SLS is around 218 meV as shown in Figure 20, which reduces to 121 meV for 30 Å thickness (Figure 21).

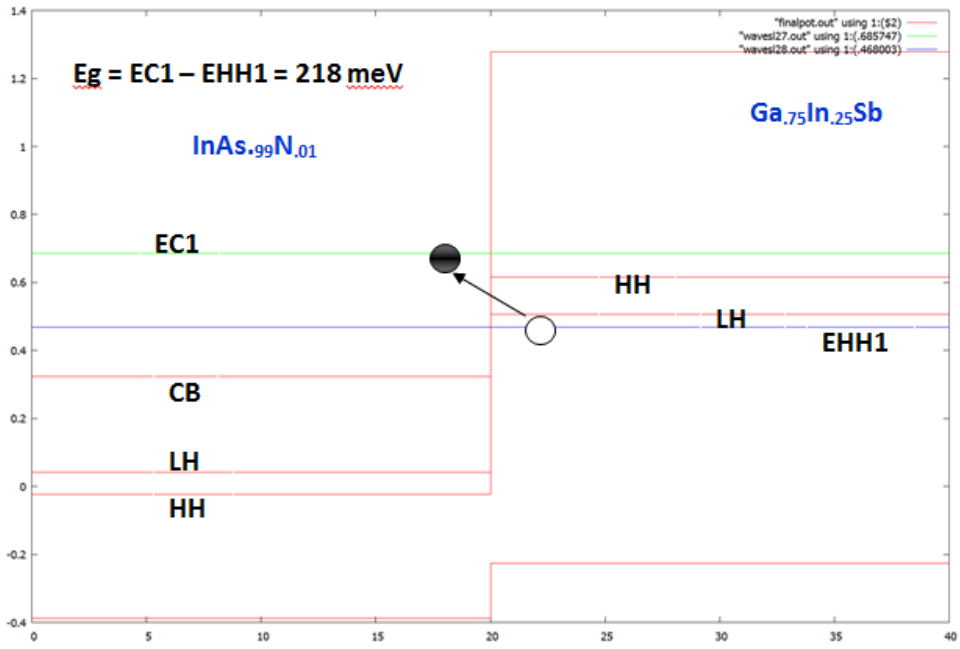

Figure 20 Simulated band alignment of $InAs_{.99}N_{.01}/Ga_{.75}In_{.25}Sb$, with a barrier and well length of 20Å

3.2.5 Comparison of InAs/GaInSb SLS with InAsN/GaInSb SLS. Figure 22 (a) shows the band alignment for an $InAs/Ga_{.85}In_{.15}Sb$ SLS. The InAs well is 30 Å thick while the $Ga_{.85}In_{.15}Sb$ barrier is 20 Å thick. Figure 22 (b) displays the band alignment for an $InAs_{.99}N_{.01}/Ga_{.85}In_{.15}Sb$ SLS. Some initial assumptions were made regarding the $InAs_{.99}N_{.01}$ parameter based on our prior work with other dilute nitride material systems namely GaInSbN, InSbN and GaSbN [5, 6, 8, 83].

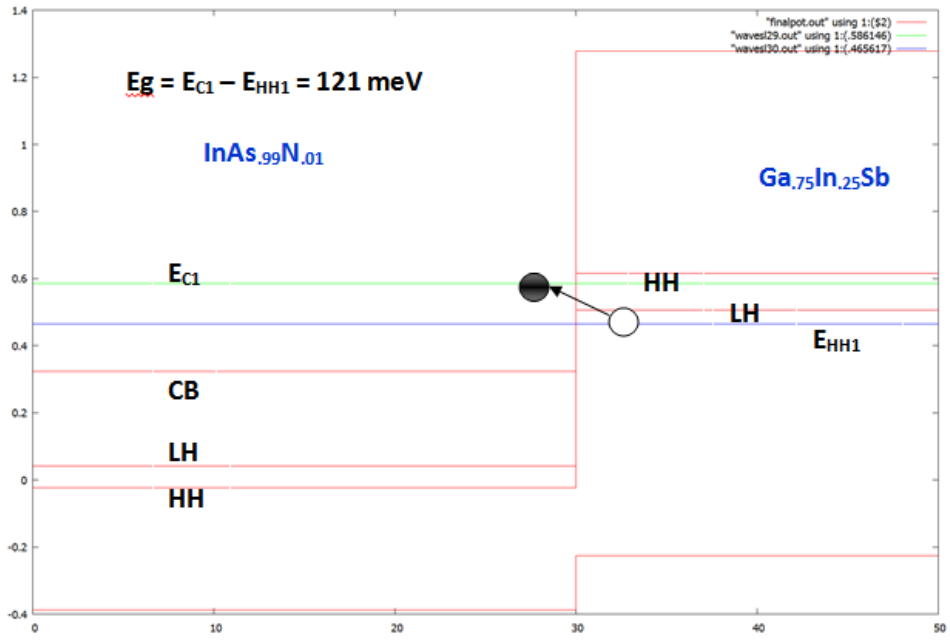

Figure 21 Simulated band alignment of $InAs_{.99}N_{.01}/Ga_{.75}In_{.25}Sb$, with a barrier length of 20 Å and a well length of 30 Å

The band alignment of 30 Å thick $InAs_{.99}N_{.0}$ well and 20 Å thick $Ga_{.85}In_{.15}Sb$ barrier was simulated (Figure 22 (b)). For a bandgap reduction of 70 meV with an addition of 1% N and marginal reduction in the lattice parameter, the simulation showed an increase in the in-plane strain. This strain caused increased splitting of the HH and LH in the GaInSb layer (compressive strain) and a reduction of the CB in the InAsN layer (tensile strain). This reduction of the InAsN CB in turn lowered E_{CB1} while the rise of the GaInSb HH increased the energy level of $E_{HH1.}$ Hence, the $InAs_{.99}N_{.01}/Ga_{.85}In_{.15}Sb$ SLS band gap was narrowed by 32 meV as compared to the InAs/GaInSb SLS for the same In concentration, and well and barrier thicknesses.

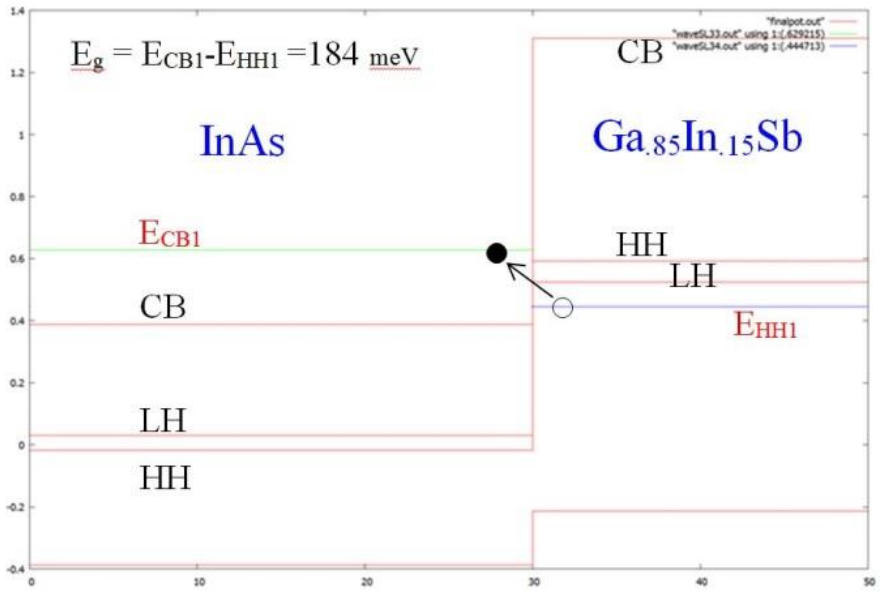

(a)

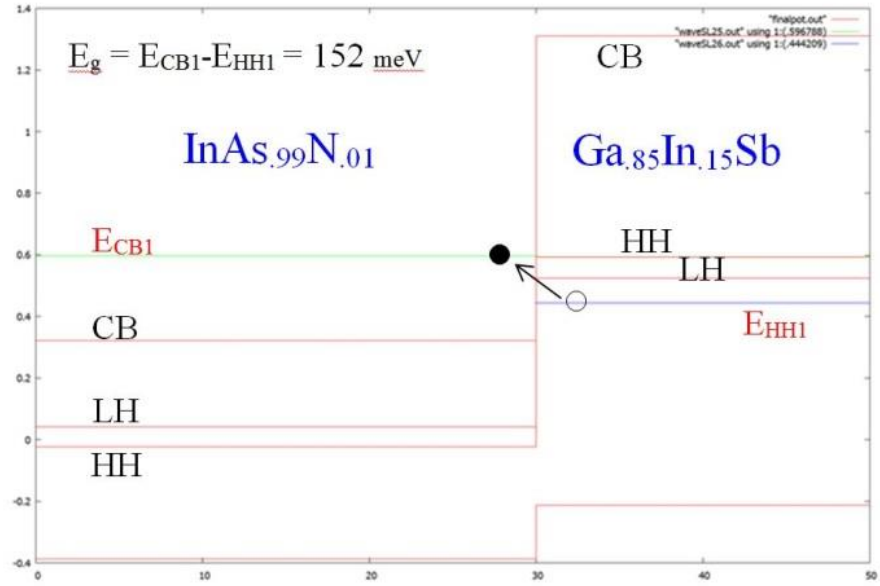

(b)

Figure 22 Simulated band alignment of SLS's using Optel software (a) $InAs/Ga_{.85}In_{.15}Sb$ SLS (b) $InAs_{.99}N_{.01}/ Ga_{.85}In_{.15}Sb$ SLS

It is to be noted that the above test values generated were at 4K as at higher temperature due to heavy overlapping of the wavefunctions the band gap could not be clearly discerned. Despite this drawback the software provided an overall trend and the relative amount of the energy band gap reduction with changes in different parameters which we used successfully as guideline to the growth of our samples described below.

3.3 Molecular Beam Epitaxy (MBE)

A Veeco EPI 930 solid source Molecular Beam Epitaxy (MBE) system (shown in Figure 23) was used in this study. The EPI 930 MBE was outfitted with five Knudsen effusion cells, one Sumo cell, two valve crackers, and a UNI-Bulb RF plasma nitrogen source. The arrangement of these cells (shown in Figure 24) displays the group III elemental sources outlined in blue, the group V elemental sources in red, the dopants in black, and the N plasma source in orange. The group III sources included 7N purity indium 1 (In1) and indium 2 (In 2) dual filament effusion cells. It is to be noted that there is no elemental difference between In1 & In 2as the nomenclature is only to distinguish one source from the other. Also in group III is a 7N purity gallium (Ga) dual filament SUMO cell which incorporated a specially designed 200 g crucible. The dual filament Ga SUMO cell was used in a hot-lip configuration which means the majority of the power is sent to the tip filament. The tip filament receiving majority power essentially means it is at higher operating temperature than the source material melt, where the primary filament is located. In this configuration the presence of oval defects has been reduced which is typically caused by the condensation and re-evaporation of Ga clusters at the lip of the crucible. In addition other benefits of a SUMO cell over a traditional dual filament effusion cell are the ability to have larger capacity of Ga (reduces MBE downtime due to source replenishing), good uniformity, and long-term flux stability, lower defect densities, and reduce shutter transients. The

only group III element in a single filament effusion cell was 7N purity aluminum (Al) which was not used in this study. The valved crackers mounted in the MBE were group V elements, arsenic (As) elements, arsenic (As) and antimony (Sb). By having a separate heating zone (filament) for the bulk and cracker regions both sources can operate in cracked or uncracked mode based on

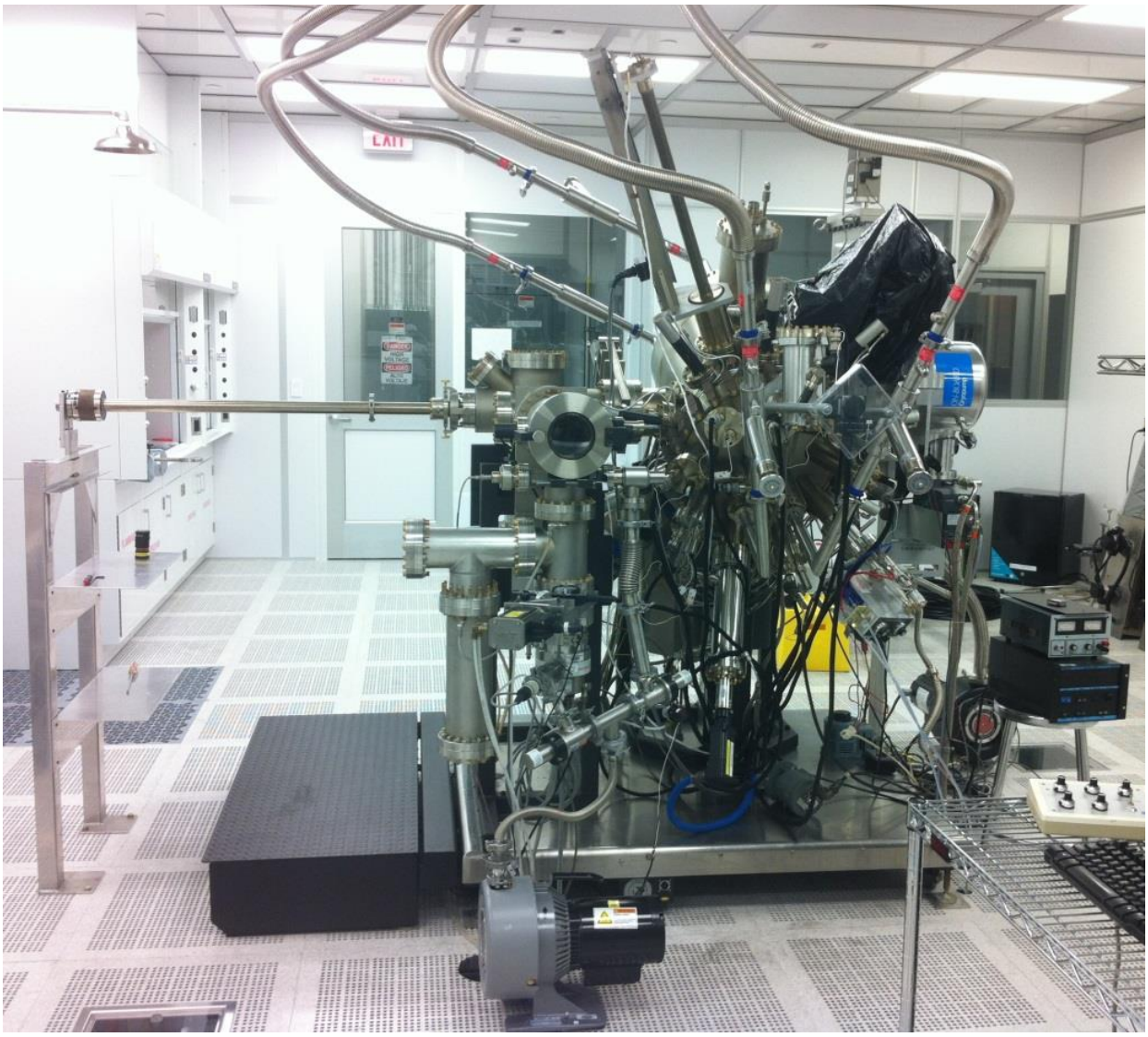

Figure 23 Veeco EPI 930 Molecular Beam Epitaxy (MBE)

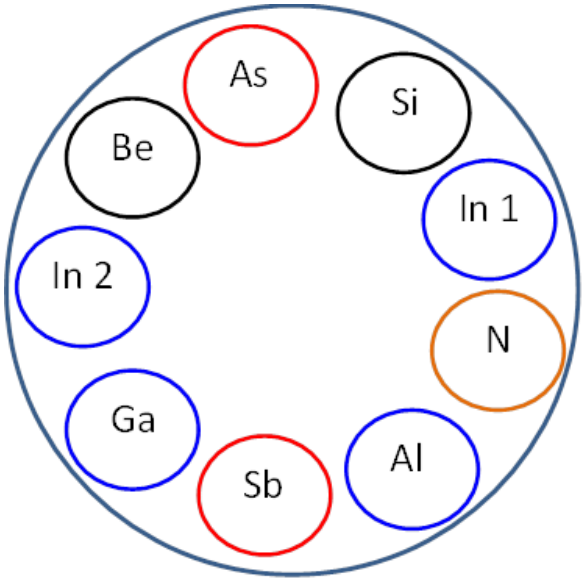

Figure 24 EPI 930 MBE source flange configuration

temperature. These crackers also have needle valves which regulate the beam flux in addition to temperature which provides exceptional uniformity and reduced waste. Each valved cracker was controlled independently by an automated valve positioner that provided quick response. Dopants were not utilized in this work, however, beryllium (Be) and silicon (Si) sources were available as p-type and n-type dopants, respectively. Furthermore, specifics of the Veeco EPI 930 MBE are reported elsewhere in the dissertations of Dr. Liangin Wu [86], Dr. Kalyan Nunna [87], and Dr. Sudhakar Bharatan [88].

3.4 MBE growth setup

3.4.1 <100> Gallium Antimonide wafer. Single crystal <100> tellurium (Te) doped (N-type) gallium antimonide (GaSb) wafers from Galaxy Compound Semiconductors, Inc. served as the substrate for all MBE growths done in this work. The 76.2 mm diameter wafers were 625 μm thick (+/-) 25 μm and were polished on both sides. These wafers are considered *ultra-low doped* (ULD) with a carrier concentration $\leq 2 \times 10^{17}$ cm^{-3} which improves optical transparency in the infrared region of interest, which is > 8 μm. The 76.2 mm wafers were diced into 10 mm^2 pieces.

The 10 mm^2 GaSb piece is sandwiched between a spring plate and a retainer plate. The plates are held together by a 3" molybdenum (Mo) block and a tungsten snap ring. This Veeco Uni-Block (shown in Figure 25) substrate holder creates easy mounting/unmounting of the GaSb wafers, fosters minimum wafer handling, cuts cost by allowing for more growths per wafer (due to the smaller size), and stimulates thermal uniformity during the MBE growths.

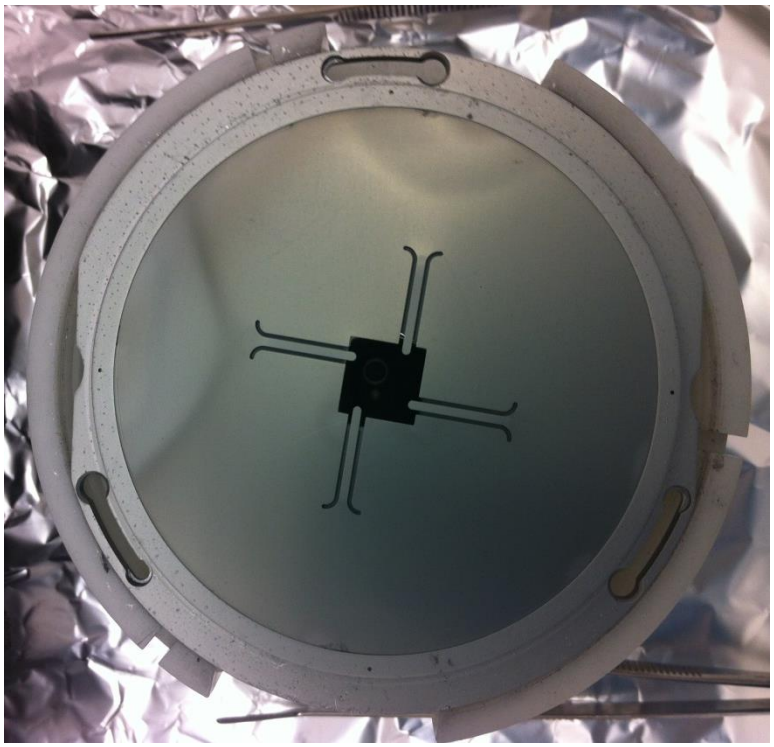

Figure 25 Veeco Uni-Block substrate holder

Prior to the growth process, the GaSb substrates were radiatively heated (baked) for 8 hrs. at 200 °C using two halogen lamps inside the introduction chamber. The pressure was maintained better than 10^{-7} Torr, to remove water vapor from the growth surface.

3.4.2 Nitrogen plasma. The UNI-Bulb RF plasma nitrogen (N) source was used to convert ultra-high purity N_2 gas into a more active atomic species. The source consists of a pyrolytic boron nitride (PBN) gas inlet tube and plasma bulb. The source also has two deflector

plates (shown in Figure 26) at the end of the plasma cell and a 100 hole (density) PBN aperture plate (also shown in Figure 26), for better conductance and uniformity. The N_2 gas flow was

Figure 26 RF plasma source deflector plates and aperture disc

controlled by a MKS 250 controller, 627B pressure transducer, 148J all metal flow valve, and a Varian manual leak valve. A manual RF matching network was used to minimize the reflected power through impedance matching the source for plasma stability. A view port is located on the external in of the plasma source so that the N plasma can be visibly seen as shown in Figure 27.

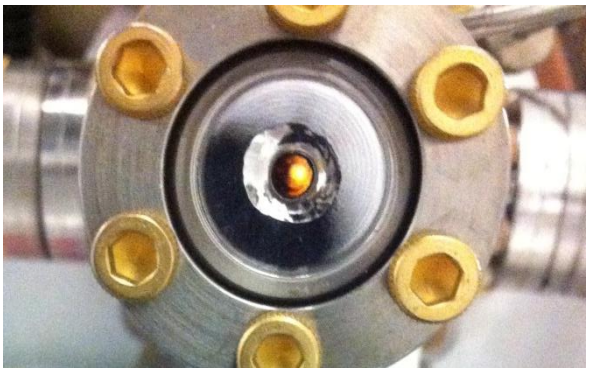

Figure 27 Nitrogen plasma

3.4.3 MBE growth procedure. After the GaSb wafers were baked for 8 hrs. at 200 °C, they were then transferred from the introduction chamber into the buffer chamber, which was maintained at a pressure ~10^{-11} torr. Liquid nitrogen (LN_2) was then started (which acts as a cryostat) and all applicable sources temperatures were increased from their idle temperature to their approximate growth temperature. Once the estimated growth temperatures were reached a beam flux monitor (BFM) was used to measure beam equivalent pressures (BEP) by individually opening pneumatic source shutters. The flux (beam) was measured for each source and the temperature and/or valve was adjusted for each source until desired flux values were achieved.

The BFM consist of a nude ion gauge which was lowered into the growth chamber and positioned where the substrate will later be placed for the growth. The dual filament Ga SUMO cell used this study had 95% of the power sent to the tip filament for all growths. Similarly, In 1 and In 2 had majority of the power directed to the tip at 90%. The As and Sb cracking zones were set at 900 °C for all growths done in this work. At that temperature As_4 was cracked to As_2 and Sb_4 was cracked to Sb_2. In all cases the cracker temperatures were raised and stabilized before the bulk temperatures were increased. The N plasma RF power was set at 300 W for all dilute nitride growths The BEP for the N plasma was controlled by the Varian manual leak valve and measured using the growth chambers ionization gauge. Before the introduction of N_2 gas, the ion pump gate valve was closed which left the cryopump to maintain ultra-low vacuum in the growth chamber. This was done to reduce unnecessary arcing in the ion pump caused by the volume of N_2 gas in the system which could possibly reduce its lifetime. The N plasma pneumatic shutter was opened after desired stabilization of N BEP and plasma which could be monitored by observing the brightness of the plasma through the view port. Finally, a -5 V bias

was applied to the deflector plates to minimize any damage that could induce defects in the layers, caused by high energy N plasma ions.

3.5 In-situ Characterization Techniques

3.5.1 Refraction High Energy Electron Diffraction (RHEED). The reflection high energy electron diffraction is a very powerful technique used during the MBE growth of thin films. This in-situ technique is very valuable due its non-destructive, real-time characterization during the growth. This technique uses a high energy (12 KeV) electron beam which is directed towards a sample at a grazing angle. Due to the low angle of incidence (~2°), the incidence beam only penetrates a few atomic layers before it gets diffracted onto a fluorescent screen creating a visual pattern. This visual diffracted beam pattern provides information on the behavior and atomic regularity at / near the surface. Therefore, the in-situ observation of the evolution of this pattern is used to understand the growth mechanisms. For example, an implication of a 2D or 3D growth can be made depending on if the RHEED pattern is streaky or spotty, respectively. This RHEED pattern can be recorded dynamically using a CCD camera connected to a computer for which individual images or continuous videos can be retained for detailed real-time or post growth analysis. Some examples of the analysis that can be done are determining the growth rate, lattice spacing / strain and determining the crystal structure. In this work, a kSA 400 analytical RHEED system manufactured by k-Space Associates, Inc. was used. This system included a 12-bit firewire camera, PCI-based digital frame grabber and the latest acquisition software (v5.13).

3.5.1.1 Determining the surface structure by RHEED. All growths were carried out on <100> Te doped GaSb wafers. A 10 mm^2 GaSb wafer was loaded on the substrate manipulator inside of the MBE chamber (growth chamber) and rotated at 30 rpm. The substrate heater was

increased to 561 °C to remove the native oxide layer from the surface of the wafer. It is to be noted that once the substrate temperature was above 400 °C the Sb valve and shutter was opened to provide a Sb overpressure. This was done because Sb desorbs above 400 °C and without overpressure of Sb would leave the substrate surface Ga-rich and rough. The process which is referred to as desorption is essential to grow structures with high crystalline quality. The desorption procedure is monitored by in-situ characterization technique RHEED. The RHEED pattern starts slightly spotty as shown in Figure 28 and slowly changes to a streaky pattern as shown in Figure 29 (a) and (b). A very bright streaky (1x3) pattern confirms an oxide free surface, which is then ready for the buffer layer to be grown on.

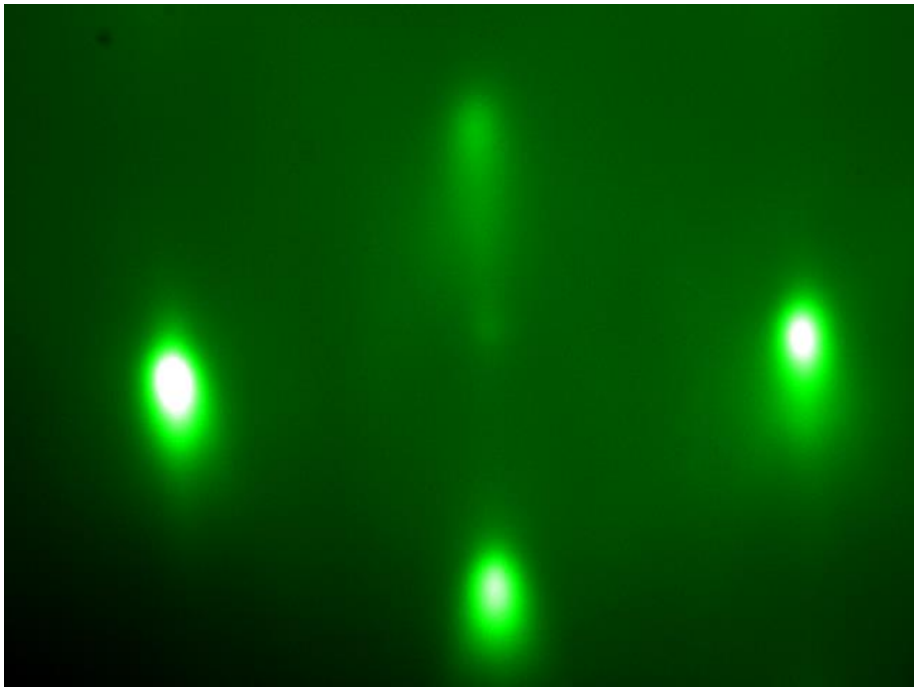

Figure 28 GaSb spotty desorption

The desorption process generally takes about 15 minutes after which the substrate temperature is lowered to 505 °C in preparation for the GaSb buffer layer. The GaSb buffer layer was grown to 0.3 µm thick for all samples in this work. The GaSb buffer provides a quasi-defect

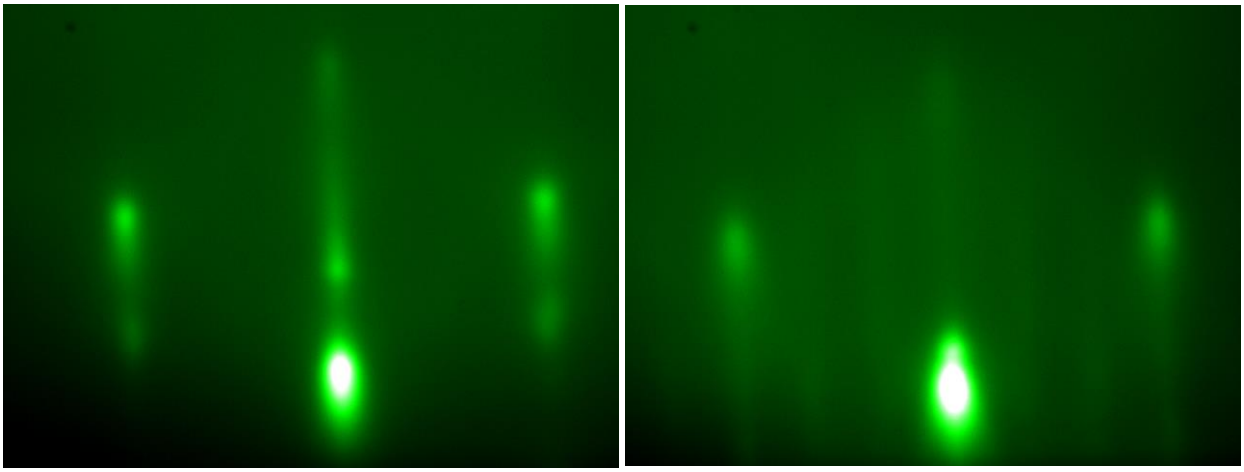

(a) (b)

Figure 29 (a) GaSb streaky desorption (1x3) RHEED pattern, and (b) rotated 90 °

free layer on which the SL structures are grown. The growth temperature for all superlattices was 405 °C. The growth temperature was monitored by a pyrometer which was calibrated by the well know [(1x3) → (2x5)] surface reconstruction of GaSb under Sb overpressure [89, 90] as shown in Figure 30. High quality streaky RHEED patterns were observed during the SL growths. For

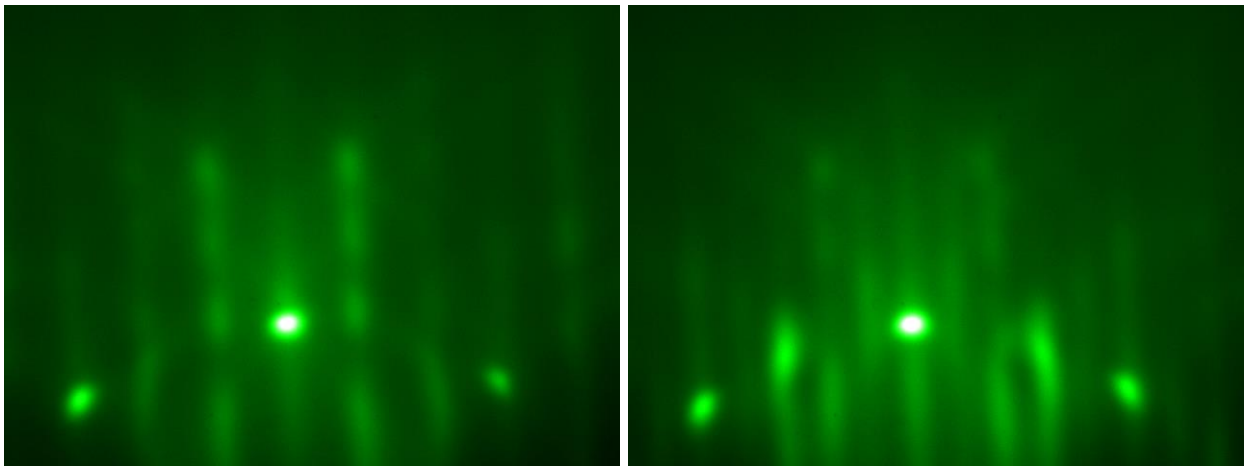

(a) (b)

Figure 30 GaSb surface reconstruction (a) x3 of (1x3) pattern, and (b) x5 of (2x5) pattern

example, Figure 31 shows a (2x5) streaky RHEED pattern for a GaInSb layer during a SL growth. Streaky RHEED patterns were also observed for the GaSb, InAs and InAsN layers (not shown) during the SL growths.

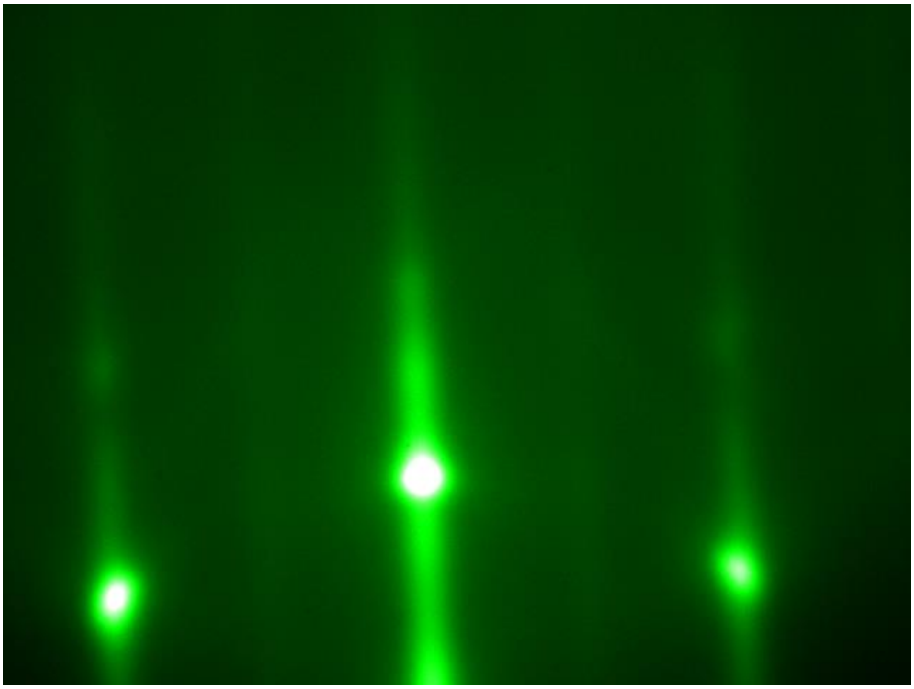

Figure 31 GaInSb (x2) RHEED pattern

3.5.1.2 Determining the growth rate by RHEED. To acquire the growth rate, real-time analysis and movies were taken to analyze the RHEED oscillations. These oscillations were observed at the beginning of the growth or a few seconds after the shutters are open. There are some undesired transients observed when the shutters are first open before usable oscillations are detected, as shown in Figure 32. Once the oscillations are obtained the analysis is started by cropping any unwanted transients as shown in Figure 33. The kSA software provided three different techniques to analyze the RHEED oscillations, specifically, fast Fourier transform (FFT), damped sine wave, and extrema count, which are shown in Figure 34, Figure 35, and Figure 36, respectively. These three growth rate techniques each exhibited advantages and

disadvantages independently but the software allows for the comparison of all three methods simultaneously, for the best accuracy possible.

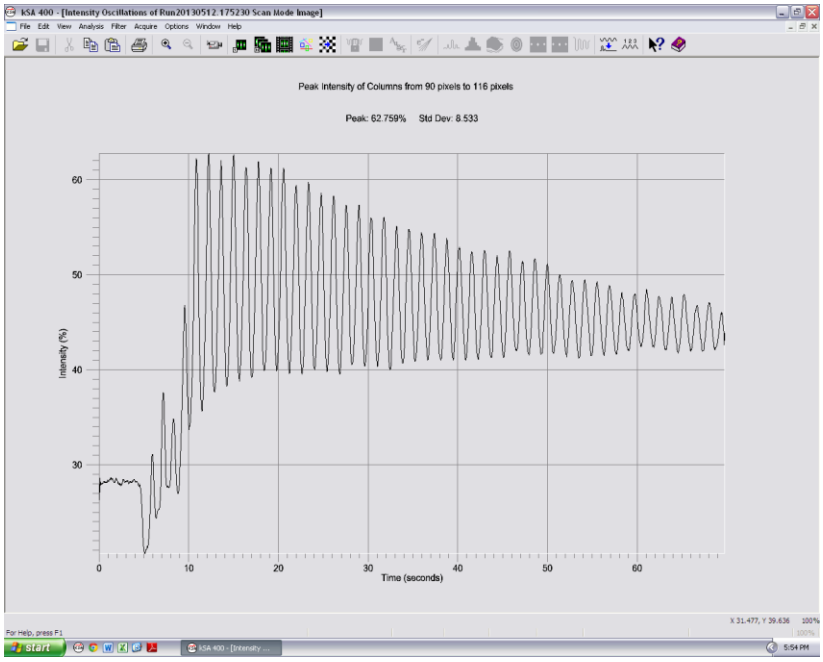

Figure 32 RHEED oscillations

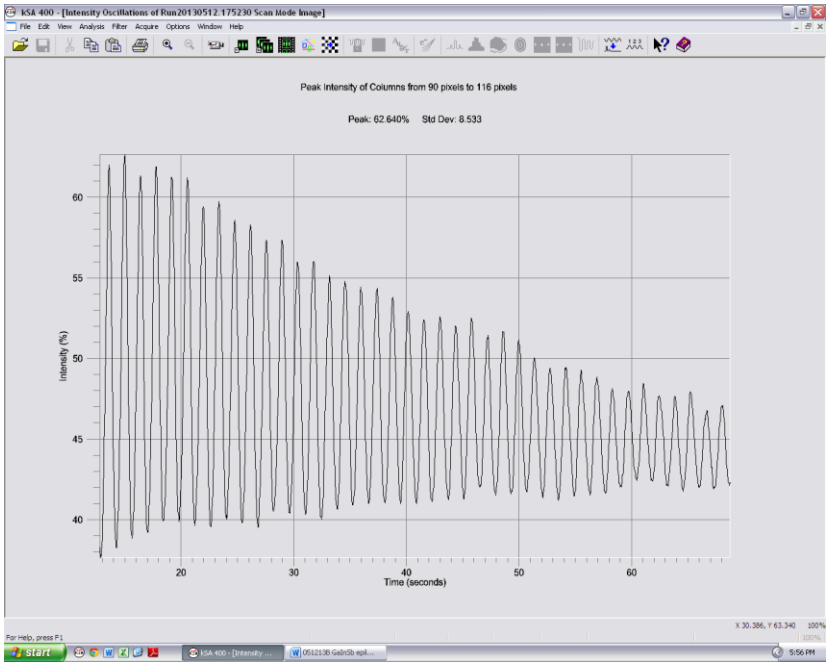

Figure 33 RHEED oscillations with the undesired transients cropped

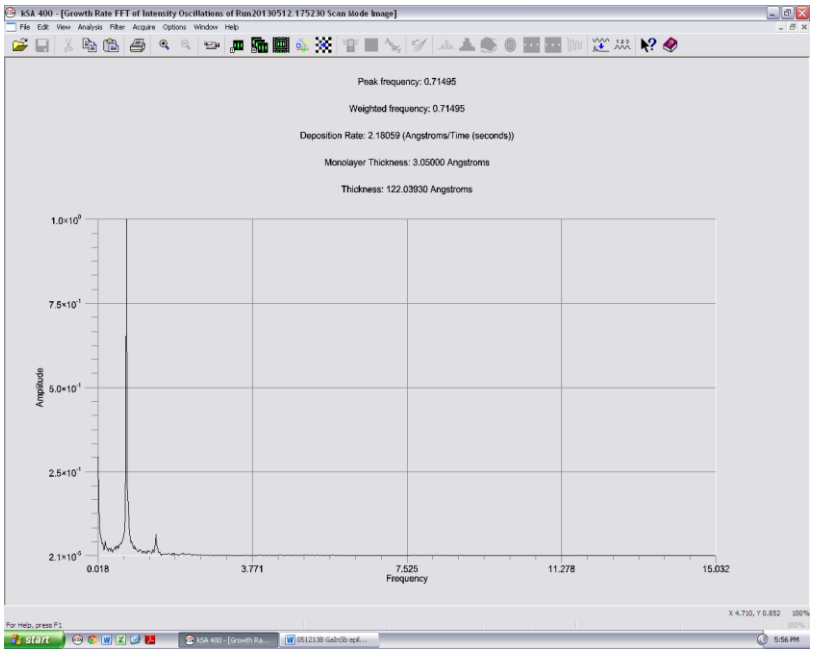

Figure 34 Results of growth rate FFT

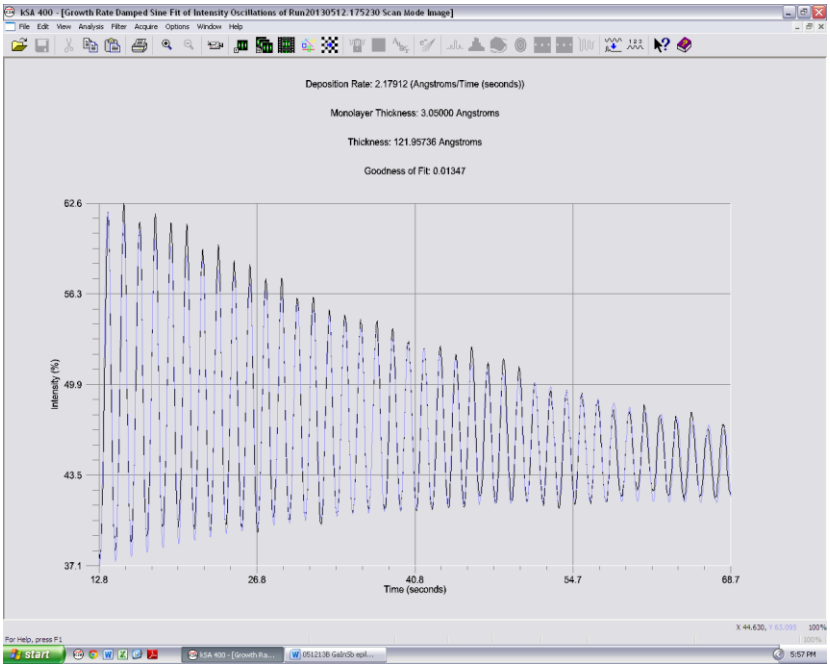

Figure 35 Results of growth rate of damped sine

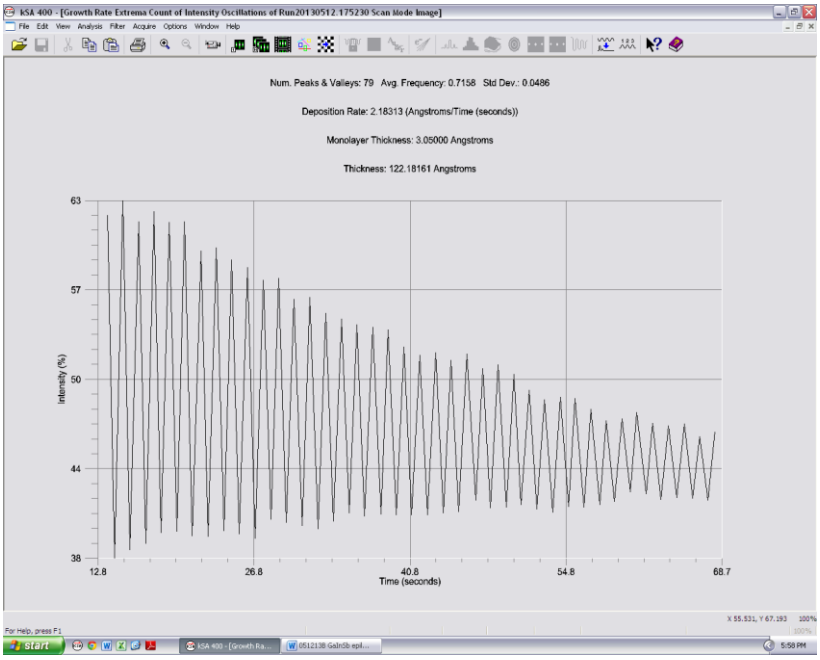

Figure 36 Results of growth rate extrema count

3.6 SLS Material System Optimization

3.6.1 SLS test structures. In this work several SL structures were grown and were varied in material composition, layer thickness, number of periods, and the number of compound materials (as shown in Figure 37 (a)-(d)). The SL material systems grown in this study were InAs/GaSb, InAs/GaInSb, InAsN/GaSb, and InAsN/GaInSb. The V/III BEP ratio was minimized to reduce As / Sb cross contamination, which is probable while switching between layers. The V/III BEP ratio in this study was 6 for Ga(In)Sb and InAs(N). The ratio was calibrated by streaky RHEED patterns which are indicative of a desired 2D growth. Also, a low growth rate was chosen (0.6 ML/s for GaSb and GaInSb and 0.5 ML/s for InAs(N)) for better growth control because of the thin layers required in this study (few monolayers). The low growth rate was also crucial in order to reduce the As background which can degrade the overall quality of the SL structure.

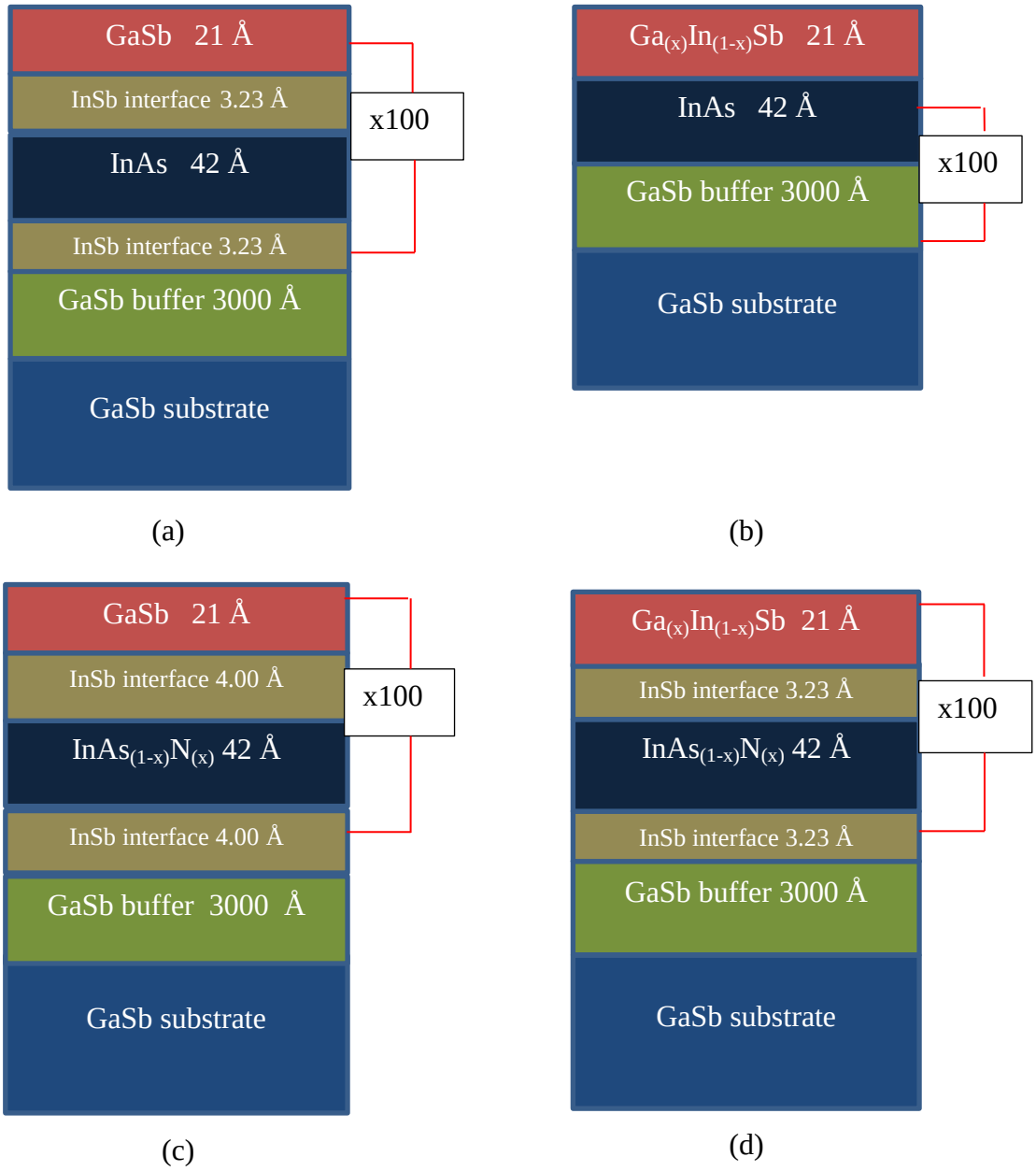

Figure 37 Typical SL structures grown in this study (a) InAs/GaSb, (b) InAs/GaInSb, (c) InAsN/GaSb, and (d) InAsN/GaInSb

3.6.2 Shutter sequence. The shutter sequence shown in Figure 38 was used as a model to grow the test SL structures. The shutters and cracker valves sequences were computer controlled for all of the SL growths. The computer programs were written specifically for each growth

done. The interfaces were controlled by soaking with As and or Sb or directly growing InSb and or GaAs as shown in Figure 38.

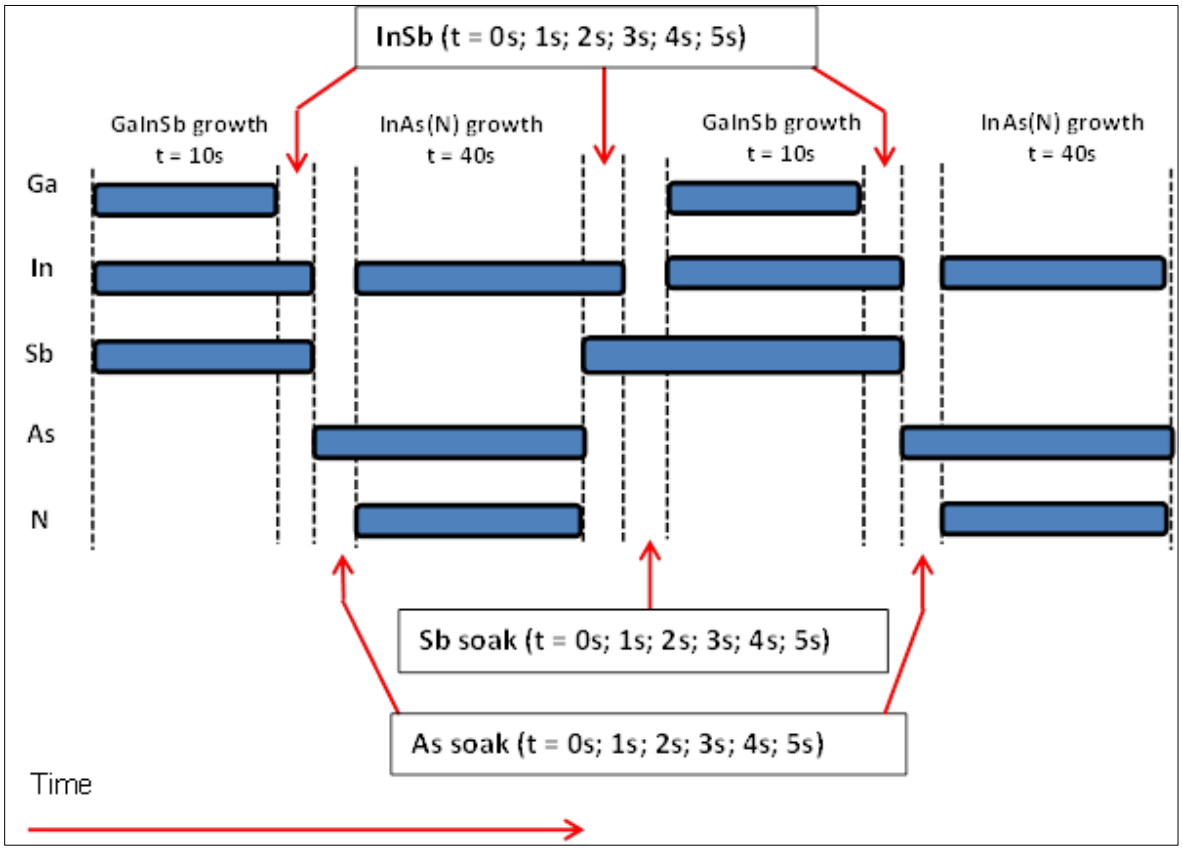

Figure 38 Shutter sequence for a typical SL growth

3.6.3 Strain balancing, intentional and unintentional interfaces. Strain balancing the SLs was extremely important for good crystalline quality and to prevent layer relaxation. Strain balancing the entire SL stack to the GaSb substrate depended on many factors, such as the number of layers, thickness of the constituent layers, and elemental composition of the individual layers. To achieve this, the interfaces between the fundamental layers were carefully controlled. For instance, three types of interfaces (IF) no intentional IF, GaAs IF and InSb IF were

methodically selected to attain the desired strain balance. Again, Figure *38* shows the model used to control the SL interfaces.

3.6.3.1 Influence of nitrogen (N) on strain balancing. Nitrogen added challenges to strain balancing the SL structure. This is because a dilute amount of N (< 1 %) lowers the band gap and reduces the lattice parameter of select III-V alloys which is also a function of the amount of N incorporated in the film. Therefore, with the lattice parameter varying with N incorporation several bulk $InAs_{(1-x)}N_{(x)}$ layers were grown on GaSb substrates to quantify the N incorporation. Hence, knowing the N incorporation was essential in proper strain balancing the InAsN/GaSb and InAsN/GaInSb SLs.

3.7 Conclusion

MBE growth technique was used for the growth of InAs/Ga(In)Sb and InAsN/Ga(In)Sb SL on GaSb substrates, due to its ability to precisely control the thermodynamic condition to favor the kinetics of high quality lattice matched alloy growth. By varying the shutter sequence various interfaces were grown with different techniques. RHEED was used to understand the surface construction and to determine the growth rate. Theoretical modeling software was used as an aid for faster growth turn around. Lastly, the effect of N on strain balancing the structure was summarized.

CHAPTER 4

Material Characterization Techniques

4.1 Introduction

This chapter will provide a description of the material characterization techniques and the experimental setup utilized in this work. After the samples were grown in the MBE system various techniques as described in this chapter were used to investigate the surface morphology, crystalline quality, elemental compositions, and optical properties. The grown samples were 10 mm x 10 mm in size and were cleaved to 10 mm x 5 mm because of the destructive nature of some techniques, specifically, STEM, and lapping / polishing, which was necessary for optical measurements. It is to be noted that some of the material characterizations were carried out by expert personnel from Evans Analytical Group Inc.

4.2 Rutherford Backscattering Spectrometry (RBS)

The RBS spectrum was acquired at a backscattering angle of 160° and an appropriate grazing angle (with the sample oriented perpendicular to the incident ion beam). The sample is rotated or tilted with a small angle to display a random geometry to the incident beam. This is done to avoid channeling in both the film and the substrate. The use of two detector angles can significantly improve the measurement accuracy for composition when thin surface layers need to be analyzed. Figure 39 shows the scattering geometry used in this RBS experiment and the analytical parameters are shown in Table 2.

Spectra are fit by applying a theoretical layer model and iteratively adjusting elemental concentrations and thickness until good agreement is found between the theoretical and the experimental spectra. The determination of layer thickness from RBS data requires making assumptions about the film densities. If the thickness of the films is known, the real density can

be calculated. Conversely, if the density is known RBS can provide accurate thicknesses. The equation governing the conversion from the RBS densities (D_{RBS}), RBS thicknesses (T_{RBS}) and real thicknesses (T_{real}) to the real densities (D_{real}) is given below in equation 1.2.

$$D_{real} = (D_{RBS} \times T_{RBS})/T_{real} \quad (1.2)$$

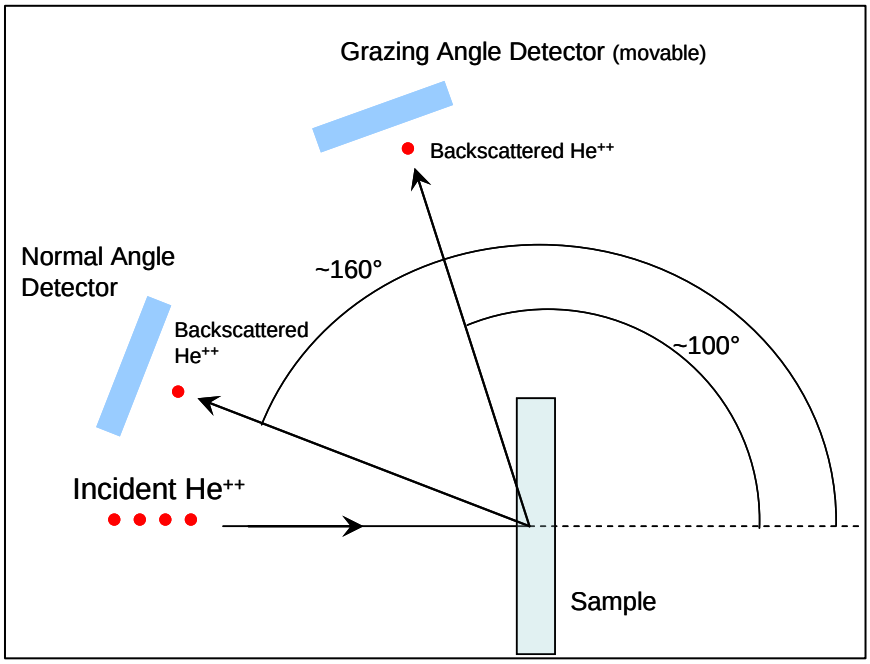

Figure 39 Scattering geometry in a typical RBS experiment

Table 2

Analytical Parameters: RBS

He^{++} Ion Beam Energy	2.275MeV
Normal Detector Angle	160°
Grazing Detector Angle	~100°
Analysis Mode	*CC RR*

4.3 Nuclear Reaction Analysis (NRA)

Ion channeling is an application of RBS in which the absence of backscattering signal is quantified. A crystalline sample is made up of regularly spaced and repeating atomic structures. In the macroscopic sense, it is possible to "see' through the entire crystal structure for the proper sample orientation. In an ion backscattering application, alignment of the incident beam with a major crystallographic axis will allow the incident ions to be "channeled" down the open regions of the crystal lattice. The probing ions are then "steered" down the rows of atoms, resulting in a reduction in backscattering yield with the minimum backscattering occurring when the sample is optimally channeled. For a channeled orientation, the incident ions can be transported to very great depths (>3-5 μm) from which backscattering events cannot be detected. In crystal Si, for example, there are many sample orientations that will allow channeling to be observed. Varying degrees of channeling will result in an increase of detectable backscattering events. Therefore, the degree of ion channeling can be quantified. If the crystal lattice contains either matrix or impurity atoms which are not in the crystal structure, that is, interstitial in the crystal structure, backscattering events can quantify the concentration of interstitial atoms (in units of atoms/cm^2). Thus, the range and the extent of damage from ion implantation, degree of crystal regrowth upon annealing, and the degree of impurity substitutionality / interstitiality can all be quantified in an ion channeling experiment.

Channeled and rotating random RBS spectra were acquired at detector angles of 160° and ~100° from the forward trajectory of the incident He ion beam. The grazing angle data provides improved depth resolution, while the 160° normal angle data allows a depth of up to 1μm to be measured. When the sample is moved in a rotating random orientation, the sample normal is precessed about the incident ion-beam. The backscattering spectrum from this orientation is

representative of a spectrum from a polycrystalline or amorphous sample and is normalized as the signal for 100% amorphization at all depths. The channeled spectra can then be compared to the rotating random spectra to yield quantifiable channeling parameters.

To improve C, N and O detection sensitivity and accuracy, nuclear reaction analysis (NRA) was used to measure C, areal density in our bulk grown samples. For N, the $^{14}N(d,p)\ ^{15}N$ reaction was used, $^{12}C(d,p)^{13}C$ for C, and $^{16}O(d,p)^{17}O$ for O. The proton yields from our grown were then compared to a standard sample with the known N, C and O contents to quantify N, C and O contents in the samples under study.

4.4 Atomic Force Microscopy (AFM)

The surface morphology was analyzed using an Agilent Technologies 5600 LS Atomic Force Microscope. The Agilent 5600 LS is equipped with a 200 mm x 200 mm fully addressable and programmable stage for ease of use including mounting / unmounting the samples. The system was used in automated tip mode to minimize damage to the sample surface during the scan. Image scan areas of 20 μm^2 and 5 μm^2 were done to observe the surface roughness and morphology. After the data acquisition AFM analysis was done using the free open source software Gwyddion.

4.5 X-ray Diffraction (XRD)

4.5.1 X-ray reflectivity (XRR)

X-ray reflectivity was used as to determine the thicknesses of the individual superlattice layers. The SL sample was mounted onto a glass slide with a piece of double-sided tape for analysis. The glass slide was then placed into the diffractometer. X-ray reflectivity (XRR) data was acquired with a PANalytical X'Pert Pro MRD 6-axis diffractometer equipped with a Copper x-ray tube and parallel-beam optics.

4.5.2 High resolution x-ray diffraction (HRXRD) and Reciprocal space mapping (RSM). The samples were mounted onto a glass plate with a small piece of double-sided tape which was then mounted onto the diffractometer. HRXRD data was acquired by Omega:2-Theta rocking curve near the GaSb (004) reflection and by 2-axis (Omega and Omega:2-Theta) reciprocal space maps (RSMs) near the GaSb (224) reflection. Data was acquired with a PANalytical X'Pert Pro MRD 6-axis diffractometer equipped with a Copper X-ray tube and hybrid (parabolic mirror plus 2-bounce Ge (220) crystal) monochromator. The HRXRD and RSM reflection scans were executed with different diffracted beam optics. The rocking curve data also known as double-axis geometry was acquired with a 1 mm fixed slit in front of the detector. The RSM data was acquired with a 2-bounce Ge (220) diffracted-beam monochromator instead, which is referred to as triple-axis geometry.

4.6 Scanning Transmission Electron Microscope (STEM)

A Hitachi HD-2700 Scanning Transmission Electron Microscope was used to determine the interfacial quality and layer thickness of the constituent layers of the SL samples. To prepare a cross-section using FIB, protective layers were added to the surface of the sample. A layer of carbon was first deposited onto the sample's surface; then a layer of platinum was sputtered using a K575X Emitech coating system. The sample was then placed in an FEI 200TEM focused ion beam (FIB) system. An additional layer of platinum was FIB-deposited by injection of an organo-metallic gas and rastering the 16kV gallium ion beam over the area of interest. A thin cross section measuring approximately 15 mm long, 2 mm wide and 10 mm deep was extracted from the die surface using a proprietary in-situ FIB technique. The cross section was attached to a 200 mesh copper TEM grid using FIB-deposited platinum. One window was thinned to

electron transparency using the gallium ion beam of the FEI FIB. The samples were wedged with 5kV Ga ion beam.

4.7 Raman Spectroscopy

The Raman measurements were performed with a Jobin Yvon spectrometer ("LabRam") equipped with a BX40 Olympus microscope in the backscattering geometry (180 °). A Helium Neon (HeNe) laser (632.8 nm wavelength) and an 1800 gr/mm grating were used in these measurements, which were repeated with an Argon+ ion (Ar+ ion) laser as well 514.5 nm wavelength).

Raman spectroscopy is the collection of light inelastically scattered by a material or compound. When a light of known wavelength strikes a material, the light is shifted according to the chemical functionalities of the material. The intensity of this shifted light depends on both molecular structure and macrostructure. As a result of these phenomena, the collection of the shifted light gives a Raman spectrum that can provide direct information regarding the molecular vibrations of the compound or material. We can then interpret this information to determine chemical structure, organization, and in some cases, non-covalent intermolecular interactions.

4.8 Fourier Transform Infrared Spectroscopy (FTIR)

Transmission and reflection measurements were carried out using a Varian/Agilent 670 FTIR spectrometer. A universal transmission holder by Harrick Scientific was used to hold the samples in place during the acquisitions. The samples were secured between two plates with 3 mm apertures for normal incidence measurements. A Harrick Scientific Seagull spectral reflection accessory was used for all reflection measurements. The reflection measurements were taken at an angle 5 ° from normal. The scan range for both transmission and reflection was from 6000 to 400 cm^{-1} or 1.6 to 25 μm.

4.8.1 Wafer Lapping/Polishing. All samples were backside thinned to between 50 and 100 μm in preparation for optical transmission measurements. As mentioned in the introduction of this chapter, half of the sample (10 mm x 5 mm) was used in this process. The samples were mounted to a South Bay Technology 150 lapping fixture with mounting wax. The backside of the samples was then thinned using the 150 lapping fixture with the 920 Lapping Machine, (shown in Figure 40) which was also purchased from South Bay Technology.

Backside thinning or lapping was necessary to reduce the infrared absorption from the 625 μm thick GaSb substrate. The GaSb substrate absorbs strongly in the LWIR and VLWIR regions (as shown in Figure 41 and Figure 42) which are the areas of interest in this work. Without thinning, the IR absorption from the film would be masked because the substrate is 1000 times thicker than the film. The low-doped wafers used in this work shown in Figure 41 has a much higher transmission (approximately 30 % higher) at 8 μm than that of a standard Te doped GaSb wafer, shown in Figure 42. The higher transparency aided significantly in the lapping process since the wafers did not have to be thinned as much as the regular Te doped GaSb to achieve the same transparency. This was very important in handling the samples during the measurements because of the brittle nature of GaSb.

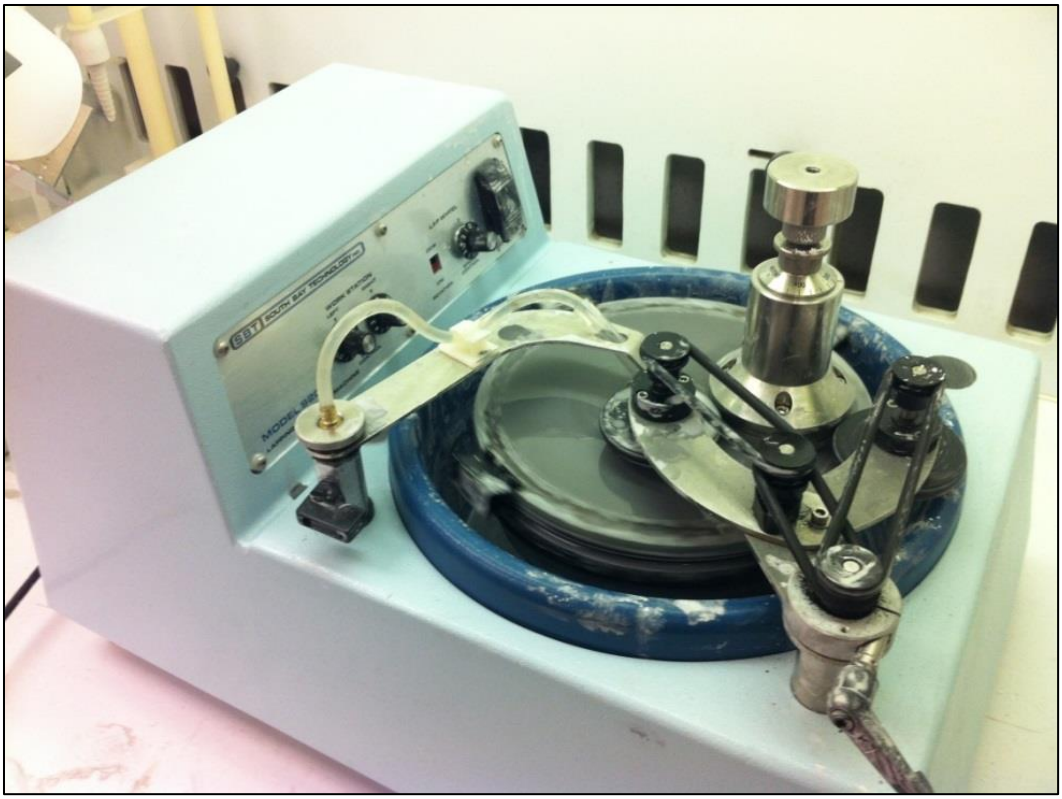

Figure 40 South Bay Technologies model 920 lapping machine and model 150 lapping fixture

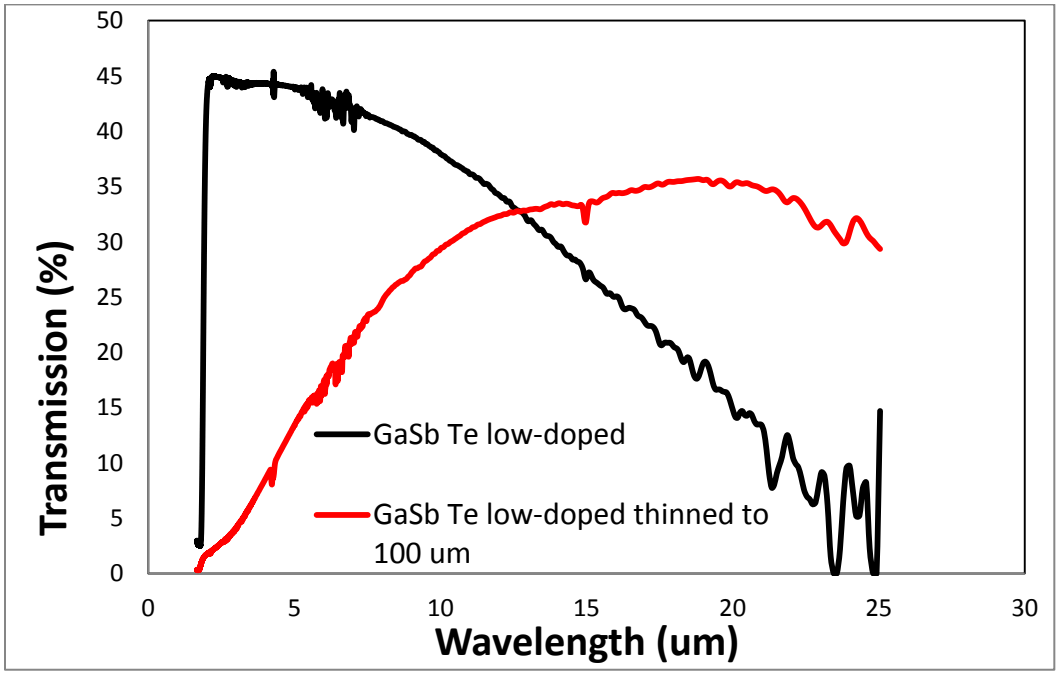

Figure 41 Transmission of Te low-doped 625 µm thick GaSb wafer and a Te low-doped GaSb wafer thinned to 100 µm

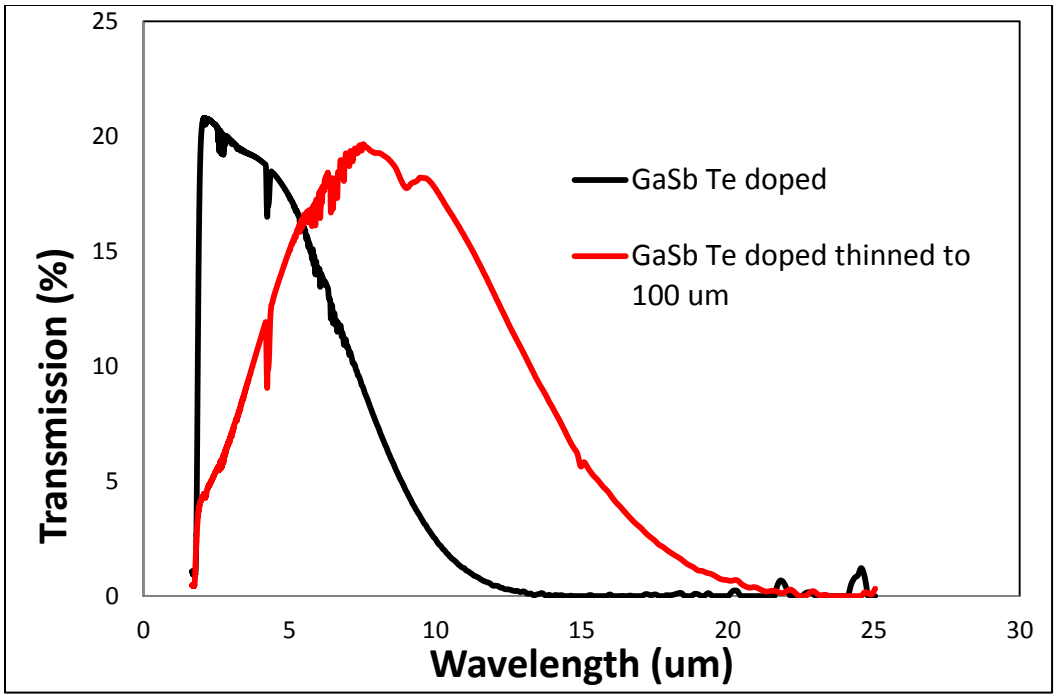

Figure 42 Transmission of Te doped 500 µm thick GaSb wafer and Te doped GaSb wafer thinned to 100 µm

4.9 Conclusion

This chapter discussed in detail the various material characterizations used in this work. These characterization techniques were used to determine the elemental composition, N incorporation, strain, crystalline quality, surface roughness, interfacial quality, and optical absorption.

CHAPTER 5

Material Characterization Results and Analysis

5.1 Introduction

The grown SL structures in the work were analyzed by various material characterizations. Namely, RBS and NRA for elemental composition, x-ray diffraction and Raman for crystalline quality, RSM for strain/relaxation, and STEM for layer thickness and atomic intermixing at the interface. These characterizations would provide insight to the SL's suitability for fabrication into IR detectors of high performance. The nomenclature for the SL samples studied in this work and its parameters are listed in Table 3 for simplicity.

Table 3

Nomenclature for SL samples studied in this work

Sample #	Material System	L_b (Å)	L_w (Å)	# Periods	InSb IF (Å)
SL1	InAs/ GaSb	21	42	100	1 ML
SL2	InAs/ GaSb	21	50	100	1 ML
SL3	InAs/$Ga_{.74}In_{.26}Sb$	21	42	100	not intentional
SL4	InAs/$Ga_{.74}In_{.26}Sb$	21	50	100	0.4 ML
SL5	$InAs_{.997}N_{.003}$/ GaSb	21	42	100	1 ML
SL6	$InAs_{.997}N_{.003}$/ $Ga_{.74}In_{.26}Sb$	21	42	100	0.4 ML

5.2 Rutherford Backscattering Spectrometry (RBS) Results and Analysis

A 2 µm thick $Ga_{(x)}In_{(1-x)}Sb$ bulk layer was grown on a GaSb substrate (same wafer used throughout this work). This ternary alloy was used as to verify the elemental compositions in the InAs/$Ga_{(x)}In_{(1-x)}Sb$ and $InAs_{(1-x)}N_{(x)}$/$Ga_{(x)}In_{(1-x)}Sb$ SL's. Figure 43 shows the RBS/channeling

spectra of $Ga_{(x)}In_{(1-x)}Sb$ bulk layer. The experimental spectra was fitted by applying a theoretical layer model while iteratively adjusting the concentrations and thicknesses until good agreement was found between the theoretical and the experimental spectra (shown in Figure 43). It is to be noted that the determination of the layer thickness from RBS data requires making assumptions about the film densities. The assumed densities used to calculate the film thicknesses are provided in Table 4. Since In and Sb have similar masses, resolution by RBS is not possible. Therefore, the Ga atomic percent (at. %) was directly measured and thus, indirectly yielded the In at. % based on the calculation In + Ga = 50 % with Sb being the other 50 %.

It is to be noted that the estimated uncertainty for the Ga, In, and Sb elemental compositions were within (+/-) 1 at. The composition of Ga in the layer was determined to be 37 at. %(Table 4) which translates to an alloy composition of $Ga_{0.74}In_{0.26}Sb$.

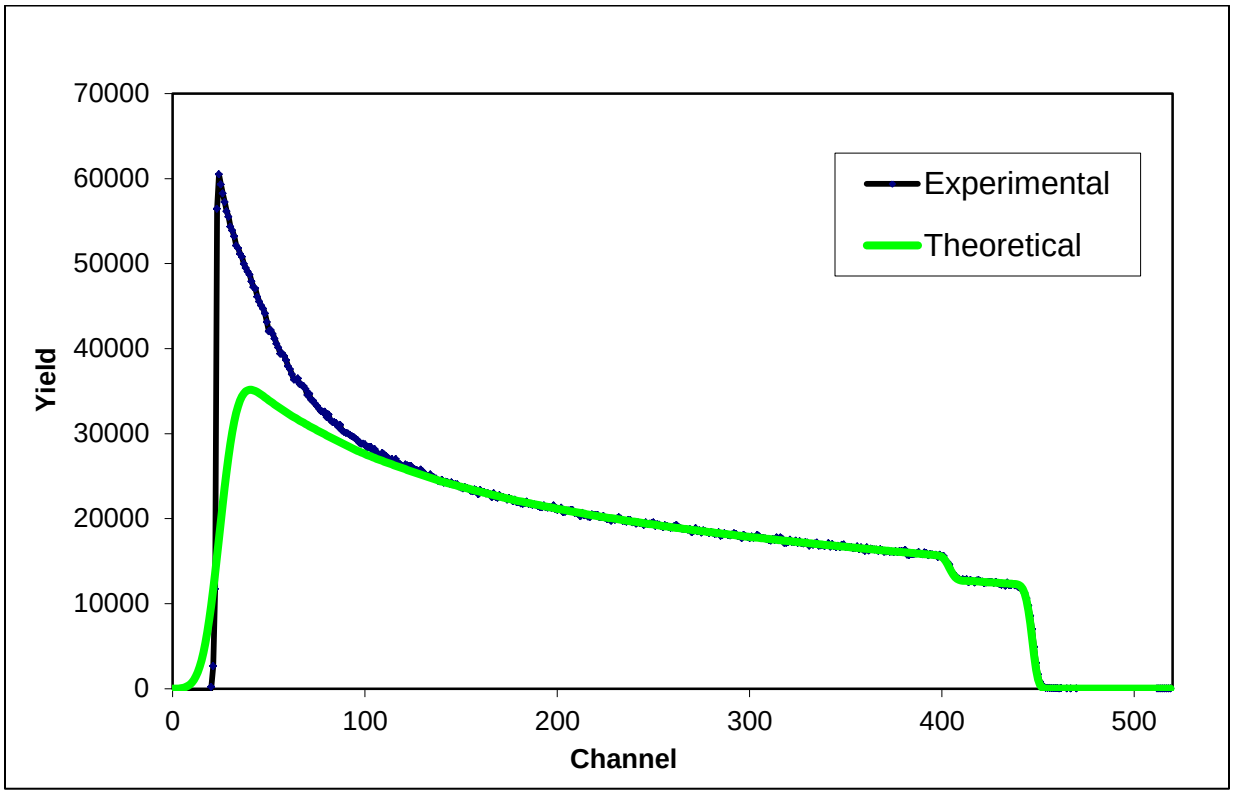

Figure 43 RBS theoretical fit to the experimental data

Table 4

Summary of the results from RBS

Thickness (Å)	**Atomic Concentrations (at. %)**			**Density (atoms/cc)**
	Ga	**In**	**Sb**	
< 20000	37	13	50	4.04×10^{22}

5.3 Nuclear Reaction Analysis (NRA) Results and Analysis

Nuclear reaction analysis (NRA) was used to verify the substitutional and interstitial N content in a 2 μm thick $InAs_{(1-x)}N_{(x)}$ epi-layer grown on a GaSb substrate. The spectrum was fitted by applying a theoretical layer model and iteratively adjusting the concentrations and thickness until good agreement is found between the theoretical and the experimental spectra, as discussed earlier for RBS spectra in section 5.1.

Channeled and random spectra of the $InAs_{(1-x)}N_{(x)}$ taken with NRA is shown in Figure 44. Significant reduction in the height of the aligned spectra of N relative to the corresponding random ones is indicative of the N being mainly on the lattice sites. The calculated amount of substutional atoms is 73%, however, the uncertainty in the ratio is large, anywhere between 60% to 80% due to the small intensity of the channeled spectra. In addition, the N areal density was found to be 5×10^{15} atoms/cm^2. O and C are also observed in the NRA spectra which are at channel 220 and 330, respectively. These are assumed to be atmospheric contaminants on the films surface and were not included in modeling the InAs layer.

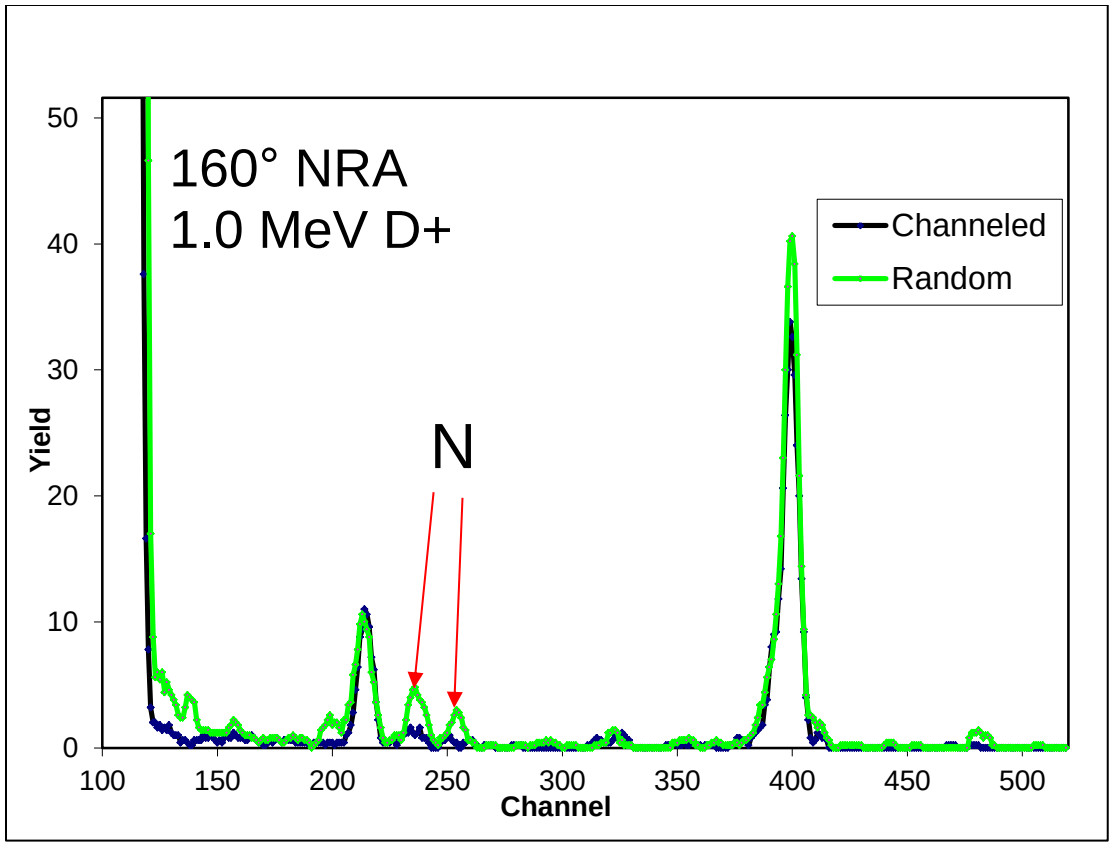

Figure 44 NRA theoretical fit to $InAs_{(1-x)}N_{(x)}$ epi-layer grown on a GaSb substrate

Table 5

Summary of the NRA results

	Thickness (Å)	**Atomic Concentrations (at. %)**						**Density (atoms/cc)**
		Si	**In**	**As**	**N**	**Ga**	**Sb**	
Epi-layer	4921	-	50	49.7	0.3	-	-	4.27×10^{22}
GaSb buffer	-	-	-	-	-	50	50	4.21×10^{22}

5.4 Atomic Force Microscopy (AFM) Results

The surface morphology of two different size scan images for all the samples were taken to get detailed information on the surface quality and signs of defects present in the sample. AFM images at two magnifications corresponding to 20 µm x 20 µm and 5 µm x 5 µm are shown for all the samples in Figures 45 - 47 to get both the micro and overall features. Figures 45, 46 and 47 display the morphology at the above two magnifications for the non-nitride binary pair (SL1,SL2), non-nitride with ternary barrier pair (SL3,SL4) and nitride pair (SL5,SL6), respectively.

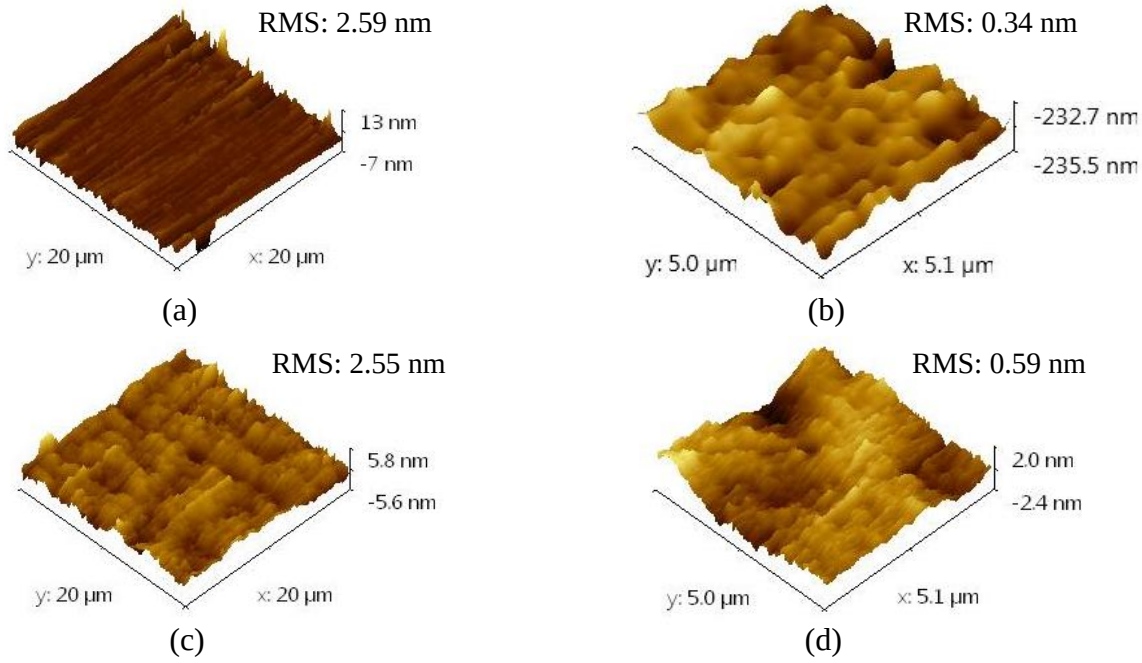

Figure 45 (a) shows the 20 µm x 20 µm and (b) the 5 µm x 5 µm AFM of SL1 (c) shows the 20 µm x 20 µm and (d) the 5 µm x 5 µm AFM of SL2

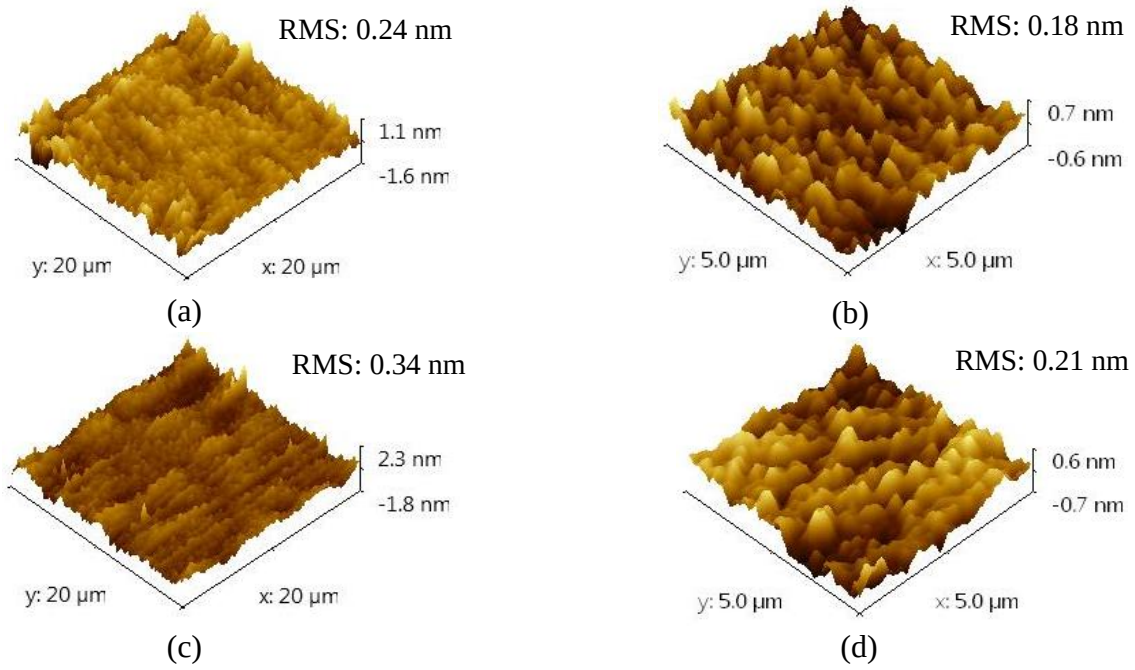

Figure 46 (a) shows the 20 µm x 20 µm and (b) the 5 µm x 5 µm AFM of SL3 (c) shows the 20 µm x 20 µm and (d) the 5 µm x 5 µm AFM of SL4

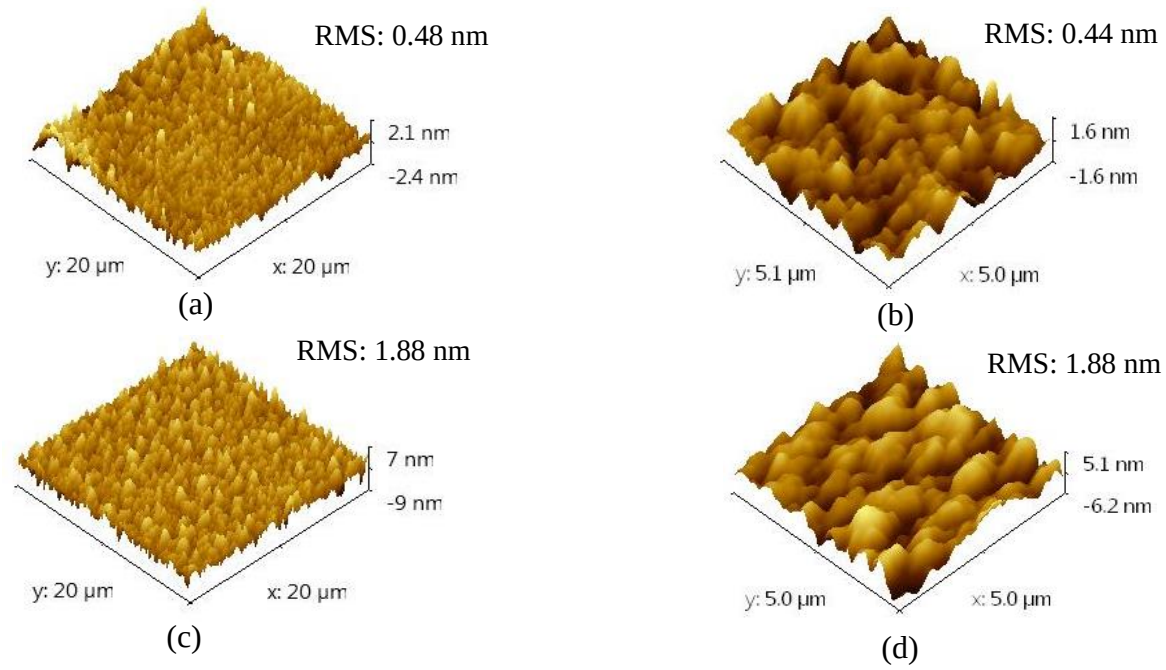

Figure 47 (a) shows the 20 µm x 20 µm and (b) the 5 µm x 5 µm AFM of SL5 (c) shows the 20 µm x 20 µm and (d) the 5 µm x 5 µm AFM of SL6

5.4.1 AFM analysis. The surface morphology of structures SL1, SL2, SL3, and SL4 (non-nitride grown samples) exhibits terracing indicative of a monolayer step growth. No macroscopic defects were observed in the high resolution 20 µm x 20 µm AFM scan image. Non-nitride SLs (Figure 45 (a-d) and Figure 46 (a-d)) display periodic undulations in the form of finger like structures orthogonal to the terracing. It is more pronounced and well defined in samples SL2 and SL4. The periodic surface modulation is more likely due to the local atomic ordering arising due to the tensile train within the SLs [47]. The terracing edges are more hillock and round shaped for samples SL1, SL2, and SL5 which all have a GaSb barrier. The SL3 and SL4 structures (InAs/GaInSb SL's) exhibits closely spaced terraces with terracing edges having finer features. The surface morphology of nitride SL's are quite different. The terracing is observed in structure SL5 (InAsN / GaSb SL) with the terraced edges being more jagged the latter being more pronounced in sample SL6 (InAsN / GaInSb SL) with no terracing. This is also reflected in the RMS roughness. The roughness varied from 0.24 nm being the lowest for sample SL3 to the highest value of 2.5 nm for sample SL2 for a 20 µm x 20 µm scan. The structures SL5 & SL6 (nitrides) had intermediate values though remarkably lower RMS roughness of 0.48 and 1.88 nm, respectively than the non-nitride sample SL2.

5.5 X-ray Diffraction Results and Analysis

5.5.1 X-ray reflectivity (XRR) results and analysis. XRR was performed only on one sample (SL1) to provide information on the constituent layers forming the SL. The XRR spectra of SL1 is shown in Figure 48. No thickness fringes were expected due to the total superlattice thickness exceeding 600 nm and quite low density contrast between the GaSb and the InAs. The observed peaks are Bragg diffraction peaks for the 1st through 7th order of the superlattice repeat thickness of approximately 6.95 nm. If each superlattice repeat structures were exactly the same,

in addition to strong, very sharp repeat layer peaks, additional weaker satellite peaks would be observed due to the repeating GaSb and InAs layers. The fact that the repeat layer peaks are observed, but the weaker satellite peaks are missing is an indication that the repeatability of the superlattice repeat structure is better than the repeatability of the individual layers within the repeat structure. Note also that the higher order superlattice peaks are broader and appear to be composed of numerous overlapped peaks. This suggests variation in the superlattice repeat thickness.

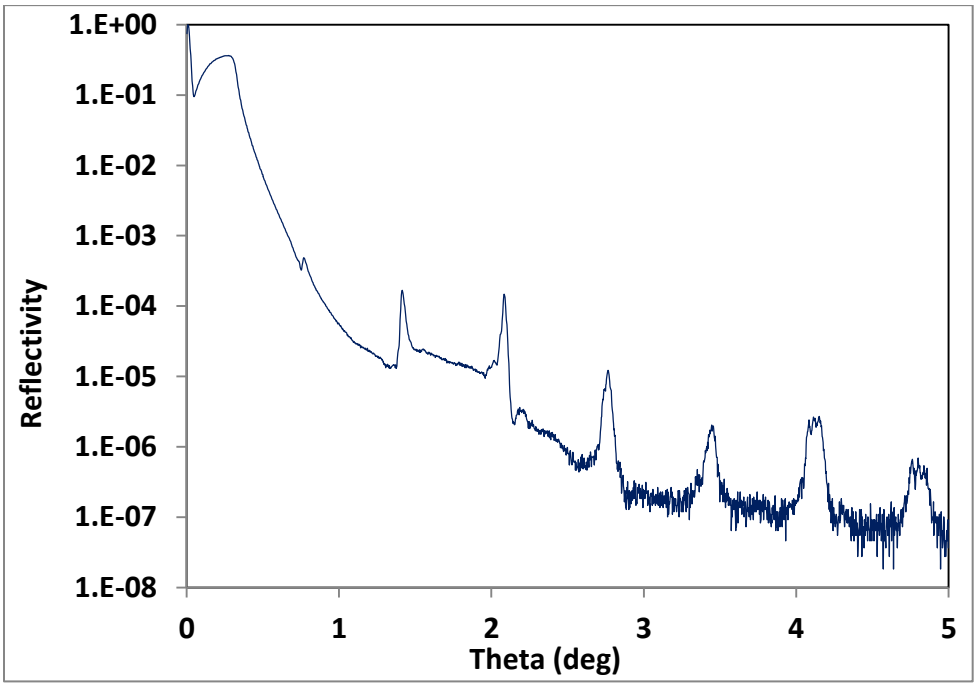

Figure 48 XRR data of sample SL1

Figure 49 compares the experimental data with a best fitting model. Since the variation in individual layer thicknesses is too numerically difficult to refine (potentially > 1200 adjustable parameters), four superlattice subunits of 25 repeat units were modeled (37 adjustable parameters). The details of the model are shown in the table beneath the figure and summarized in the table above. The fit (chi^2 = 18.4 %) is still quite poor. The agreement in position of the superlattice peaks is reasonable, but the fit to the background between peaks is poor. The model

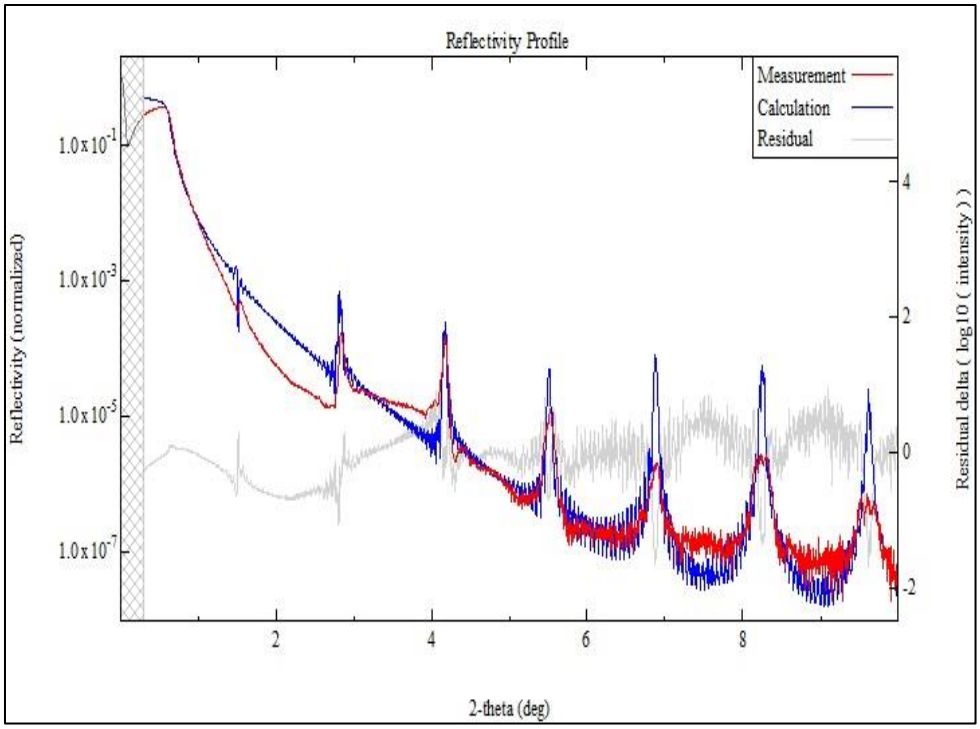

Figure 49 XRR data and simulation of sample SL1

also does not fit the width of the superlattice peaks. In addition, with so many layers being modeled by so few parameters, it is likely that these results are not unique. Nevertheless, the variation in each of the values may still be relevant. For example, the variation in the thickness of the total superlattice repeat unit is only 0.3% while the variation in the GaSb thickness is 14.5% and the variation in the InAs is 6.7%. Note also that while the thickness of the two InSb interface layers stayed close to the expected thickness, the GaSb and InAs layers are thinner than expected. This may indicate that the InSb simply diffuses into the bottom of the layer above so that the total thickness stays close to the nominal values. The fitting parameters from the simulation are shown in Table 6, while the final parameters are displayed in Table 7. It is to be noted that there is additional inaccuracy in the results due to the constraints imposed by the sample size. A large surface area is essential (on the order of 20 mm x 20 mm) due to the grazing

incidence of the x-ray. It was assumed that the other SL's in the work followed similar behavior and were not measured with XRR.

Table 6

Sample SL1 simulation parameters from XRR

Layer	**Density (g/cm^3)**	**Thickness (nm)**	**Roughness (nm)**
GaSb – 1	5.34	2.04	0.46
InSb – 1	5.63	0.46	0.01 **F**
InAs - 1	5.55	3.58	0.01 **F**
InSb - 2	5.95	0.36	0.01 **F**
GaSb – 2	5.27	2.08	0.42
InSb – 3	5.20	0.32	0.01 **F**
InAs – 2	5.20	3.76	0.01 **F**
InSb – 4	5.65	0.26	0.01 **F**
GaSb – 3	6.40	1.50	0.64
InSb – 5	5.87	0.33	0.01 **F**
InAs – 3	5.66	4.19	0.01 **F**
InSb – 6	5.60	0.42	0.01 **F**
GaSb – 4	6.02	2.08	0.48
InSb – 7	5.44	0.18	0.01 **F**
InAs – 4	5.73	3.93	0.01 **F**
InSb – 8	5.80	0.28	0.01 **F**
GaSb – 5	5.62 **F**	300 **F**	0.60
GaSb Substrate	5.62 **F**	----	0.50 **F**
F indicates a fixed parameter in the model refinement			

Table 7

Sample SL1 final parameters from XRR

Sample	Layer	Density (g/cm^3)	Thickness (nm)	Roughness (nm)
SL1	GaSb – layer 1	5.75 +/- 0.55	1.93 +/- 0.28	0.50 +/- 0.10
	InSb – layer 2	5.68 +/- 0.36	0.32 +/- 0.11	n/a
	InAs –layer 3	5.53 +/- 0.25	3.87 +/- 0.26	n/a
	InSb –layer 4	5.75 +/- 0.16	0.33 +/- 0.07	n/a
	GaSb - 1	5.62 **F**	300 **F**	0.61
	GaSb Substrate	5.62 **F**	----	0.50 **F**
	Total SL	----	6.44 +/- 0.02	----
F indicates a fixed parameter in the model refinement				

5.5.2 HRXRD and RSM results and analysis. Symmetric (004) reflection HRXRD scans were done to verify the elemental composition and crystalline quality of 100% relaxed $Ga_{(x)}In_{(1-x)}Sb$ on GaSb substrates. From HRXRD simulation (not shown), the mole fraction of Ga was determine to be 72 % (x = 0.72) with In being 28%. The findings from this HRXRD simulation closely match the outcomes from RBS as discussed in section 5.2. In addition, the lowest FWHM or best crystalline quality was found to be for $Ga_{(x)}In_{(1-x)}Sb$ epi-layers with a V/III BEP of 6.

Reciprocal space maps near the asymmetric GaSb (224) reflection were used to determine whether the various layers were pseudomorphically strained to lattice match the substrate or showed evidence of relaxation. Figure 50 shows the real space GaSb (224) RSM for sample SL1. This map covers 2 degrees in ω/2-θ on the horizontal axis and 2 °in ω on the vertical axis. The step size in ω/2-θ was 0.005 ° while the step size in ω was 0.02 degrees. The dwell time for each point was 1.2 seconds with the total scan running to 13.75 hours for one RSM. The bright spot in the center is from the GaSb substrate while the two spots to either side are the SL -1 and SL +1 superlattice peaks. There also appears to be a streak running between the three peaks. The locations of each peak are shown in the table beneath the figure. Also included is the width of these peaks in both the ω and ω/2-θ directions. Note that this map is plotted using a log intensity scale so the width of the observed peaks appears wider than they actually are. Interpretation of a real space RSM is difficult because lattice matched peaks will appear in a line between the (224) peak and the origin (000). Whether a sample is lattice matched is easier to determine by viewing the same data in reciprocal space. Figure 51 shows the data for sample SL1 in reciprocal space units. The vertical line encompasses both the substrate and the two superlattice satellite peaks indicative of growth of pseudomorphic SL layers grown on the substrate. Figure 52 shows that the streak between the substrate and superlattice peaks is actually composed of a number of sharp peaks. These are interference fringes due to the superlattice thickness similar to those observed in x-ray reflectometry (XRR).

Figure 53 shows the ω/2-θ rocking curve acquired near the GaSb (004) symmetric reflection. This scan covers a 15 degree range with a 0.001 degree step size and a 1 second dwell time. Seven superlattice peaks are observed on either side of the SL0th peak. The details of peak position, width and intensity are shown in the figure beneath the Table. Figure 54 is an expanded

view showing the SL -5, SL -6 and SL -7 superlattice satellite peaks. Note that these higher angle peaks are actually envelopes of close together peaks. It is not clear what causes this structure although the most likely reason due to the presence of different periods within the SL due to the small changes in repeat thicknesses as a function of depth. Normally this tends to affect the higher order satellite peaks more than the lower order, which is consistent with our observation. XRR data Figure 48 acquired on this sample also attest to this conjecture.

Figure 55 shows the experimental rocking curve data and the best model fit to these data. Modeling was done using the PANalytical Epitaxy 4.3 software package with simulated annealing. The details of the model are shown in the table beneath the figure. It is not possible to separate composition from relaxation in double-axis rocking curve data so the composition of the thicker layers was allowed to vary while the strain in the InSb buffer layers was allowed to vary. The thicknesses of all four sublayers were allowed to vary along with background and scale factor for a total of ten adjustable parameters. While the model is fairly simple, the wide range of $\omega/2\text{-}\theta$ covered resulted in refinement times ranging from 3 to 10 hours. While the positions of the observed peaks fit quite well and the relative peak intensities of the superlattice peaks are generally correct, this model does not account well for the width of these superlattice peaks. The results indicate that the total superlattice repeat thickness is close to the combined nominal thicknesses of the GaSb and InAs sublayers. This suggests that the InSb interfacial layers diffuse into the adjacent layers rather than remaining distinct layer. This is most clearly seen in the composition of the GaSb sublayer which was shown to actually be $Ga_{0.942}In_{0.058}Sb$.

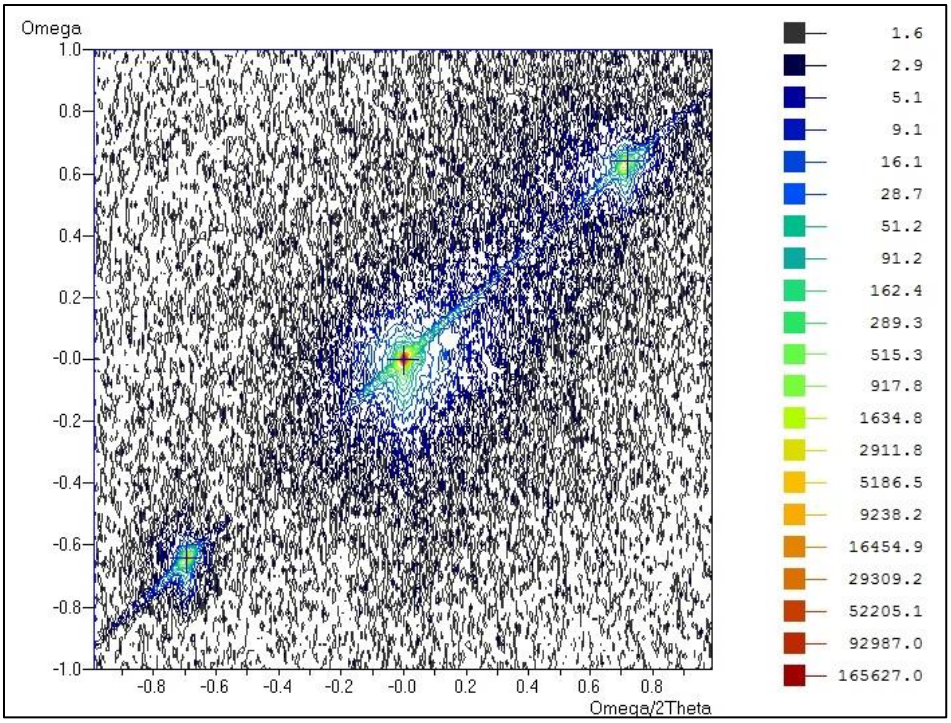

Figure 50 RSM (224) reflection for sample SL1

Table 8

SL1 parameters from RSM (224) reflection

Peak	Omega	2Theta	Qx (rlu)	Qy (rlu)	FWHMx (deg)	FWHMy (deg)	d-spacing (Å)
Substrate	2.6570	76.6041	0.36120	0.50368	0.0128	0.0205	1.24281
SL -1	1.3220	75.2141	0.36114	0.49191	0.0128	0.0208	1.26228
SL +1	4.0170	78.0441	0.36118	0.51572	0.0194	0.0250	1.22344

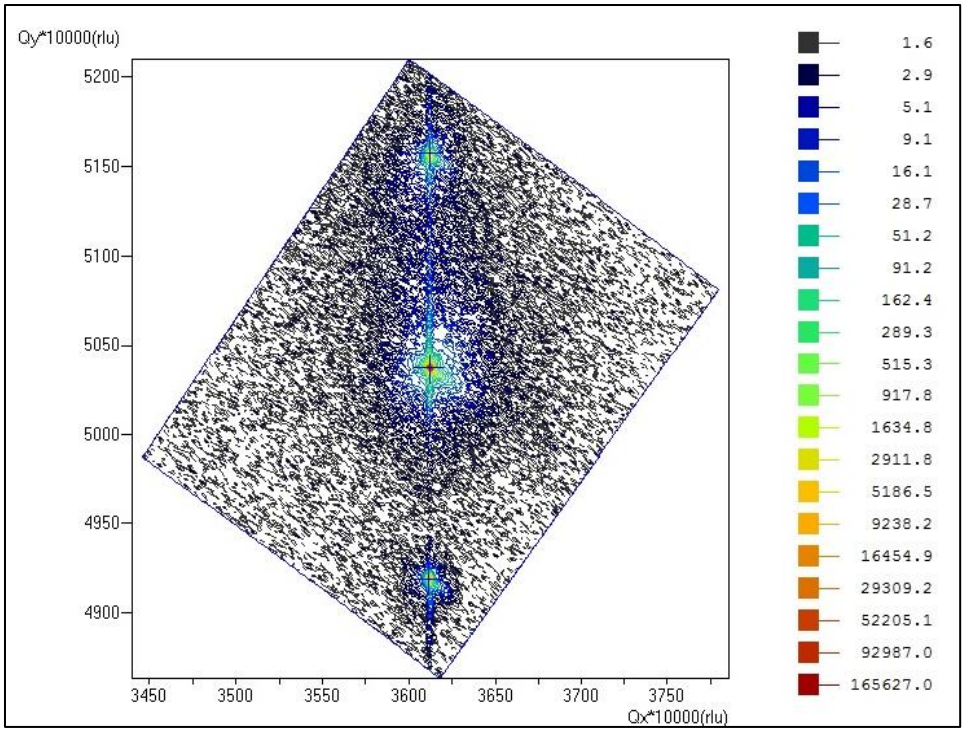

Figure 51 RSM (224) reflection in reciprocal space units for sample SL1

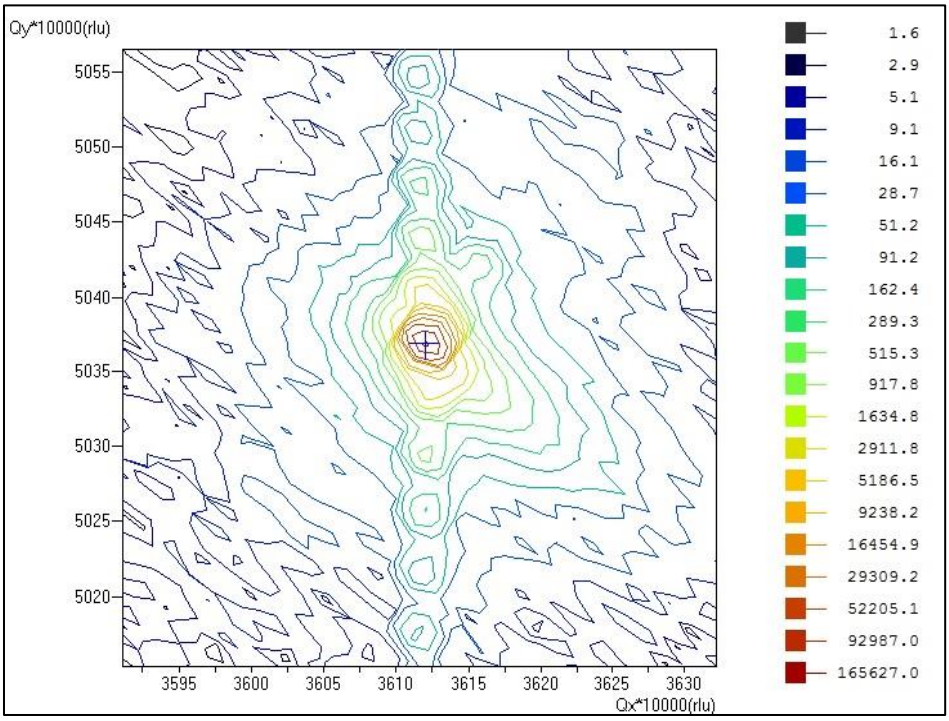

Figure 52 RSM (224) reflection in reciprocal space units for sample SL1– Expanded view near substrate

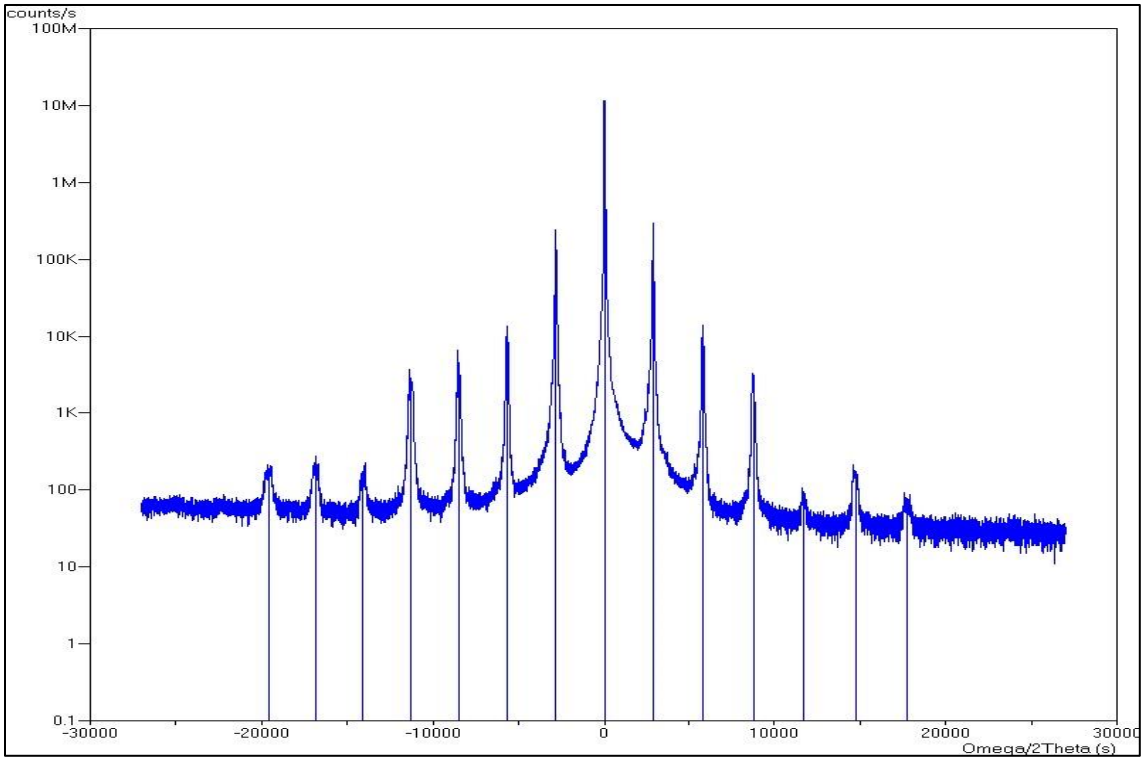

Figure 53 HRXRD (004) ω/2-θ rocking curve for sample SL1

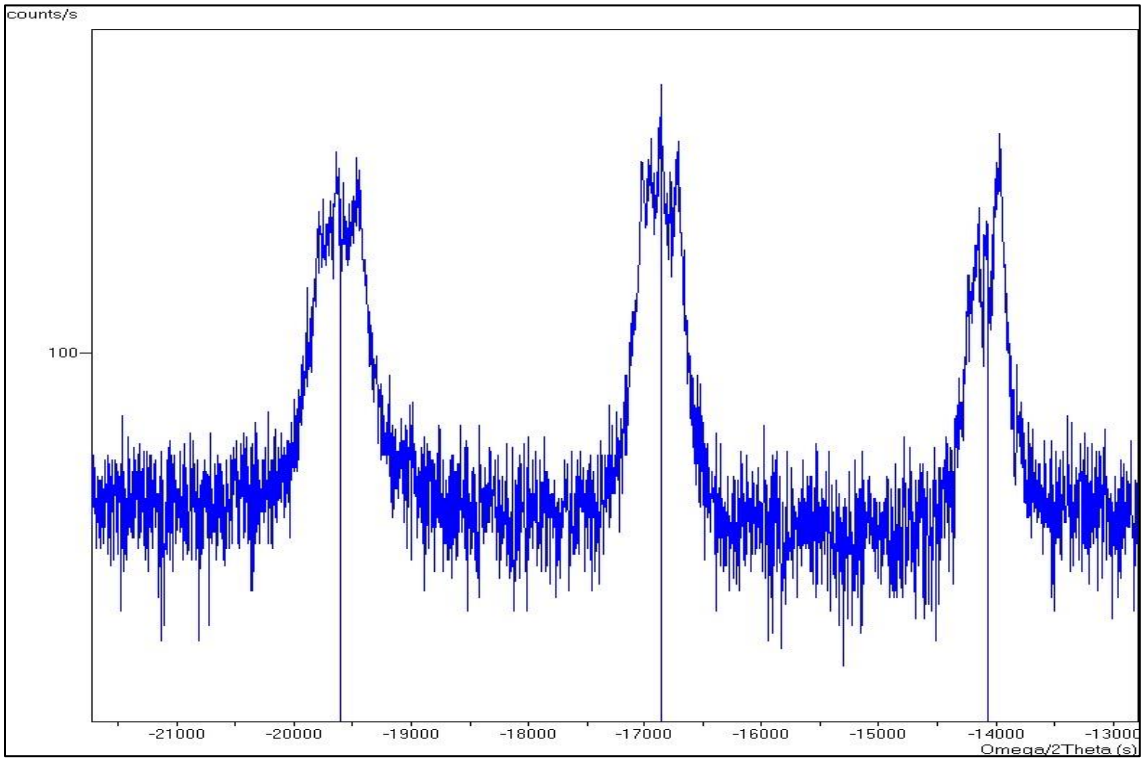

Figure 54 HRXRD (004) ω/2-θ rocking curve for sample SL1 – Expanded view

Table 9

Parameters from HRXRD (004) scan for sample SL1

Peak	**Omega (deg)**	**2Theta (deg)**	**Width (deg)**	**Intensity (cps)**
Substrate	30.0077	60.7074	0.0090	1.168e+7
SL 0	30.0190	60.7300	0.0230	3.419e+6
SL +1	30.8235	62.3389	0.0141	3.016e+5
SL +2	31.6302	63.9524	0.0290	1.417e+4
SL +3	32.4486	65.5891	0.0642	2.146e+3
SL +4	33.2650	67.2219	0.1327	7.013e+1
SL +5	34.1039	68.8997	0.1241	1.212E+2
SL +6	34.9444	70.5808	0.1812	6.827e+1
SL -1	29.2205	59.1329	0.0171	2.427e+5
SL -2	28.4353	57.5626	0.0384	8.055e+3
SL -3	27.6476	55.9867	0.0763	2.114e+3
SL -4	26.8714	54.4347	0.0909	1.783e+3
SL -5	26.0987	52.8894	0.1104	1.561e+2
SL -6	25.3257	51.3433	0.0776	2.661e+2
SL -7	24.5566	49.8050	0.1354	1.934e+2

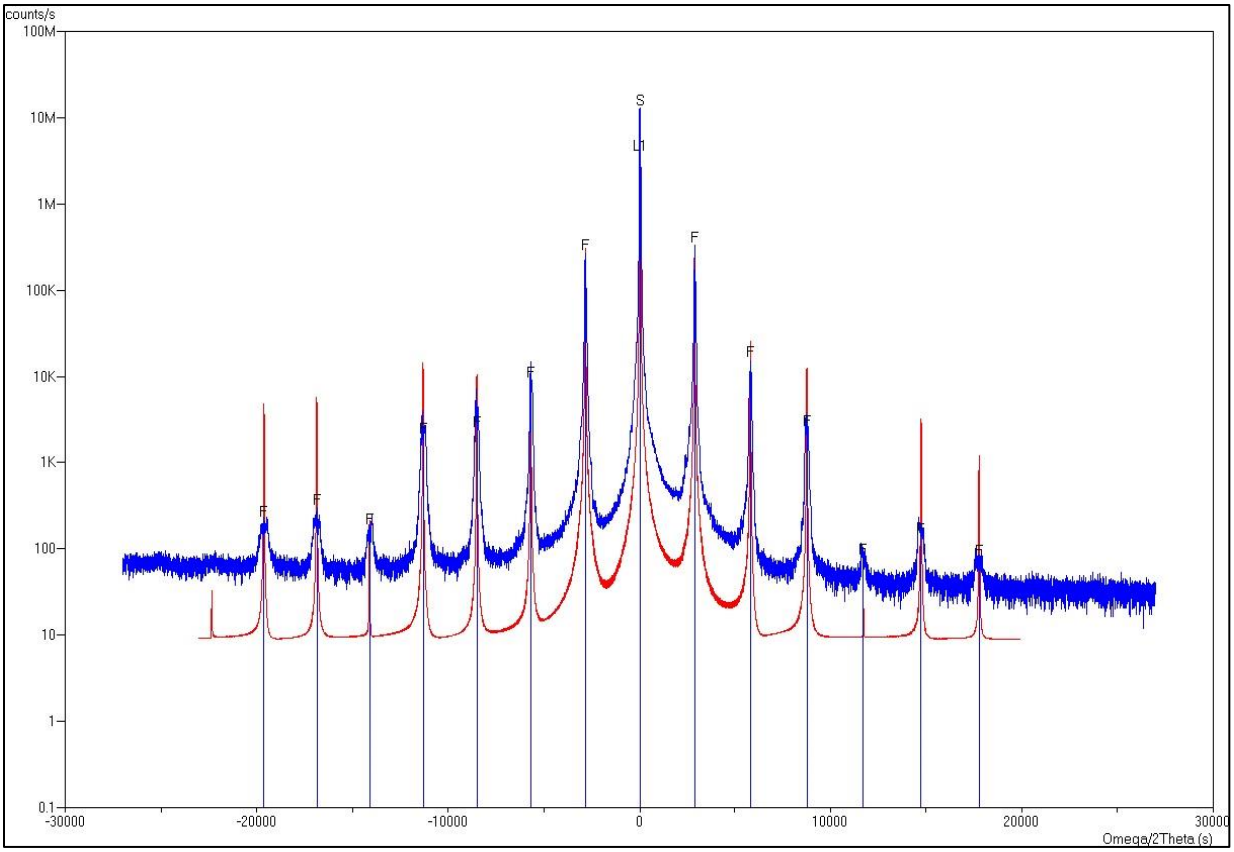

Figure 55 HRXRD (004) ω/2-θ rocking curve data and model for sample SL1

Table 10

Simulation data from HRXRD (004) for sample SL1

Layer	**Composition**	**Thickness (nm)**	**Strain**
$Ga_xIn_{1-x}Sb$	x = 0.94206	2.06	----
InSb	----	0.15	0.5
$InAs_ySb_{1-y}$	y = 1.00000	4.03	----
InSb	----	0.15	0.0
GaSb buffer	----	300 (fixed)	----
GaSb substrate	----	Superlattice - 6.39	$\Delta a/a = -3.57 \times 10^{-4}$

Sample SL2 was damaged so only an approximately 3x3mm piece was left to analyze. Figure 56 through Figure 58 show the reciprocal space maps for sample SL2. As expected, the overall intensity is lower due to the smaller sample size. However, there is also a vertical streak through the substrate in the normal space plot. It is not clear the source of this feature, but it could be due to damage to the substrate. Otherwise, this data is similar to that of the previous sample except that the satellite peaks are closer to the substrate peak due to the larger superlattice repeat distance.

Figure 59 through Figure 61 show the experimental data and modeling for the GaSb (004) rocking curves from sample SL2. The rocking curve has broadening to the right of the substrate and SL +1 superlattice peaks and to the left of the SL -1 superlattice peak suggesting partial relaxation. These features could not be reproduced by the simple model that was used. As with the previous sample, the layer is pseudomorphically strained to lattice matched the substrate and the modeled superlattice repeat length closely matched the sum of the nominal GaSb and InAs sublayer thicknesses and again suggest that the InSb interface layers are incorporated into the surrounding layers. The model also indicates that In incorporation into the top GaSb layer increased to 10.7% compared to 5.8% for the previous sample.

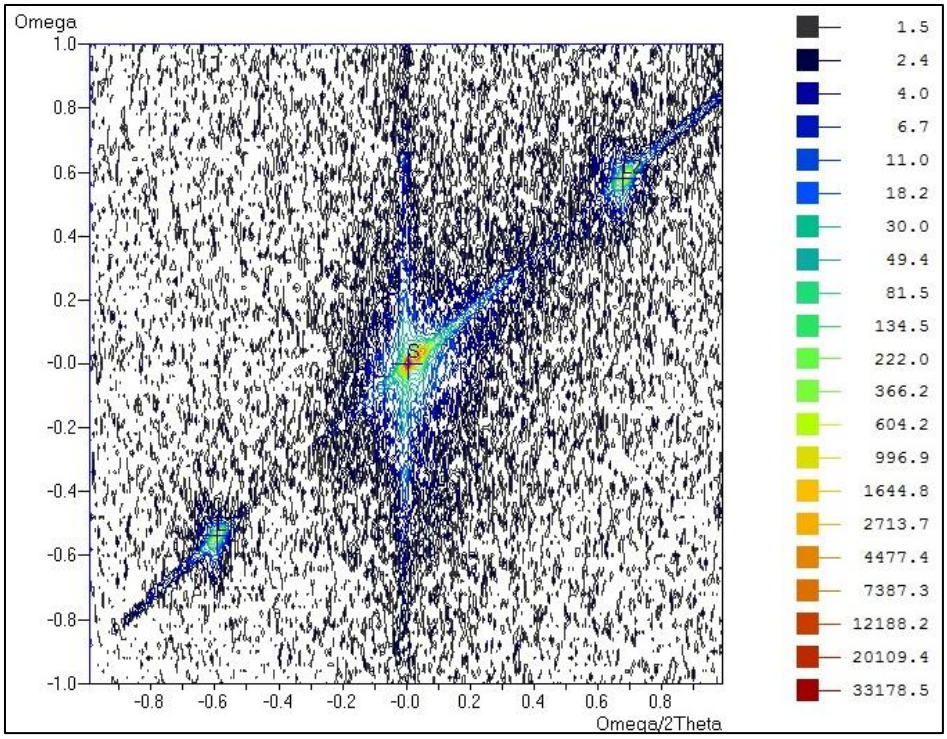

Figure 56 RSM (224) reflection for sample SL2

Table 11

SL2 parameters from RSM (224) reflection

Peak	**Omega**	**2Theta**	**Qx (rlu)**	**Qy (rlu)**	**FWHMx (deg)**	**FWHMy (deg)**	**d-spacing (Å)**
Substrate	3.0028	76.4919	0.35722	0.50558	0.0162	0.0206	1.24435
SL -1	1.8652	75.2964	0.35715	0.49551	0.0160	0.0216	1.26111
SL +1	4.2604	77.8464	0.35733	0.51677	0.0156	0.0220	1.22605

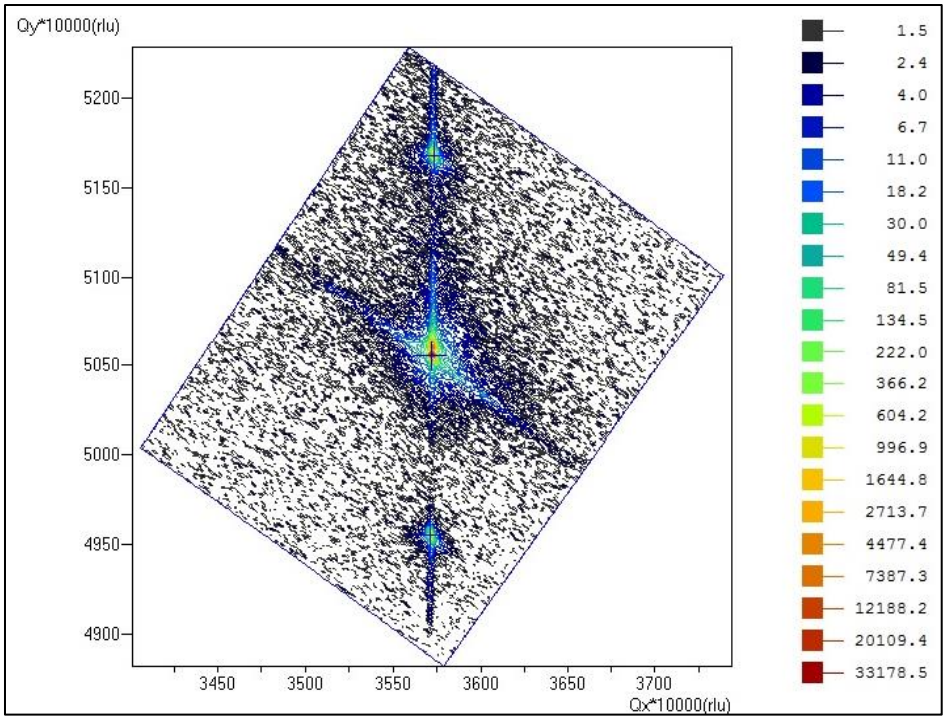

Figure 57 RSM (224) reflection in reciprocal space units for sample SL2

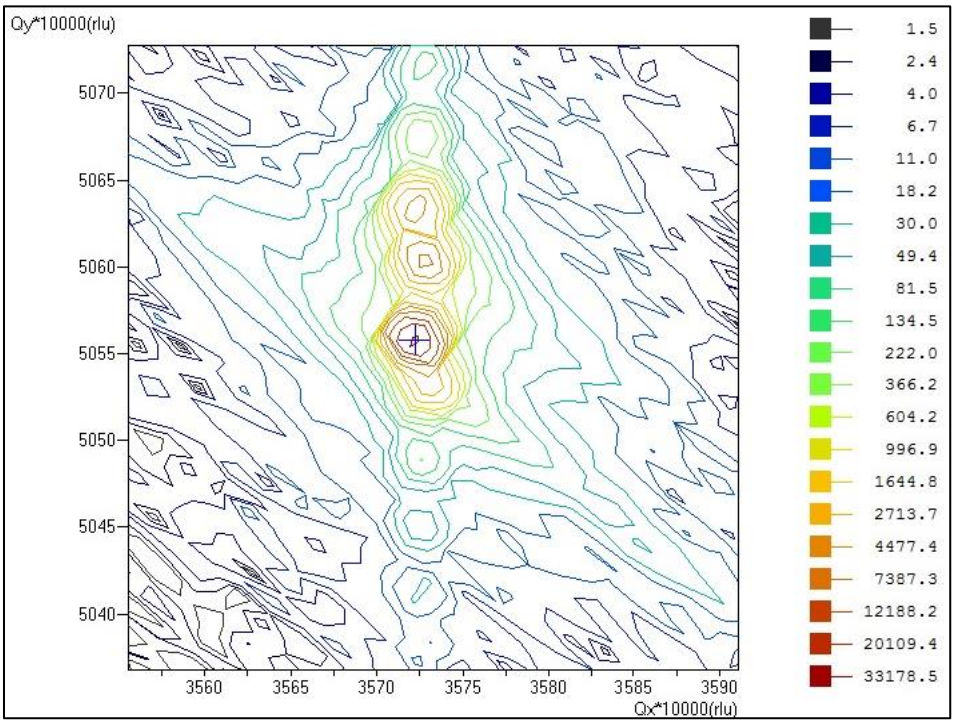

Figure 58 RSM (224) reflection in reciprocal space units for sample SL2– Expanded view near substrate

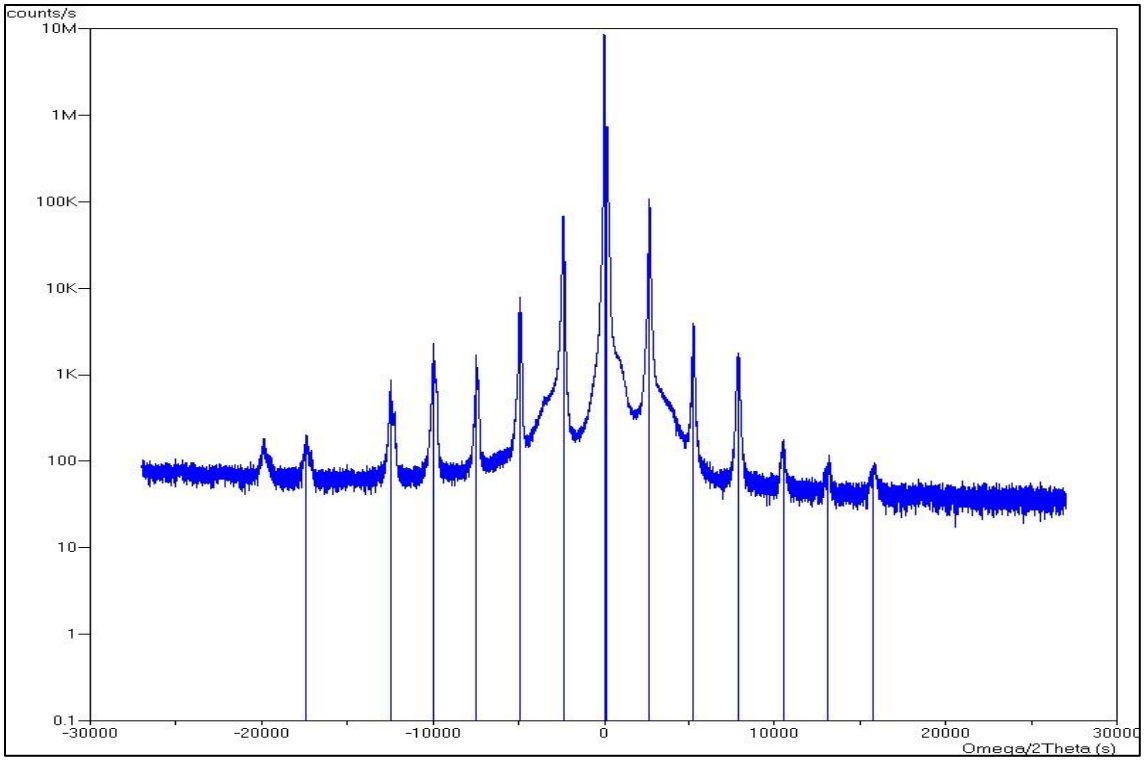

Figure 59 HRXRD (004) ω/2-θ rocking curve for sample SL2

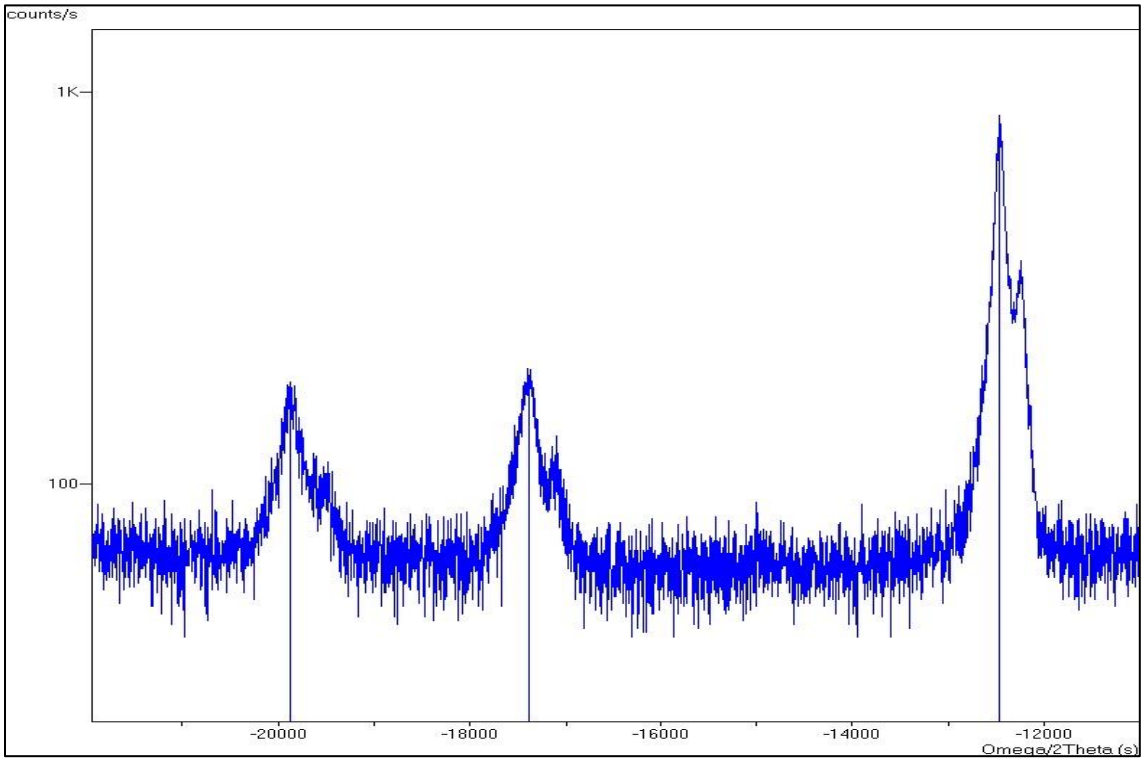

Figure 60 HRXRD (004) ω/2-θ rocking curve for sample SL2 – Expanded view

Table 12

Parameters from HRXRD (004) scan for sample SL2

Peak	**Omega (deg)**	**2Theta (deg)**	**Width (deg)**	**Intensity (cps)**
Substrate	33.3378	60.6426	0.0104	8.478e+6
SL 0	33.3828	60.7326	0.0213	7.399e+5
SL +1	34.0933	62.1536	0.0171	1.077e+5
SL +2	34.8060	63.5789	0.0359	3.918e+3
SL +3	35.5333	65.0337	0.0508	1.673e+3
SL +4	36.2592	66.4853	0.0798	1.702e+2
SL +5	37.0068	67.9806	0.0749	8.800E+1
SL +6	37.7485	69.4639	0.1488	9.400e+1
SL -1	32.6747	59.3165	0.0325	6.324e+4
SL -2	31.9664	57.8998	0.0395	7.845e+3
SL -3	31.2620	56.4909	0.0239	1.689e+3
SL -4	30.5693	55.1057	0.0288	2.333e+3
SL -5	29.8767	53.7204	0.0356	8.361e+2
SL -7	28.5084	50.9837	0.0769	1.894e+2
SL -8	27.8186	49.6042	0.1995	1.446e+2

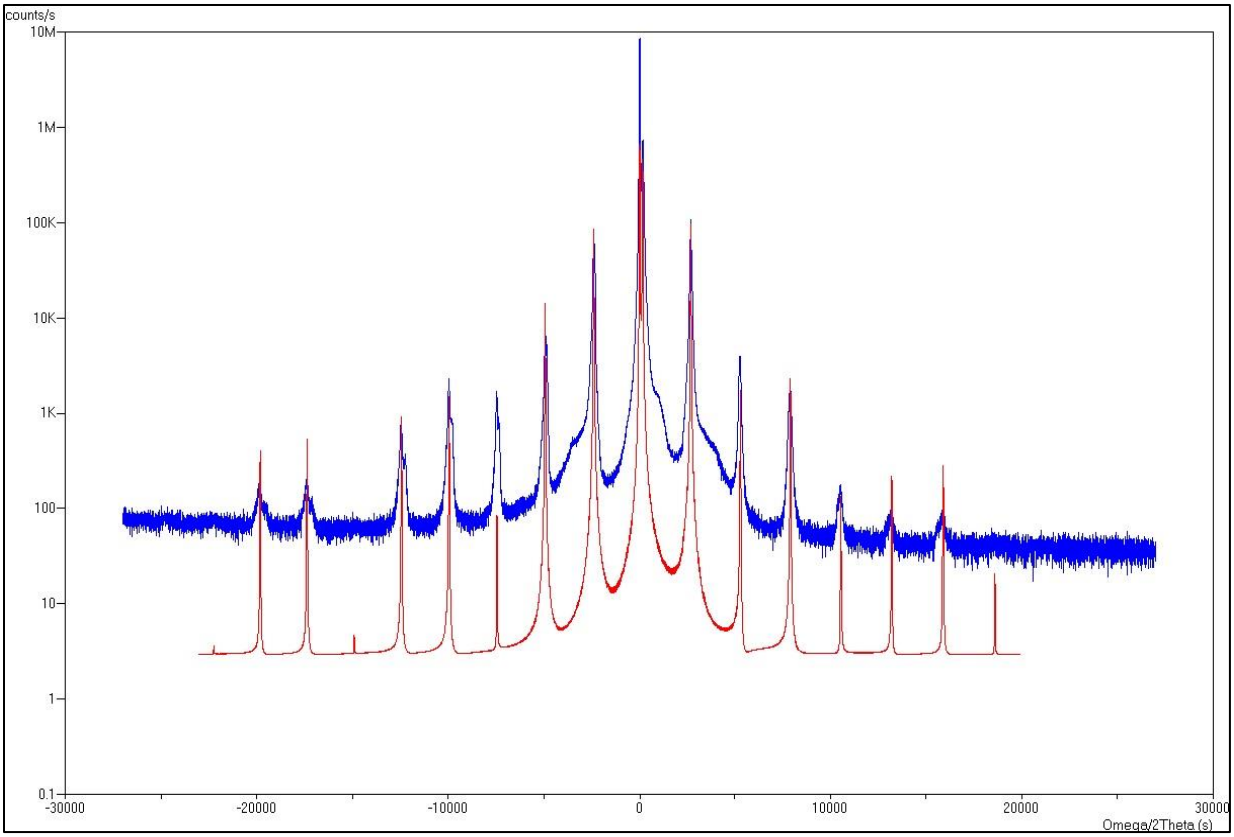

Figure 61 HRXRD (004) ω/2-θ rocking curve data and model for sample SL2

Table 13

Simulation data from HRXRD (004) for sample SL2

Layer	**Composition**	**Thickness (nm)**	**Strain**
$Ga_xIn_{1-x}Sb$	x = 0.89299	2.19	----
InSb	----	0.10	0.0
$InAs_ySb_{1-y}$	y = 1.00000	4.80	----
InSb	----	0.10	0.0
GaSb buffer	----	300 (fixed)	----
GaSb substrate	----	Superlattice – 7.19	$\Delta a/a = -1.03 \times 10^{-3}$

The reciprocal space data for sample SL3 is shown in Figure 62 through Figure 64. This data is very similar to sample SL1 and indicates that the superlattice remains lattice matched to the substrate.

The GaSb (004) rocking curve data for this sample is shown in Figure 65 through Figure 67. The best fitting model for these data indicates that the InAs layer is thicker than expected while the $Ga_xIn_{1-x}Sb$ layer is slightly thinner and more Ga-rich than nominal.

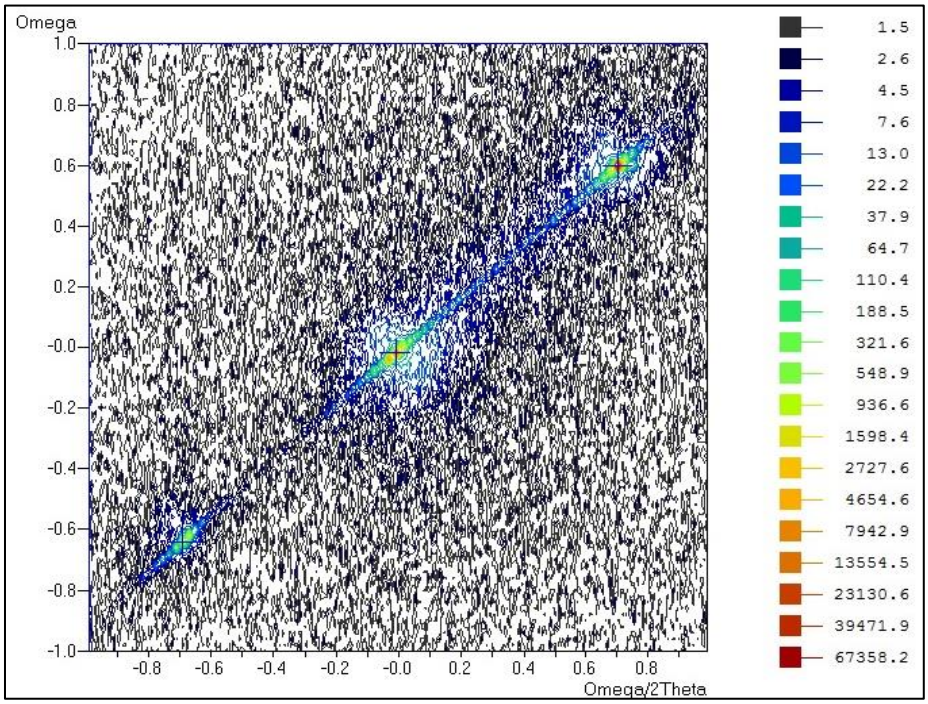

Figure 62 RSM (224) reflection for sample SL3

Table 14

SL3 parameters from RSM (224) reflection

Peak	Omega	2Theta	Qx (rlu)	Qy (rlu)	FWHMx (deg)	FWHMy (deg)	d-spacing (Å)
Substrate	2.9737	76.5186	0.35770	0.50546	0.0118	0.0202	1.24398
SL -1	1.6737	75.1586	0.35765	0.49398	0.0132	0.0208	1.26308
SL +1	4.3087	77.9486	0.35775	0.51732	0.0135	0.0200	1.22470

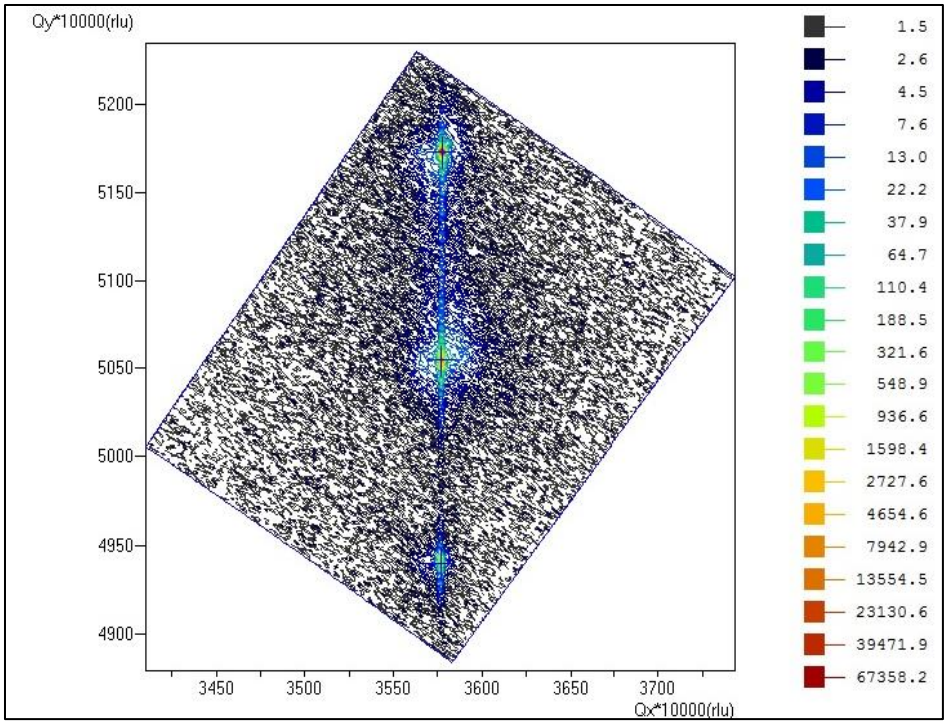

Figure 63 RSM (224) reflection in reciprocal space units for sample SL3

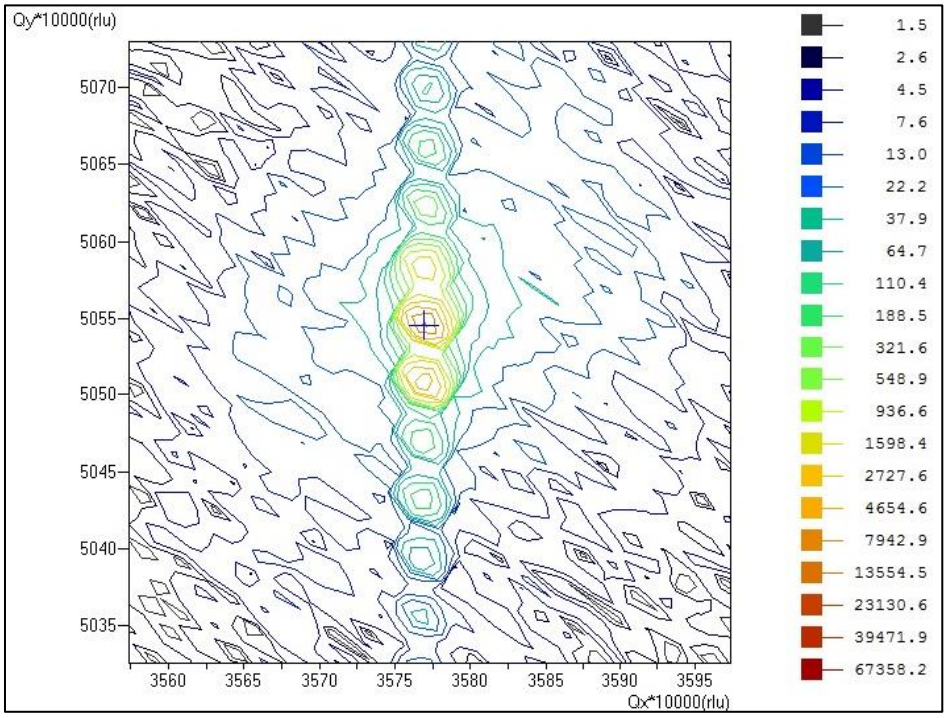

Figure 64 RSM (224) reflection in reciprocal space units for sample SL3– Expanded view near substrate

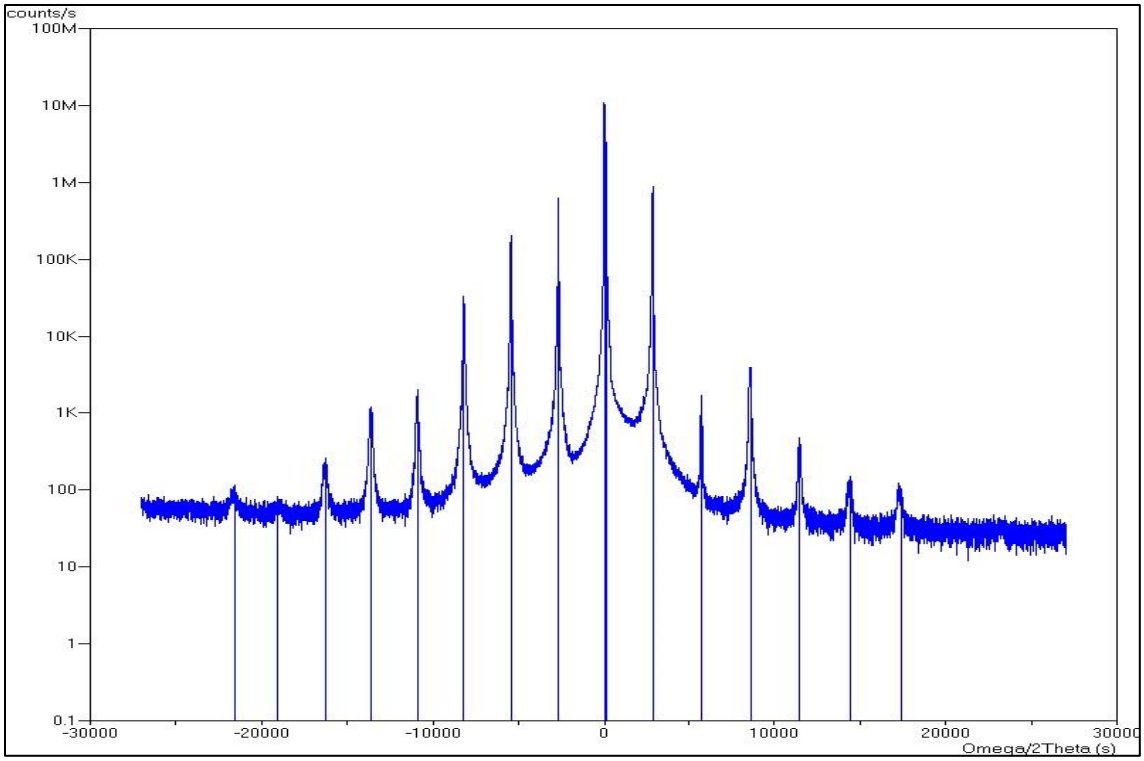

Figure 65 HRXRD (004) ω/2-θ rocking curve for sample SL3

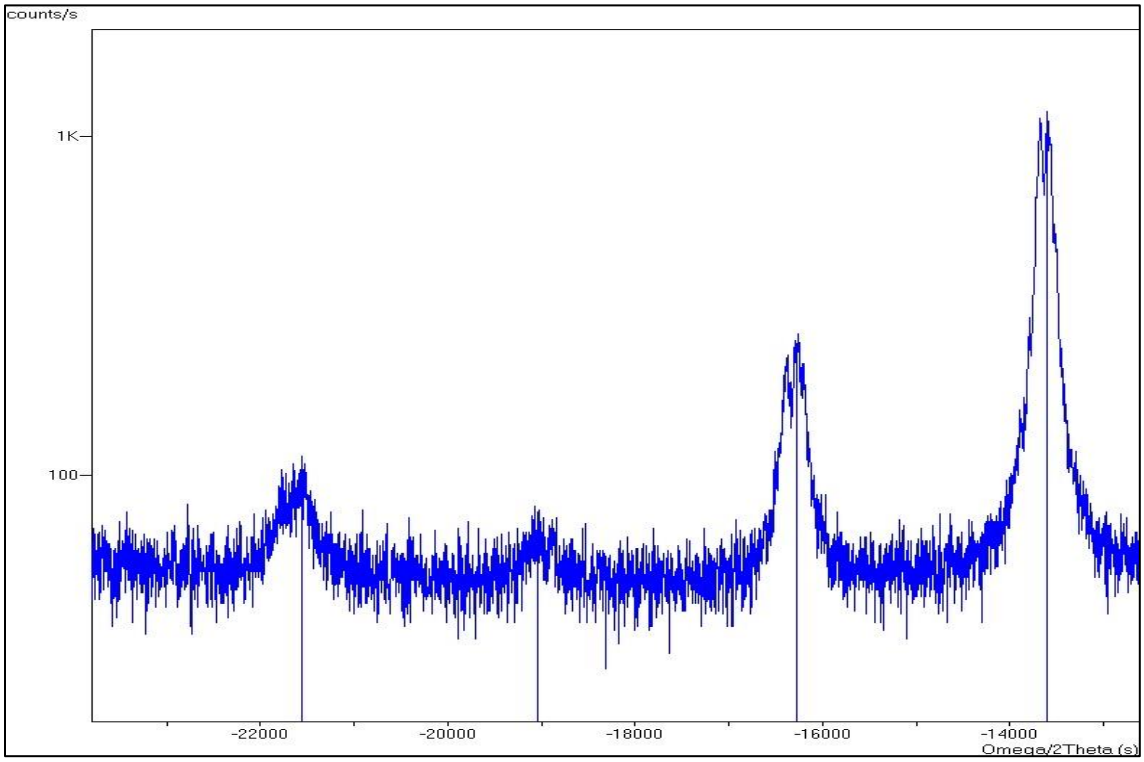

Figure 66 HRXRD (004) ω/2-θ rocking curve for sample SL3 – Expanded view

Table 15

Parameters from HRXRD (004) scan for sample SL3

Peak	**Omega (deg)**	**2Theta (deg)**	**Width (deg)**	**Intensity (cps)**
Substrate	30.2799	60.7561	0.0083	1.062e+7
SL 0	30.3111	60.8186	0.0108	3.347e+6
SL +1	31.0878	62.3719	0.0118	8.821e+5
SL +2	31.8797	63.9557	0.0229	1.632e+3
SL +3	32.6741	65.5446	0.0406	3.893e+3
SL +4	33.4612	67.1187	0.0499	4.264e+2
SL +5	34.2976	68.7915	0.0796	1.367E+2
SL +6	35.1119	70.4201	0.1391	8.860e+1
SL -1	29.5331	59.2625	0.0096	6.204e+5
SL -2	28.7655	57.7273	0.0117	2.074e+5
SL -3	28.0006	56.1975	0.0216	3.295e+4
SL -4	27.2555	54.7074	0.0380	1.967e+3
SL -5	26.5021	53.2004	0.0511	1.150e+3
SL -6	25.7603	51.7169	0.0905	2.192e+2
SL -7	24.9890	50.1743	0.0688	7.550e+1
SL -8	24.2926	48.7815	0.1869	9.570e+1

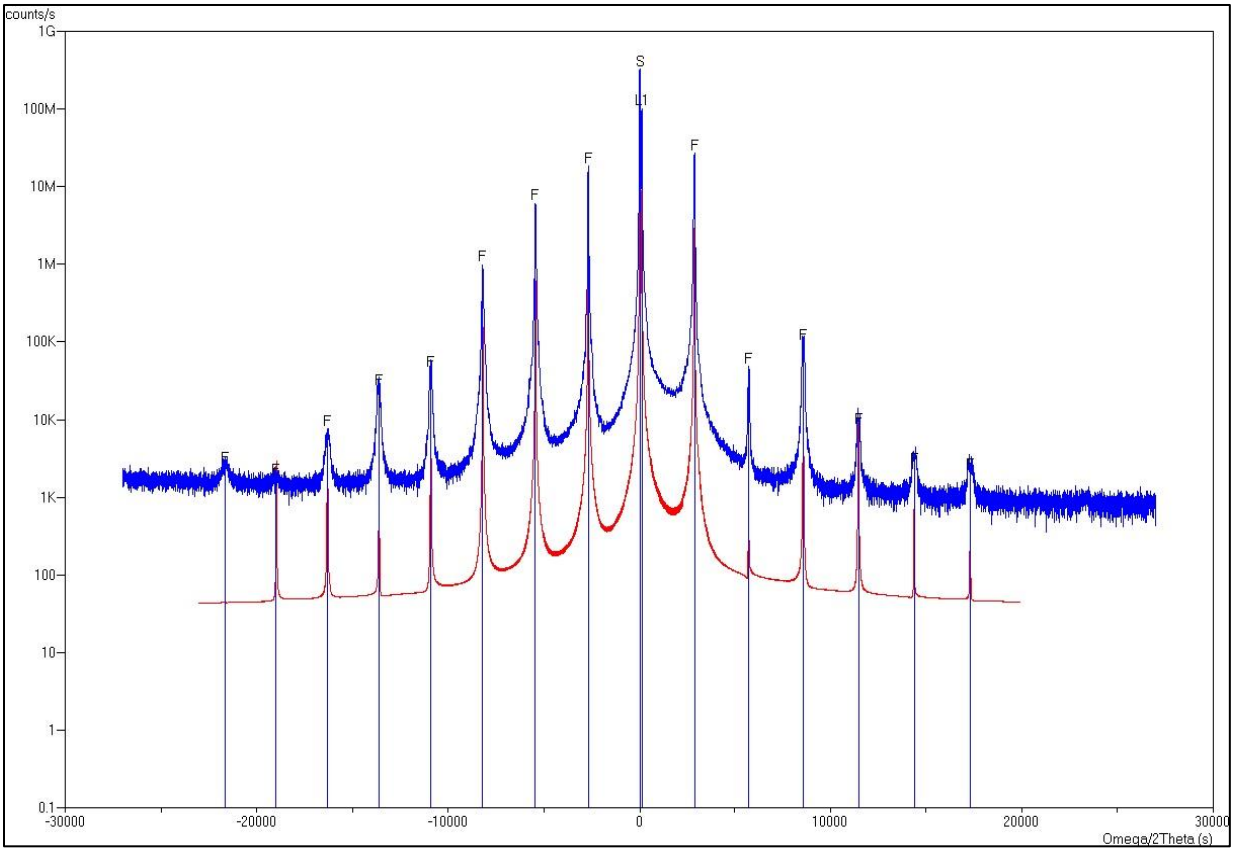

Figure 67 HRXRD (004) ω/2-θ rocking curve data and model for sample SL3

Table 16

Simulation data from HRXRD (004) for sample SL3

Layer	**Composition**	**Thickness (nm)**	**Strain**
$Ga_xIn_{1-x}Sb$	x = 0.75783	1.96	----
$InAs_ySb_{1-y}$	y = 0.99409	4.63	----
GaSb buffer	----	300 (fixed)	----
GaSb substrate	----	Superlattice – 6.59	$\Delta a/a = -9.49 \times 10^{-4}$

Figure 68 through Figure 70 show the GaSb (224) RSM reflections for sample SL4. These data are also quite similar to samples SL1 and SL3. However, the interference fringes to

either side of the substrate peak (Figure 70) could not be clearly resolved as in the previous samples. It is not known whether this is due to a sample misorientation or due to the sample itself.

Figure 71and Figure 73 show the GaSb (004) rocking curve data for this sample. The expanded view (Figure 72) shows that the superlattice peaks are split into 4-5 strong peaks. Since this splitting is an indication of repeat thickness change as a function of depth, it is possible that this is the cause of the blurring of the interference fringes in the RSM. As in the previous sample, the superlattice repeat thickness was larger than nominal; mostly due to the InAs layer.

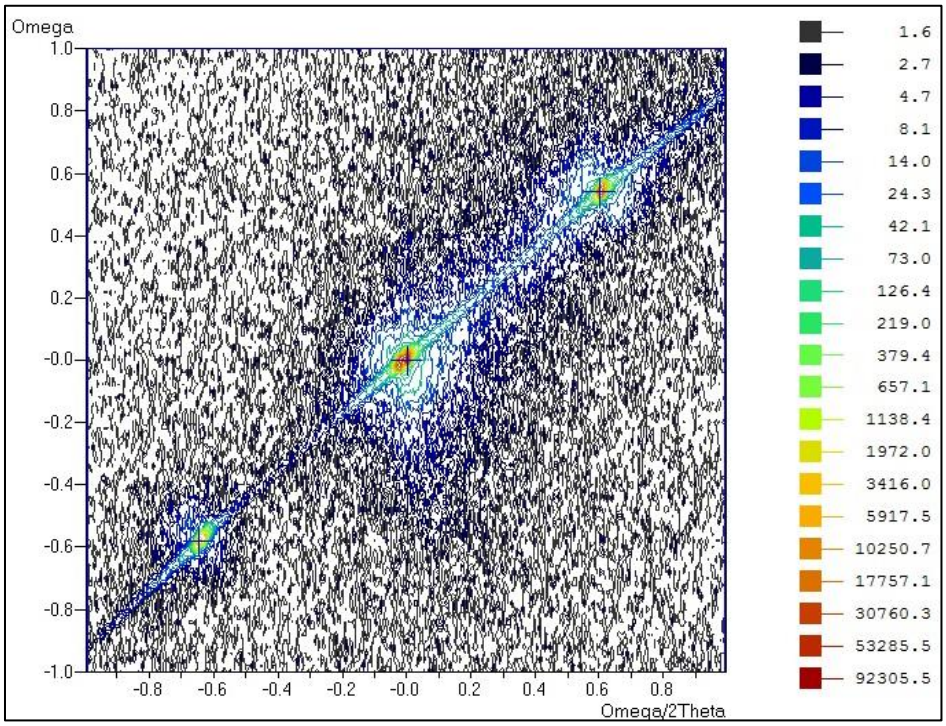

Figure 68 RSM (224) reflection for sample SL4

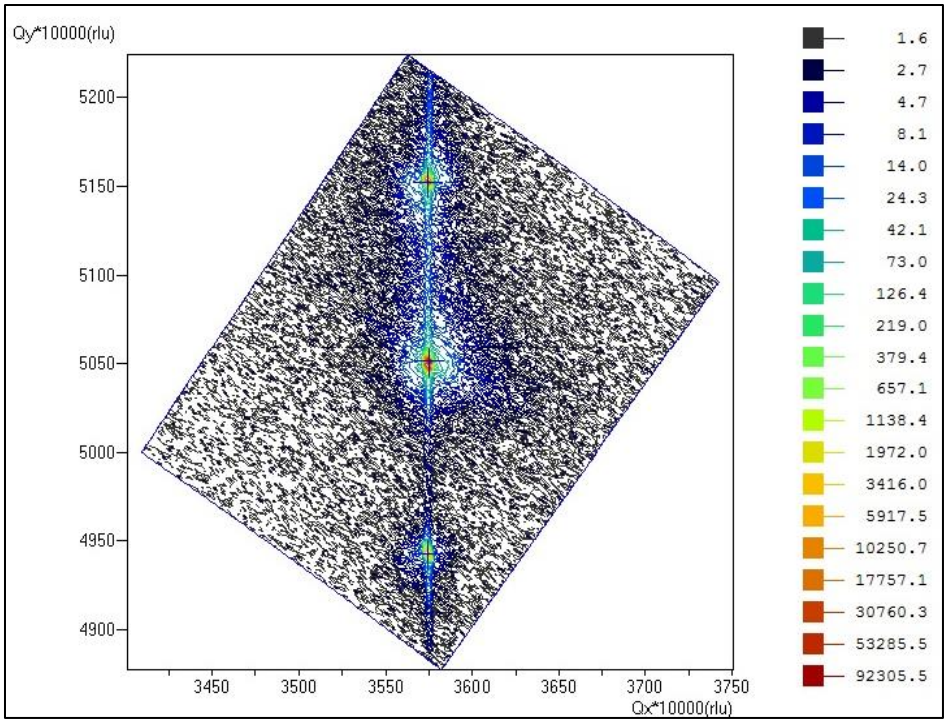

Figure 69 RSM (224) reflection in reciprocal space units for sample SL4

Table 17

SL4 parameters from RSM (224) reflection

Peak	Omega	2Theta	Qx (rlu)	Qy (rlu)	FWHMx (deg)	FWHMy (deg)	d-spacing (Å)
Substrate	2.9396	76.4619	0.35752	0.50511	0.0099	0.0232	1.24476
SL -1	1.7146	75.1719	0.35741	0.49426	0.0150	0.0235	1.26289
SL +1	4.0846	77.6719	0.35745	0.51524	0.0125	0.0218	1.22837

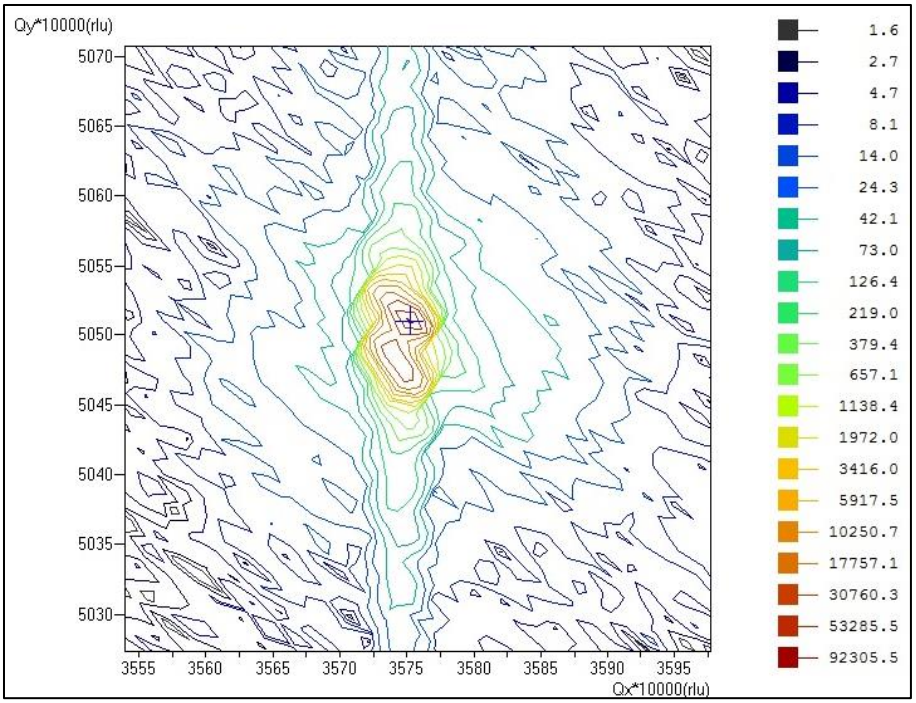

Figure 70 RSM (224) reflection in reciprocal space units for sample SL4– Expanded view near substrate

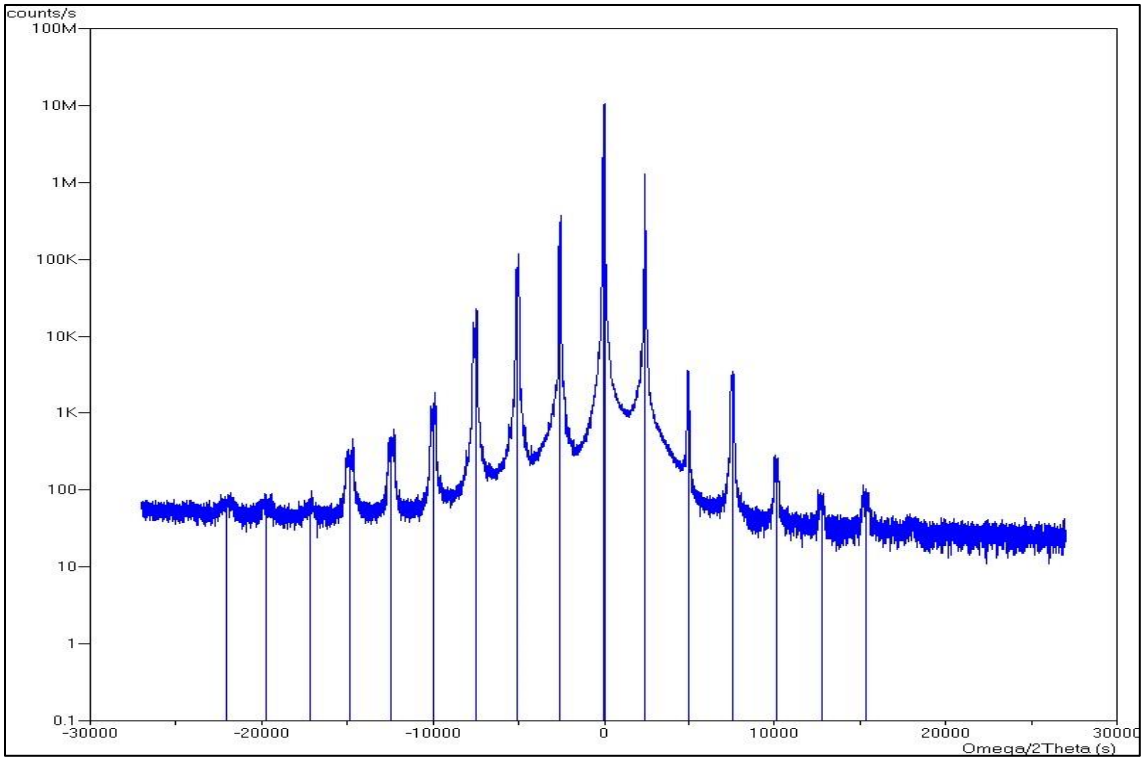

Figure 71 HRXRD (004) ω/2-θ rocking curve for sample SL4

Table 18

Parameters from HRXRD (004) scan for sample SL4

Peak	**Omega (deg)**	**2Theta (deg)**	**Width (deg)**	**Intensity (cps)**
Substrate	30.3119	60.7495	0.0085	1.0822e+7
SL 0	30.2892	60.7041	0.0123	2.151e+6
SL +1	30.9887	62.1031	0.0108	1.267e+6
SL +2	31.6913	63.5082	0.0394	2.384e+3
SL +3	32.4080	64.9415	0.0621	2.143e+3
SL +4	33.1225	66.3706	0.0881	1.982e+2
SL +5	33.8510	67.8275	0.0762	8.370E+1
SL +6	34.5783	69.2821	0.1404	7.650e+1
SL -1	29.5941	59.3138	0.0418	1.276e+5
SL -2	28.9071	57.9398	0.0580	4.541e+4
SL -3	28.2208	56.5672	0.0506	1.097e+4
SL -4	27.5381	55.2019	0.1067	5.823e+2
SL -5	26.8653	53.8563	0.1252	3.464e+2
SL -6	26.1864	52.4984	0.1690	1.844e+2
SL -7	25.5367	51.1991	0.2505	6.680e+1
SL -8	24.8355	49.7967	0.4329	6.570e+1
SL -9	24.1945	48.5147	0.4385	7.250e+1

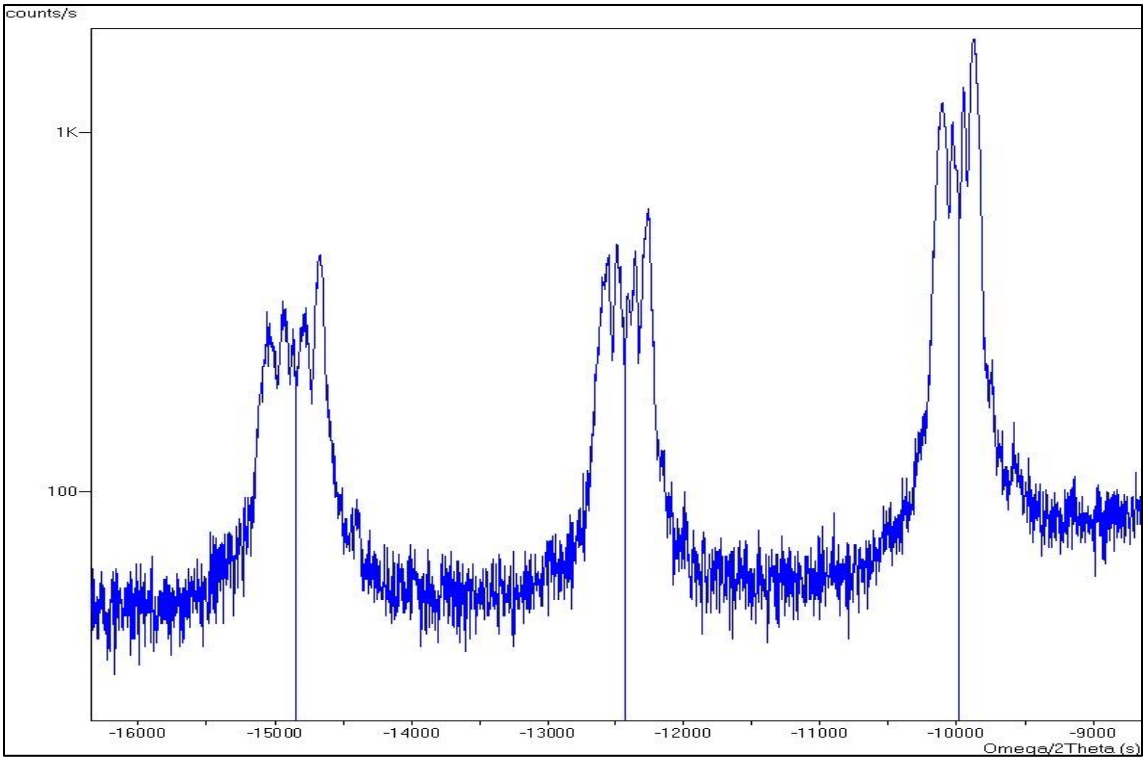

Figure 72 HRXRD (004) ω/2-θ rocking curve for sample SL4 – Expanded view

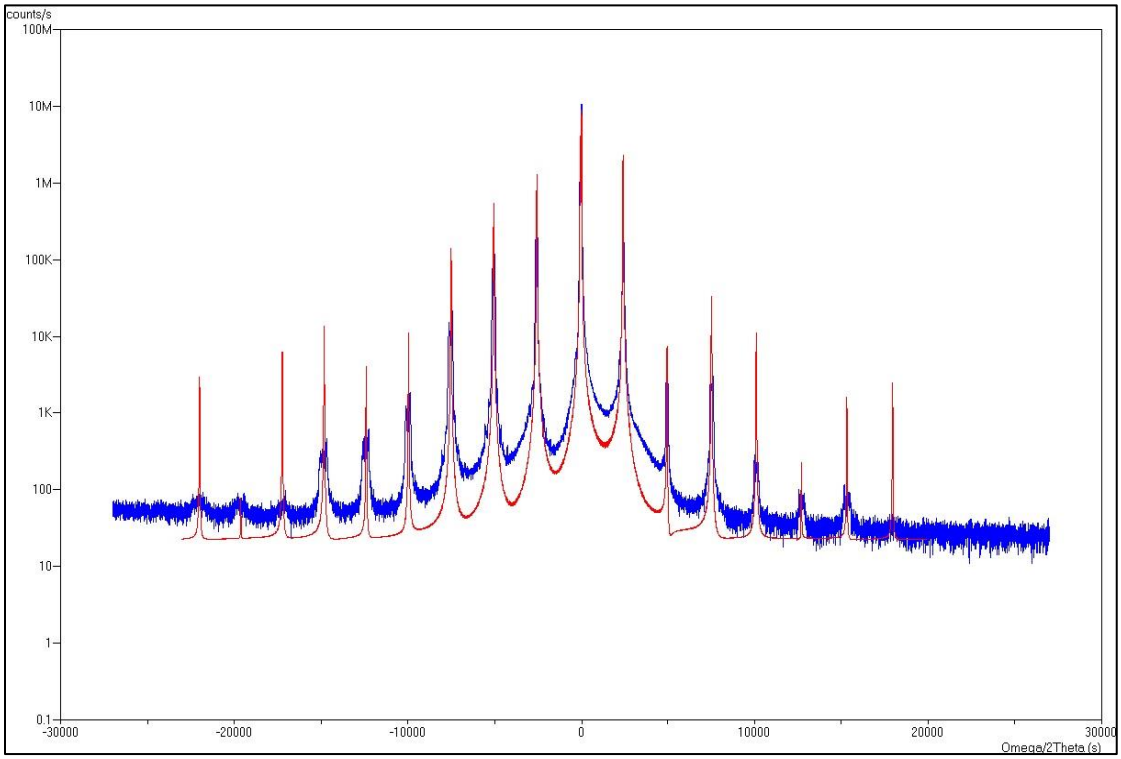

Figure 73 HRXRD (004) ω/2-θ rocking curve data and model for sample SL4

Table 19

Simulation data from HRXRD (004) for sample SL4

Layer	**Composition**	**Thickness (nm)**	**Strain**
$Ga_xIn_{1-x}Sb$	x = 0.76684	1.76	----
InSb	----	0.10	0.0
$InAs_ySb_{1-y}$	y = 1.00000	5.38	----
InSb	----	0.10	0.0
GaSb buffer	----	300 (fixed)	----
GaSb substrate	----	Superlattice – 7.34	$\Delta a/a = 6.26 \times 10^{-4}$

Figure 74 through Figure 76 show the RSM data for the GaSb (224) peak from sample SL5. This sample also has broadening to the right of the substrate indicative of tensile strain in the layer with possible partial relaxation, but not nearly as much as seen in the previous sample. Weak interference fringes are also observed on both sides of the substrate peak.

Figure 77 through Figure 79 show the GaSb (004) rocking curve data for this sample. The superlattice peaks are much more symmetric than for the previous sample and it was possible to simulate the data reasonably well. The model indicates about 6.3% In in the GaSb sublayer. It also estimates the superlattice repeat distance at 6.41nm, again very close to the sum of the nominal GaSb and InAsN sublayers. As with the previous sample, it was not possible to estimate the N content in the InAs sublayer.

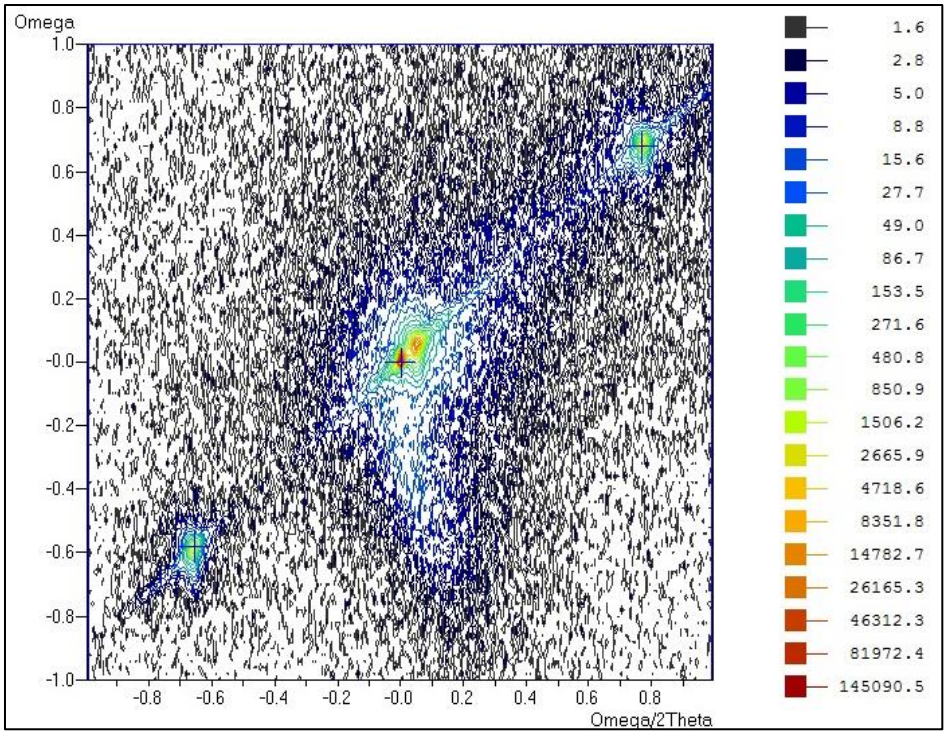

Figure 74 RSM (224) reflection for sample SL5

Table 20

SL5 parameters from RSM (224) reflection

Peak	Omega	2Theta	Qx (rlu)	Qy (rlu)	FWHMx (deg)	FWHMy (deg)	d-spacing (Å)
Substrate	2.9958	76.4580	0.35699	0.50545	0.0100	0.0227	1.24482
SL -1	1.7608	75.1480	0.35681	0.49449	0.0199	0.0365	1.26323
SL +1	4.4458	77.9980	0.35693	0.51830	0.0159	0.0267	1.22404

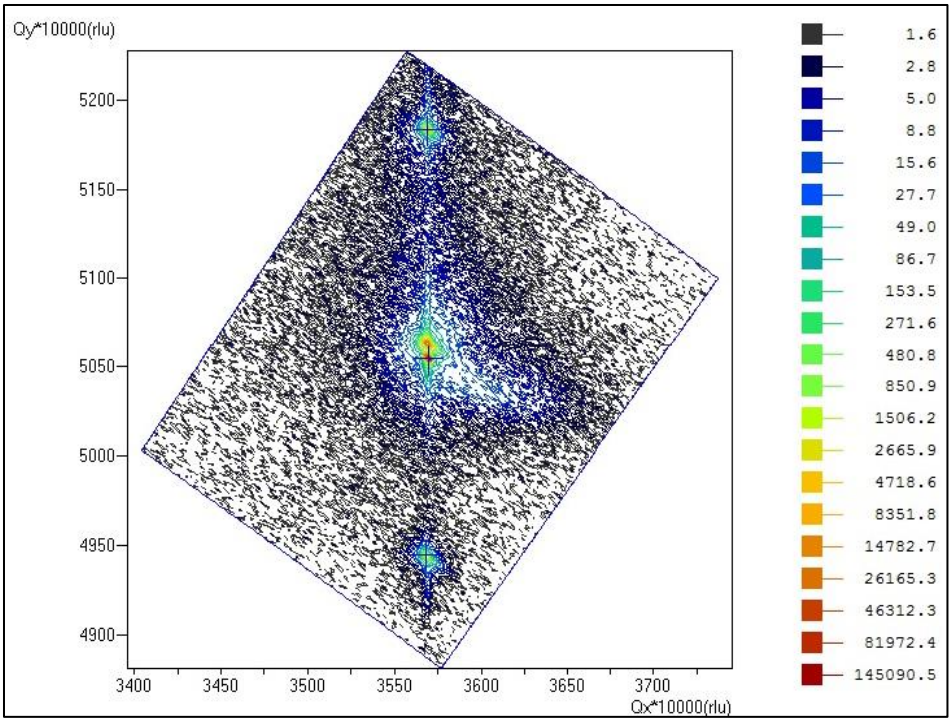

Figure 75 RSM (224) reflection in reciprocal space units for sample SL5

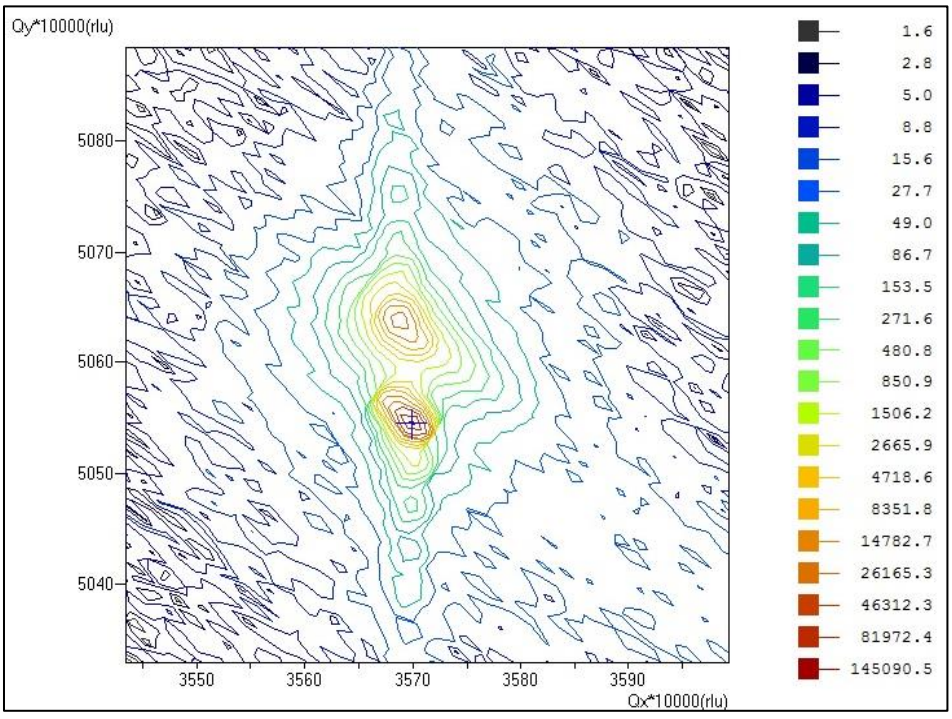

Figure 76 RSM (224) reflection in reciprocal space units for sample SL5– Expanded view near substrate

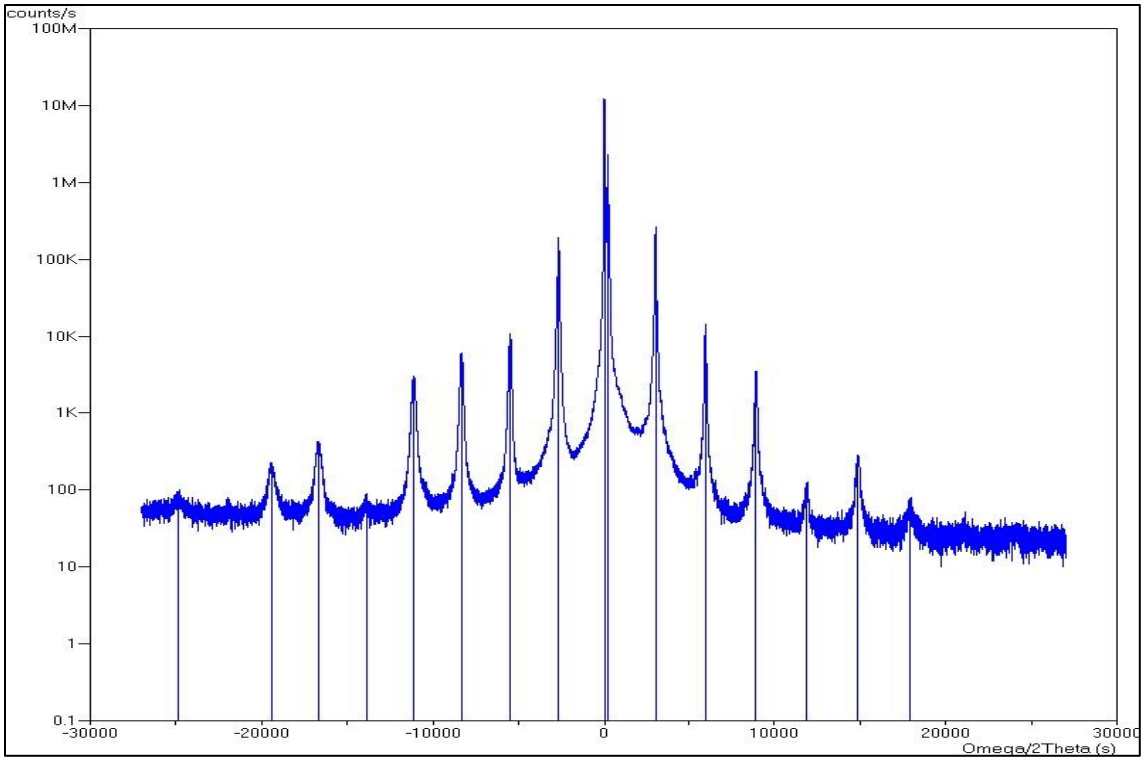

Figure 77 HRXRD (004) ω/2-θ rocking curve for sample SL5

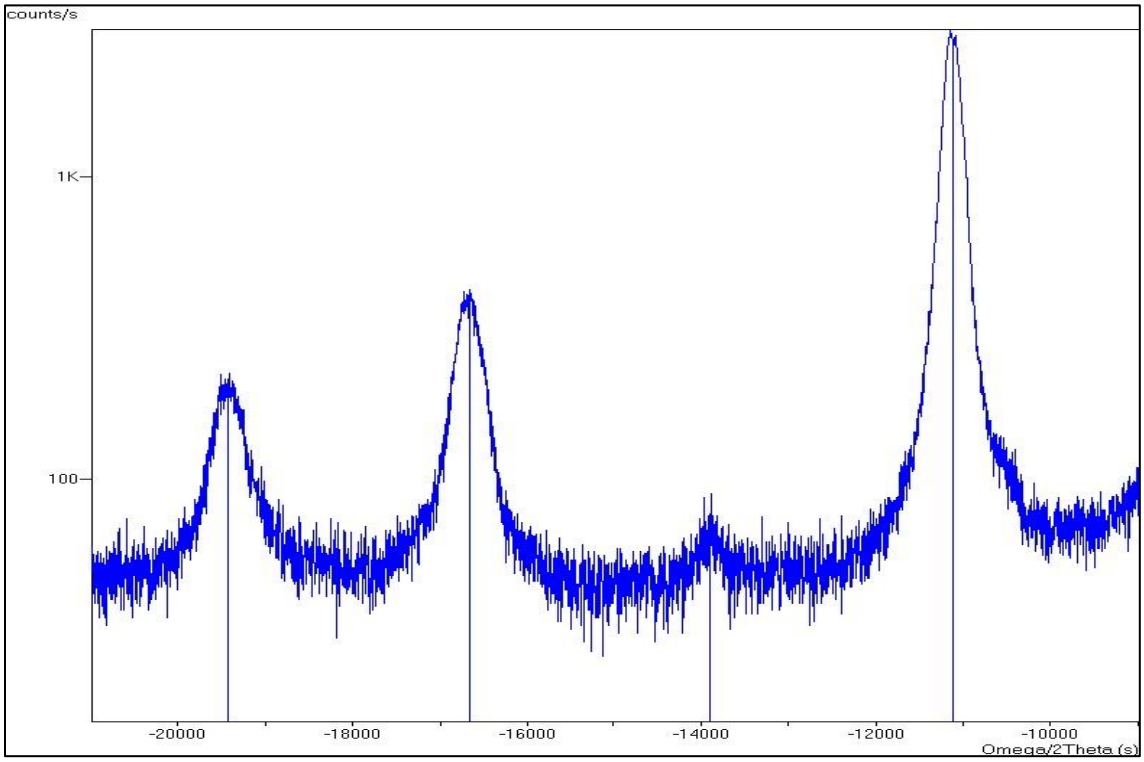

Figure 78 HRXRD (004) ω/2-θ rocking curve for sample SL5 – Expanded view

Table 21

Parameters from HRXRD (004) scan for sample SL5

Peak	**Omega (deg)**	**2Theta (deg)**	**Width (deg)**	**Intensity (cps)**
Substrate	30.3651	60.7454	0.0082	1.209e+7
SL 0	30.4216	60.8583	0.0159	2.306e+6
SL +1	31.2205	62.4561	0.0167	2.644e+5
SL +2	32.0291	64.0734	0.0218	1.450e+4
SL +3	32.8480	65.7112	0.0361	3.566e+3
SL +4	33.6697	67.3547	0.0744	1.100e+2
SL +5	34.5024	69.0199	0.0703	2.730E+2
SL +6	35.3513	70.7177	0.1209	6.470e+1
SL -1	29.6229	59.2610	0.0227	1.935e+5
SL -2	28.8392	57.6936	0.0361	1.056e+4
SL -3	28.0514	56.1180	0.0504	5.440e+3
SL -4	27.2764	54.5679	0.0672	2.818e+3
SL -5	26.5058	53.0268	0.1072	6.200e+1
SL -6	25.7356	51.4864	0.1127	3.883e+2
SL -7	24.9707	49.9566	0.1276	2.053e+2
SL -9	23.4699	46.9550	0.3528	7.980e+1

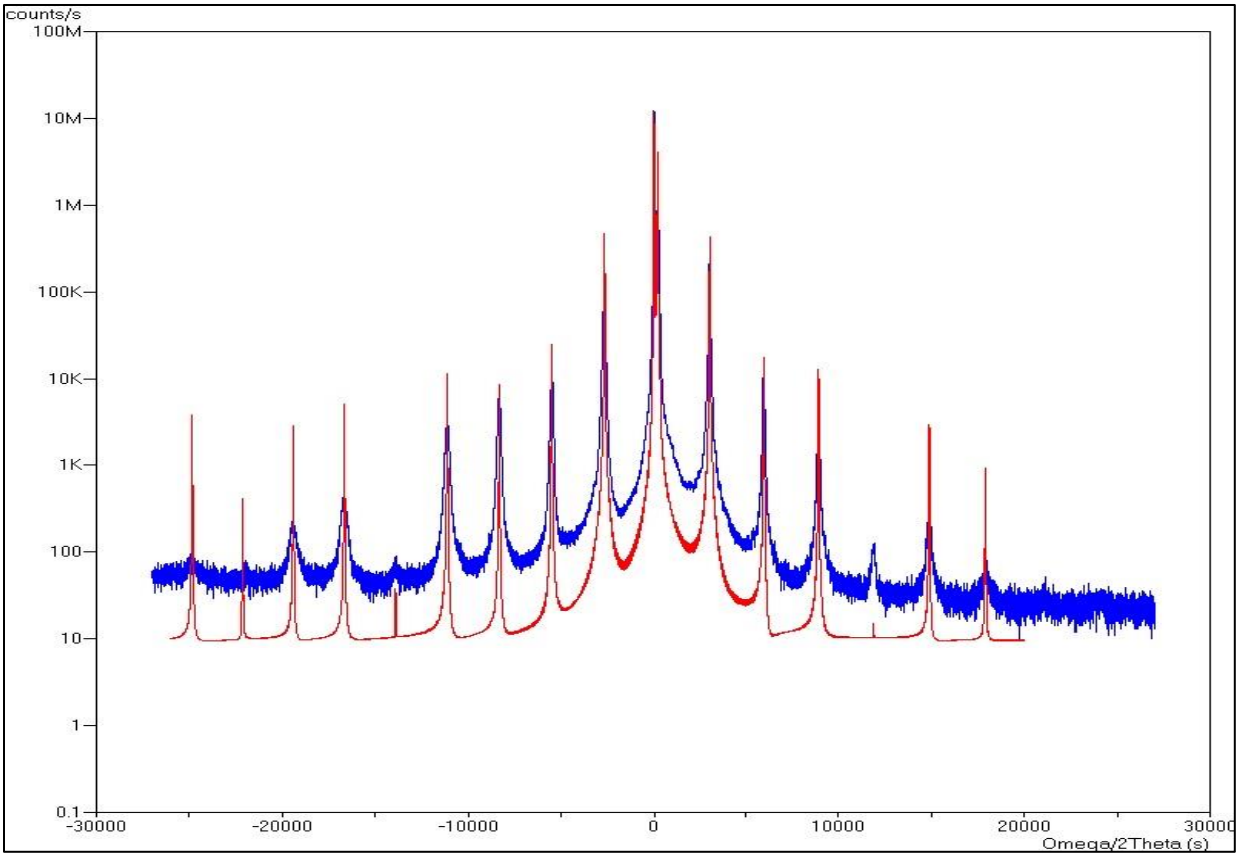

Figure 79 HRXRD (004) ω/2-θ rocking curve data and model for sample SL5

Table 22

Simulation data from HRXRD (004) for sample SL5

Layer	**Composition**	**Thickness (nm)**	**Strain**
$Ga_xIn_{1-x}Sb$	x = 0.93661	2.19	----
InSb	----	0.10	1.3
$InAs_ySb_{1-y}$	y = 1.00000	4.02	----
InSb	----	0.10	2.8
GaSb buffer	----	300 (fixed)	----
GaSb substrate	----	Superlattice – 6.41	$\Delta a/a = -1.64 \times 10^{-3}$

The GaSb (224) RSM for sample SL6 is shown in Figure 80 through Figure 82. These data are unlike any of the previous samples. There is a lot of broadening around both the substrate and superlattice peaks. While some of this broadening occurs to both sides of the strong peaks and may be due to dislocations, there is also more broadening to the right of these peaks in Figure 81. This indicates the layer is tensile strained with partial relaxation. Note also that while the interference fringes are observed above the substrate peak, they are not detected below the substrate peak.

The GaSb (004) rocking curves (Figure 83 through Figure 85) are also unlike any of the previous samples. The superlattice peaks appear to be composed of a sharp peak to the right and a broad peak to the left. There is also no obvious zero order superlattice peak observed for this sample. The composition of the GaSb sublayer was allowed to vary from top to bottom to try to account for the differences, but it is clear in Figure 84 that this attempt was unsuccessful. It appears that this broadening may be due to changes in one or more of the sublayers occurring part of the way through the deposition rather than being due to the same change in all 100 of the repeat depositions. Note also that it was not possible to model the N incorporation in the InAs sublayer. This is because no zinc blende lattice parameters for InN are found in the materials database used by Epitaxy.

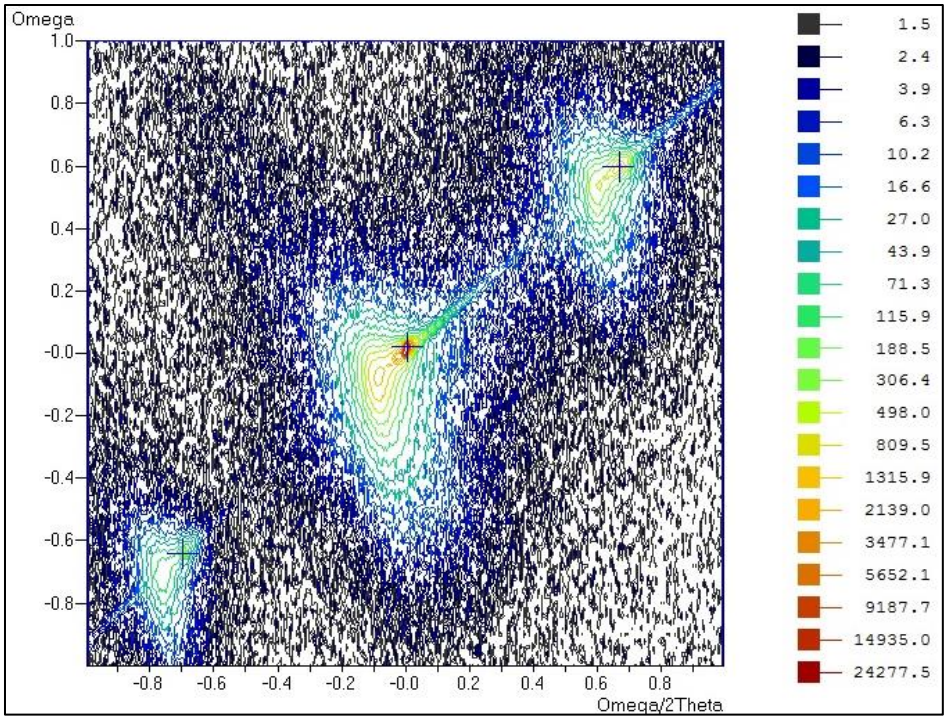

Figure 80 RSM (224) reflection for sample SL6

Table 23

SL6 parameters from RSM (224) reflection

Peak	Omega	2Theta	Qx (rlu)	Qy (rlu)	FWHMx (deg)	FWHMy (deg)	d-spacing (Å)
Substrate	2.9980	76.4852	0.35720	0.50553	0.0169	0.0238	1.24444
SL -1	1.6380	75.0852	0.35735	0.49357	0.0127	0.0225	1.26413
SL +1	4.2430	77.8152	0.35723	0.51658	0.0247	0.0303	1.22646

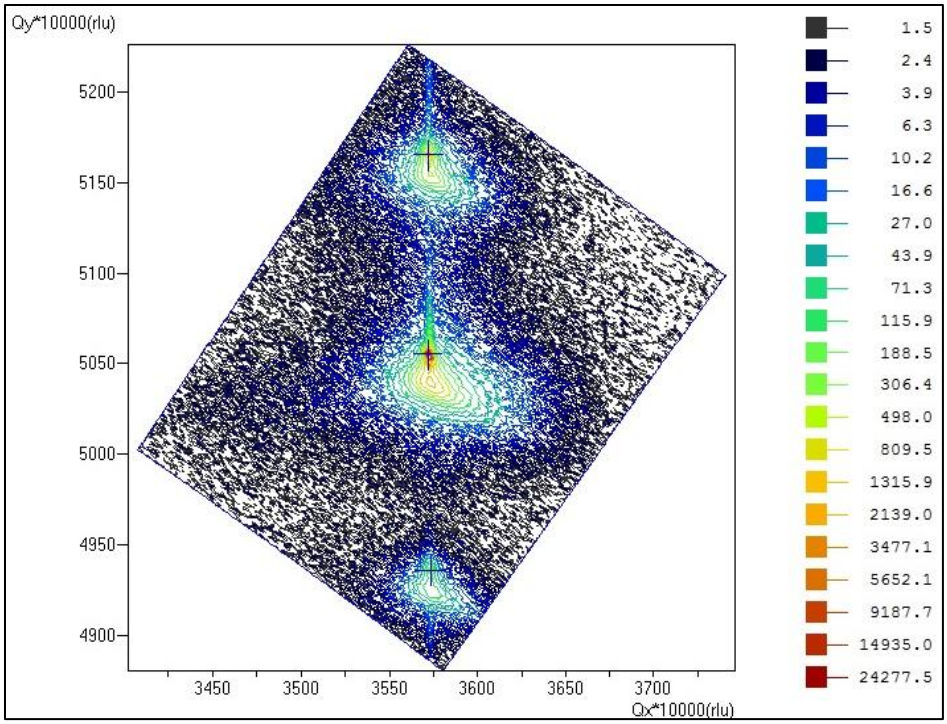

Figure 81 RSM (224) reflection in reciprocal space units for sample SL6

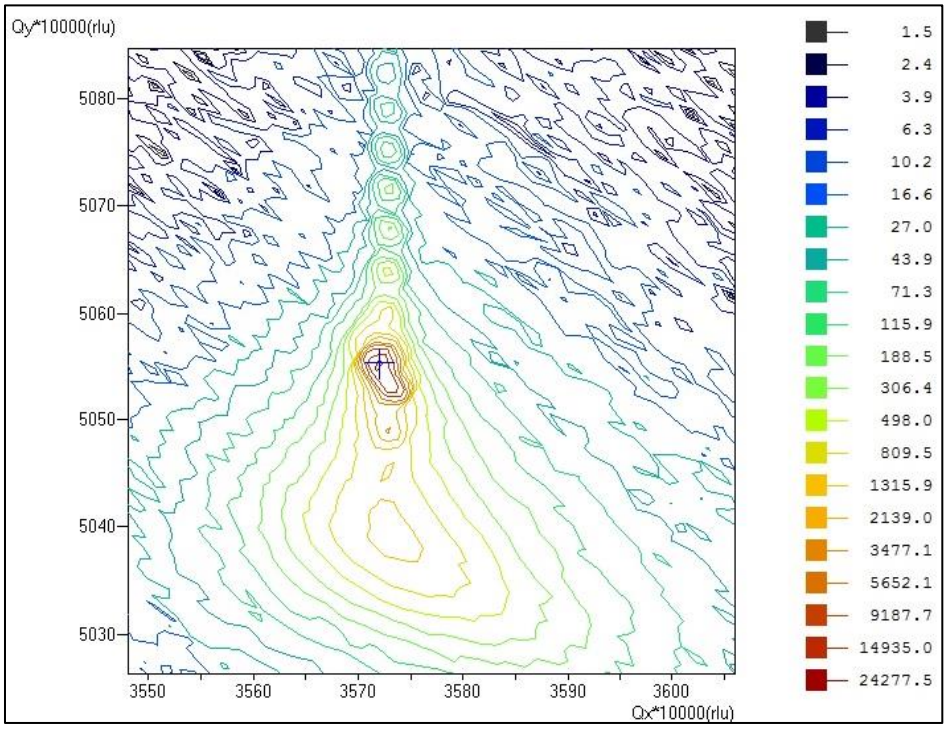

Figure 82 RSM (224) reflection in reciprocal space units for sample SL6– Expanded view near substrate

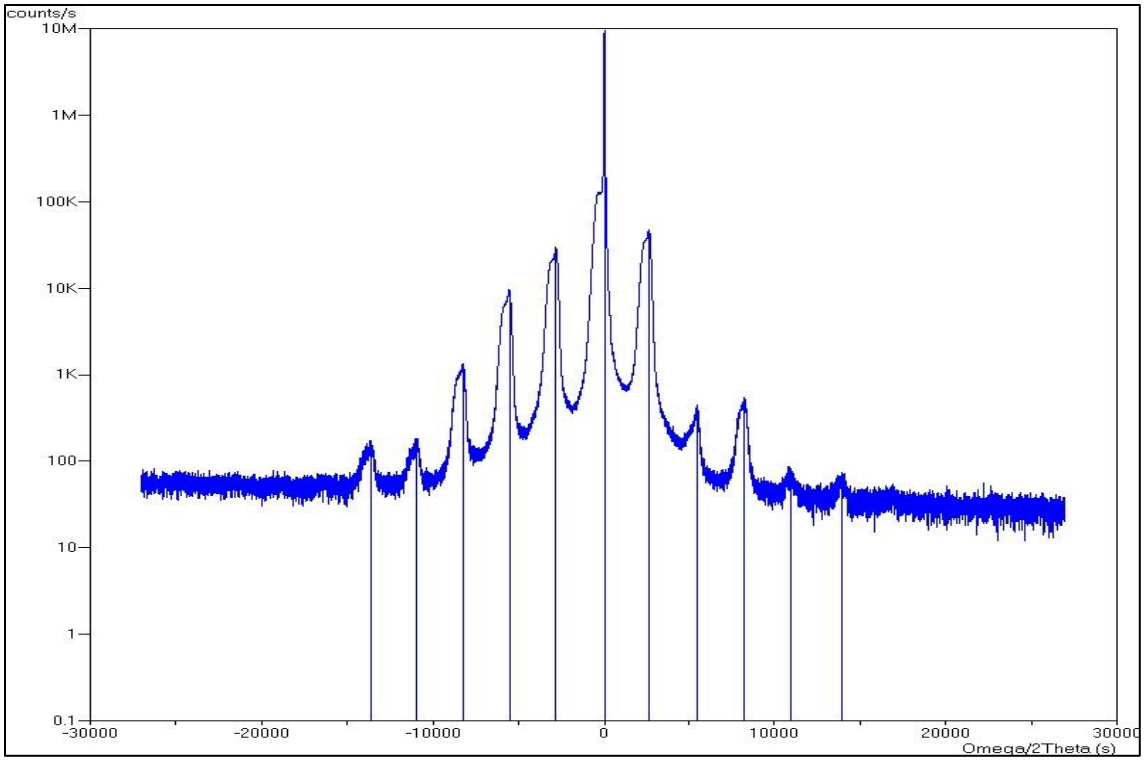

Figure 83 HRXRD (004) ω/2-θ rocking curve for sample SL6

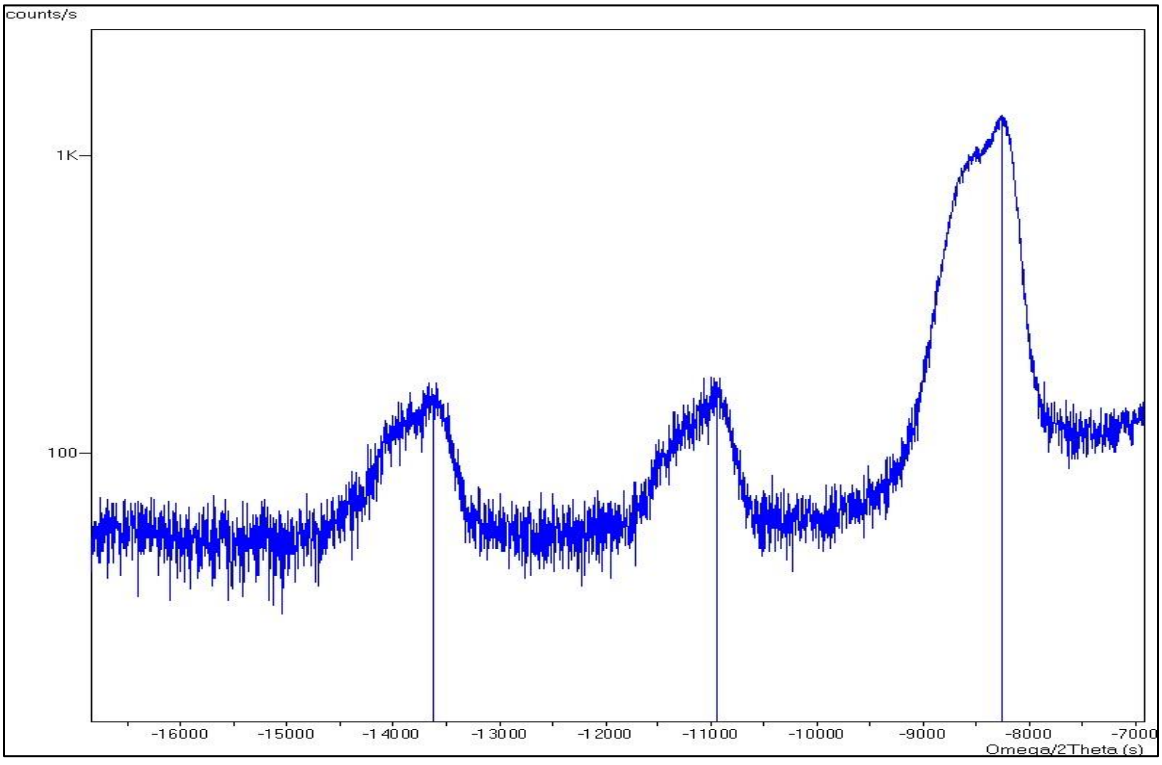

Figure 84 HRXRD (004) ω/2-θ rocking curve for sample SL6 – Expanded view

Table 24

Parameters from HRXRD (004) scan for sample SL6

Peak	**Omega (deg)**	**2Theta (deg)**	**Width (deg)**	**Intensity (cps)**
Substrate	30.3346	60.7716	0.0100	9.268e+6
SL +1	31.0823	62.2670	0.1472	4.794e+4
SL +2	31.8611	63.8246	0.1840	3.967e+2
SL +3	32.6335	65.3695	0.1548	4.860e+2
SL +4	33.3717	66.8457	0.2588	6.230e+1
SL +5	34.2156	68.5336	0.1559	7.030E+1
SL -1	29.5504	59.2032	0.1511	2.971e+4
SL -2	28.7952	57.6928	0.1581	9.445e+3
SL -3	28.0412	56.1847	0.1713	1.335e+3
SL -4	27.2975	54.6974	0.2116	1.524e+2
SL -5	26.5513	53.2050	0.2044	1.511e+2

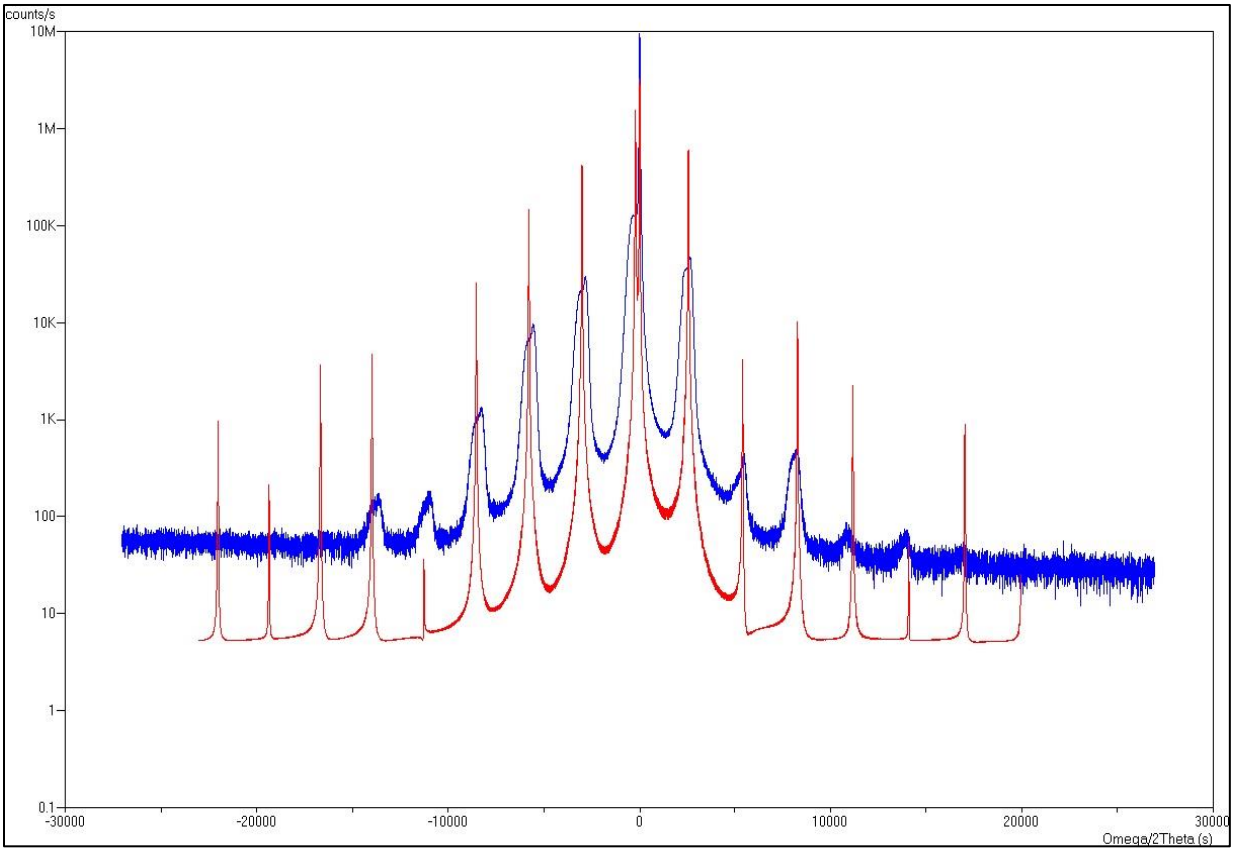

Figure 85 HRXRD (004) ω/2-θ rocking curve data and model for sample SL6

Table 25

Simulation data from HRXRD (004) for sample SL6

Layer	**Composition**	**Thickness (nm)**	**Strain**
$Ga_xIn_{1-x}Sb$	x_{top} = 0.78186 x_{bot} = 0.76413	1.71	----
InSb	----	0.10	0.0
$InAs_ySb_{1-y}$	y = 1.00000	4.65	----
InSb	----	0.10	0.0
GaSb buffer	----	300 (fixed)	----
GaSb substrate	----	Superlattice – 6.56	$\Delta a/a = 7.45 \times 10^{-4}$

5.6 Scanning Transmission Electron Microscope (STEM) Results and Analysis

Samples SL2, SL3, SL4, SL5, and SL6 were analyzed by STEM. In the Z contrast imaging the intensity varies with atomic number Z as Z^{ν} where power index ν can vary between 1.3 and 2 depending on the detector acceptor angle [91]. The spatial resolution is given by the diameter of the electron probe, which in our case was 1.0 Å. Thus, this system provides atomic resolution and allows for imaging of individual atomic columns providing a quantitative measurement of constituent layer thickness, interface thickness, interface roughness and any interdiffusion. However, one has to be careful while quantifying the information on the interfacial roughness due to the intensity dependence of the incoherent scattering on thickness of the sublayers and any spatial thickness inhomogeneity of the sample.

The superlattice contains cation and anion pairs of widely different z –values: Ga (z = 31) vs Sb (z = 51) and In (z = 49) vs As (z = 33) vs N (z = 7) thus providing sufficient contrast between the different atomic elements (as shown in Figure 86). Further the atomic spatial resolution allows resolving of cations and anions within the cation and anion dumbbells. STEM micrographs were all aligned to the [110] zone axis and are shown for all the SL investigated, as shown in Figure 87 to Figure 91. The cation and anions dumbbells are clearly resolved with the In and Sb spots being larger and brighter than the As and Ga spots, respectively. This readily allows distinction of the constituent sublayers because of the right or left hand position of the brighter and larger atoms in GaSb and InAs, respectively along the [001] growth direction. GaInSb layer in the Figure 88 is clearly evident from the two bright spots in the same dumbbell and is the brightest amongst all the sublayers. Similarly, the InAsN dumbbell is brighter than InAs dumbbell. All of the superlattice structures exhibit distinct sublayers with sharp interfaces

and with no extended structural defects consistent with the XRD RSM data shown in section 5.5 above. The thicknesses of the sublayers are in excellent agreement

with those determined from HRXRD data as well as in-stu RHEED oscillations within (+/-) 1 ML .The intentional InSb interfaces are shown but the thickness could not be quantified because the smallest scale feature is ~ 3 ML's and the anticipated layer thickness is ~ 1 ML. The STEM image of the SL3 structure (Figure 88) does not reveal any intentional InSb interface consistent with the anticipated growth.

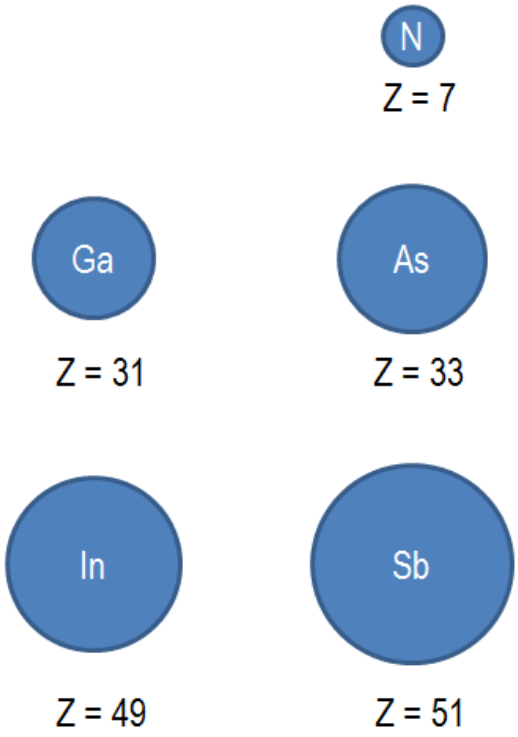

Figure 86 Relative intensities to expect for the atoms involved in this study

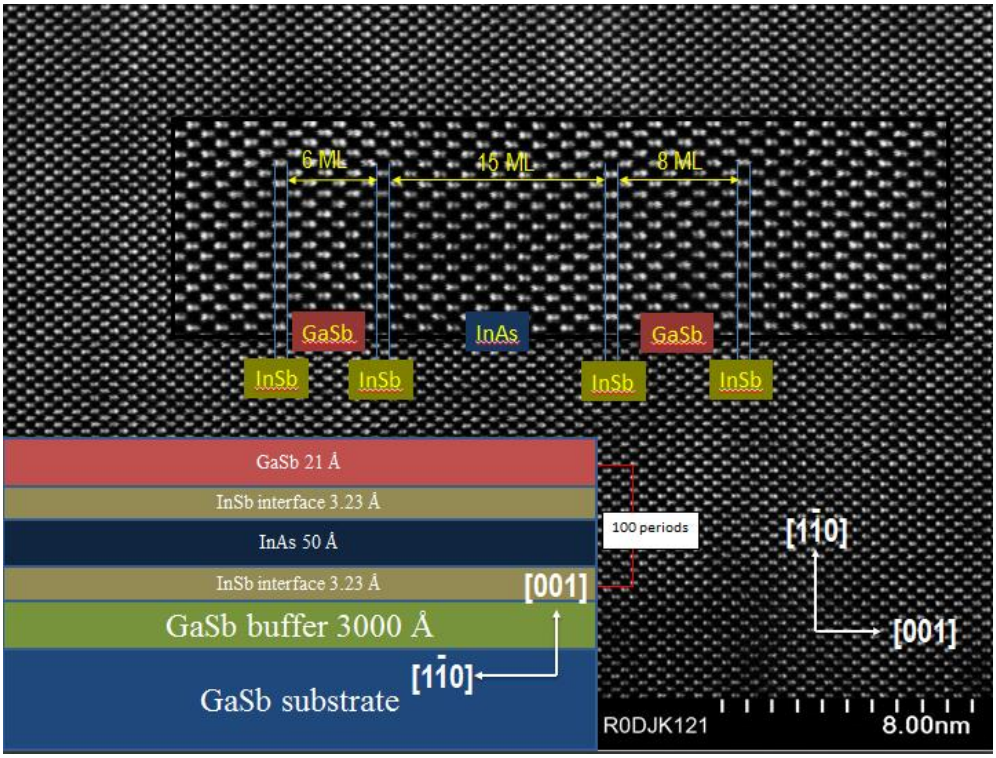

Figure 87 STM image of SL2

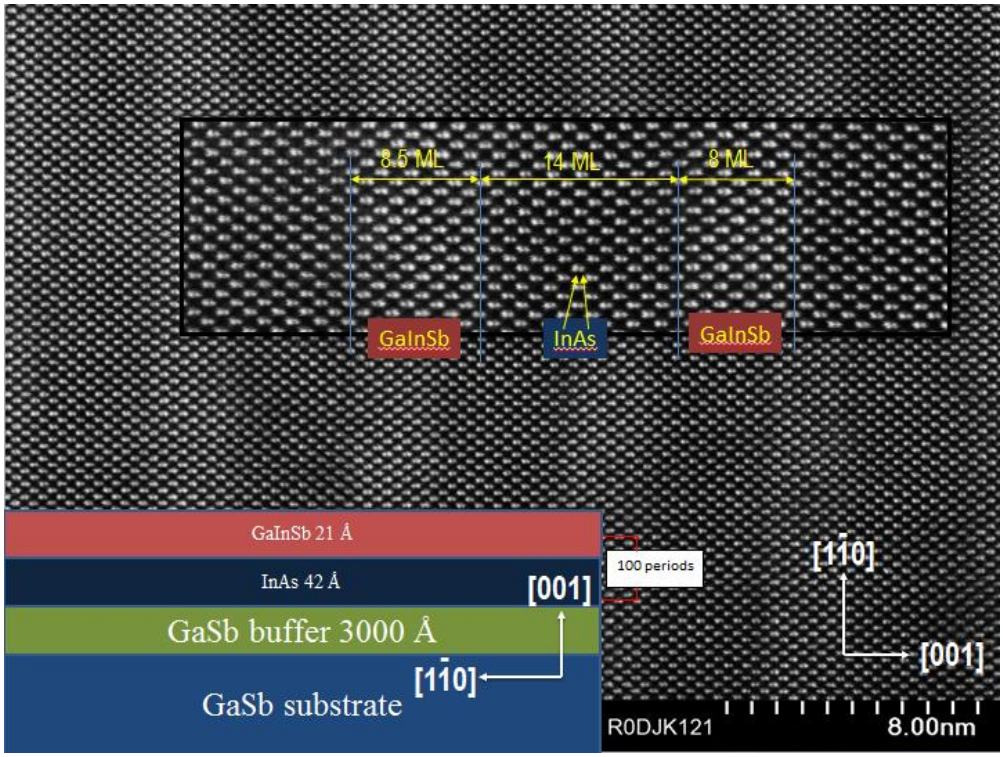

Figure 88 STM image of SL3

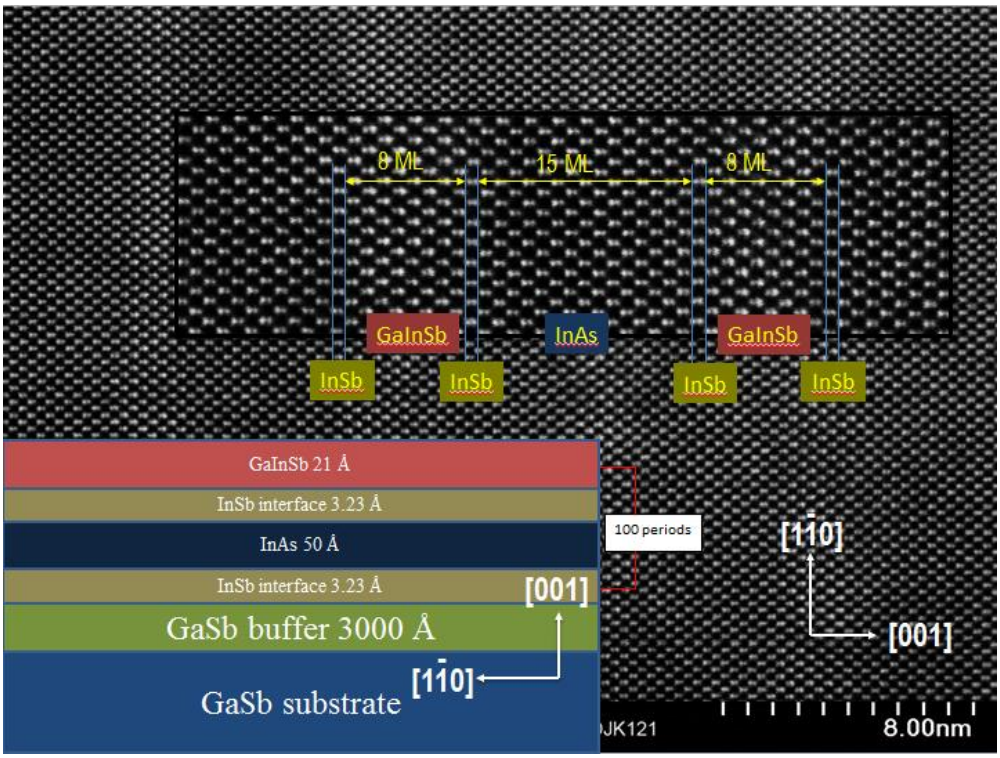

Figure 89 STM image of SL4

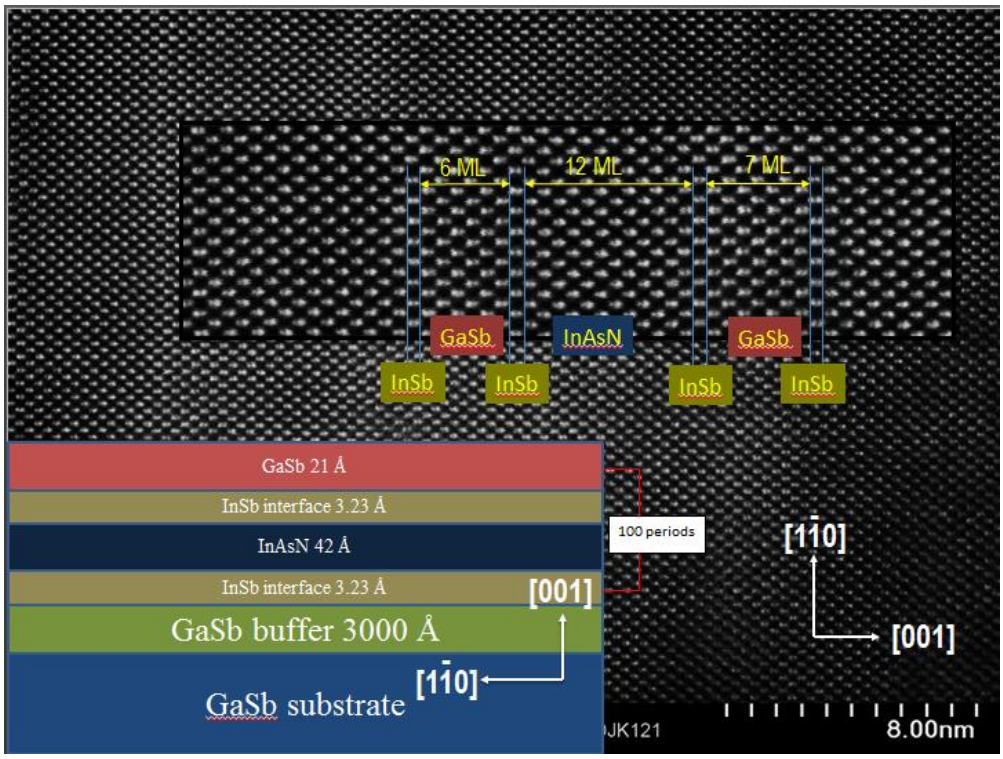

Figure 90 STM image of SL5

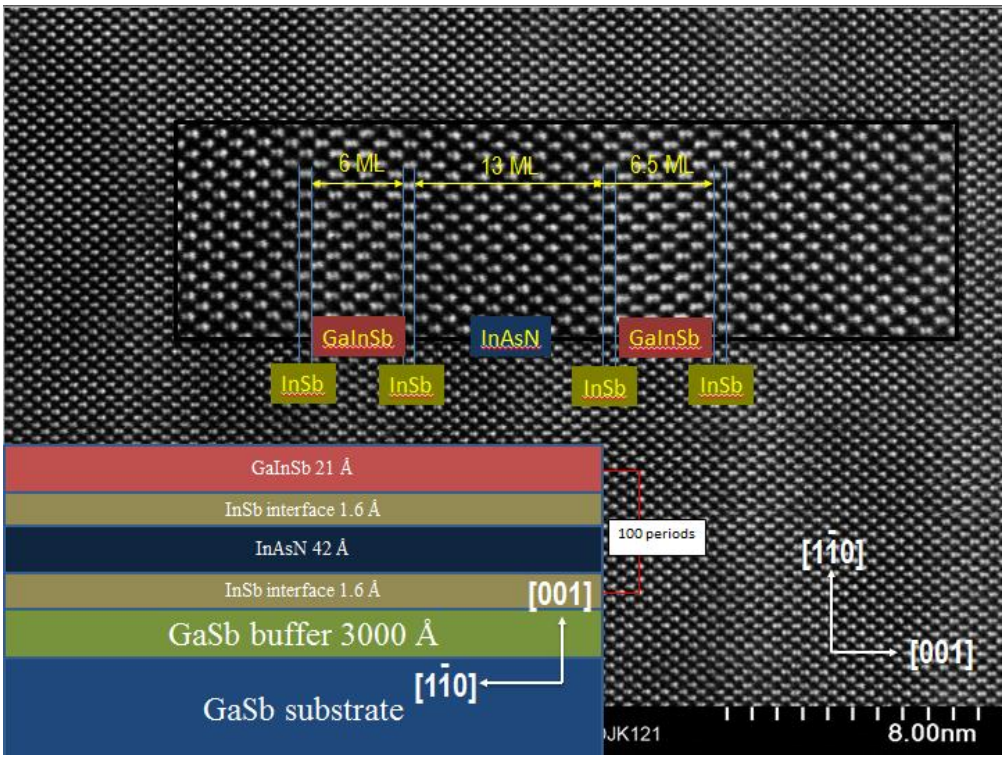

Figure 91 STEM image of SL6

5.7 Raman Spectroscopy Results

The Raman spectra of different samples were acquired with both the HeNe and Ar+ ion lasers. Since the penetration depth of 633 nm wavelength from the HeNe laser is reported to be ~100 nm in InAs and 65 nm in GaSb, the visible laser does not penetrate through the entire superlattice stack (total thickness ~ 630 nm). Similarly, the 514 nm wavelength penetrates 37 nm in InAs and 24 nm in GaSb and also does not penetrate the entire stack. Thus, the spectra acquired were composed of many bands due to the presence of different thin layers in the samples and the assignment of the bands becomes a challenge. The bands were de-convoluted with the assignment of the bands being based on the literature [92] for individual bands (phonons) of pure stress free compounds as shown below in Table 26.

Table 26

Optical phonon modes [93]

LO (Longitudinal optical phonon) and TO (Transversal optical phonon)		
III-V Binary Alloy	LO (cm^{-1})	TO (cm^{-1})
InAs	241.1	220.4
GaSb	232.6	223.6
InSb	190.7	179.7
GaAs	292.2	268.5

5.7.1 Raman analysis. With Ar+ ion laser one cannot resolve the InAs and GaSb peaks for LO modes. Most of the work in the literature has been carried out by Ar+ ion laser [94-97] but was unable to resolve GaSb (LO) and InAs (LO) peaks. However, it was able to resolve second order modes not seen with the HeNe laser. For example, structure SL3 exhibits a GaSb 2(LO) indicative of a high quality layer, but it is only seen with the Ar+ ion laser. On the other hand the HeNe laser is able to resolve the GaSb and InAs LO modes as well as the InSb LO and TO modes. For a (100) substrate only the LO phonons are expected as per the selection rules. However, in our work we do get TO phonon modes as has been found in other SL's reported in literature [92]. The presence of the TO lines does not necessarily suggest low quality as long as other characteristics attest to the high quality of the layers. The presence of these modes has also been attributed to a slight misorientation of the grown film resulting from contamination greater than 0.3ML of carbon.

All SL's exhibit GaSb, InAs, and InSb LO modes. The InSb LO modes found in all of the SL's attest to the high quality InSb interfaces between the layers. The SL's with the GaInSb

barrier all show a well-defined InAs (LO) peak which is not seen in the SL's with the GaSb barriers. The intensity of the InSb (LO) at 192.3 cm^{-1} is also higher in the SL's with the GaInSb barrier. No Raman signal between 250 and 255 cm^{-1} corresponding to GaAs planar interfacial interface is observed in any of the samples under study. This is expected as no such interface was intentionally incorporated in the heterostructure. However, the lack of this Raman peak is consistent with the other observations of good quality of the interface with no possible interdiffusion across it. However, in sample SL1 the band at 275.5 cm^{-1} is due to GaAs in the interface of the InAs and GaSb layers [95].

InSb IF is seen for all samples under the 633 nm laser excitation. A peak in the range of 177 to 185 cm^{-1} for InSb (TO) mode is seen with the 514 nm Ar+ ion laser. Other bands were detected such as the weak bands at and 177.34 cm^{-1} that are the LO and the TO modes of InSb, which could be as an impurity in the interface of InAs and GaSb layers. In the case of all the SLs with the ternary barrier, a peak at 219 cm^{-1} was detected, which could be either due to InAs (TO) phonon or GaSb-like (TO), since the wavenumber of this mode is reported [93] to be calculated by the formula: GaSb-like (TO) = $227-20.68x-9.08x^2$ for a stress free sample of $In_xGa_{1-x}Sb$, which should be at 219.98 cm^{-1} for SL3, SL4 and SL6.

Further, the structure SL1 has the highest LO/TO ratio (1.6) for InAs out of all of the samples. While sample SL5 has the lowest LO/TO ratio (0.79) for InAs. Sample SL5 exhibits the highest LO/TO ratio (3.1) for InSb, while SL1 the lowest FWHM (5.09) for InSb (LO). SL3 as compared to the others samples exhibited the best crystalline quality with the lowest FWHM (7.41) and highest peak intensity (27500) for InAs (LO). In addition, it had the highest peak intensity (45000) for GaSb (LO) and InSb (LO) (8500) as well as the FWHM for InSb (TO). The nitride SLs (SL5 & SL6) showed degraded crystalline quality as compared to the non-nitride

SL's (SL1, SL2, SL3, and SL4). For example, SL6 has the lowest InAs (LO) peak intensity and SL5 has the highest GaSb (TO) FWHM of 22.8 cm^{-1}.

The stress calculation of InAs and GaSb layer is shown below for sample SL1 only; the results of the rest of the samples are computed similarly. As the InAs (LO) band at 238.06 cm^{-1} is red-shifted from the band of pure stress free InAs at 241.1 cm^{-1} , it is very likely that top InAs layer is stressed with a tensile stress of 0.67 GPa calculated [98] using the following equation (1)

$$\nu(LO)(InAs) = 241.1+4.57P-0.15P^2 \quad (1)$$

where, $\nu(LO)(InAs)$ is the frequency of the fitted band in (Figure 92) at 238.06 cm^{-1}. The GaSb layer might be stressed with a compressive stress of 0.18 GPa as well as its band at 233.4 cm^{-1} is blue-shifted compared to the stress free pure sample of GaSb, the peak position of which is reported at 232.6 cm^{-1}. The stress calculation is based [98] on equation (2)

$$\nu(LO)(GaSb) = 232.6+4.67P-0.11P^2 \quad (2)$$

where, $\nu(LO)(GaSb)$ is the frequency of the fitted band in (Figure 92) at 233.4 cm^{-1}.
The stresses are calculated similarly for other samples and are listed in Table 7-12. It is also to be noted the samples SL5and SL6 had an InAsN layer with 1.8% N content. Raman spectroscopy is very insensitive for any low concentration component and it is not a surprise that no Raman bands were detected at 500 cm^{-1} or higher due to InN-like modes. The bands at ~ 400 cm^{-1} are the overtones of the GaSb and InAs modes.

Figure 104 shows the Raman shift for InAs (LO) and GaSb (LO) modes for the six samples. It may be observed that the stresses on InAs top layer and GaSb layer beneath are complimentary, i.e. in case when the top InAs layer has a tensile stress the GaSb layer beneath has a compressive and vice versa. In the case of all binary SLs with 1ML InSb IF, GaSb exhibits a positive Raman shift signifying compressive stress while the ones with the ternary barrier

follow the same trend of the binary for 1ML InSb IF. However the latter SL in the absence of any intentional InSb IF (SL4) exhibits the largest negative Raman shift indicative of tensile stress. In the case of InAsN as well, the GaSb layer reverts back to compressive stress with the highest stress being exhibited with the ternary barrier. The green circle in Figure 104shows the InAs (LO) for sample SL6 has a positive shift as does the other ternary SLs (SL3 and SL4). SL6 differs from all the other ternary SLs because the GaInSb also a positive shift. The GaSb (LO) shift is unlike the other ternaries but is similar to the binaries SL's (SL1, SL2 and SL5). In addition, the InAs (LO) for SL6 has the highest positive shift out of all of the samples. The purple circle in Figure 104 shows a positive GaSb (LO) shift for samples SL1, SL2, and SL5, which are compressive. Also, these three samples have a GaSb barrier and a 1 ML InSb IF in common. The red circle in Figure 104 highlights that the InAs (LO) for samples SL1, SL2, and SL5 have a negative shift and are tensile. In addition, these three samples have a GaSb barrier and a 1 ML InSb IF. The black circle in Figure 104 shows the InAs (LO) for sample SL3 which has a positive shift and is compressive while, the GaSb (LO) is the most negative out of SL3, SL4, and SL6, which all have GaInSb barriers. The orange circle in Figure 104 highlights the InAs (LO) in samples SL3, SL4, and SL6, which have a positive shift and are compressive as compared to the samples SL1, SL2, and SL5 which all have GaSb barriers.

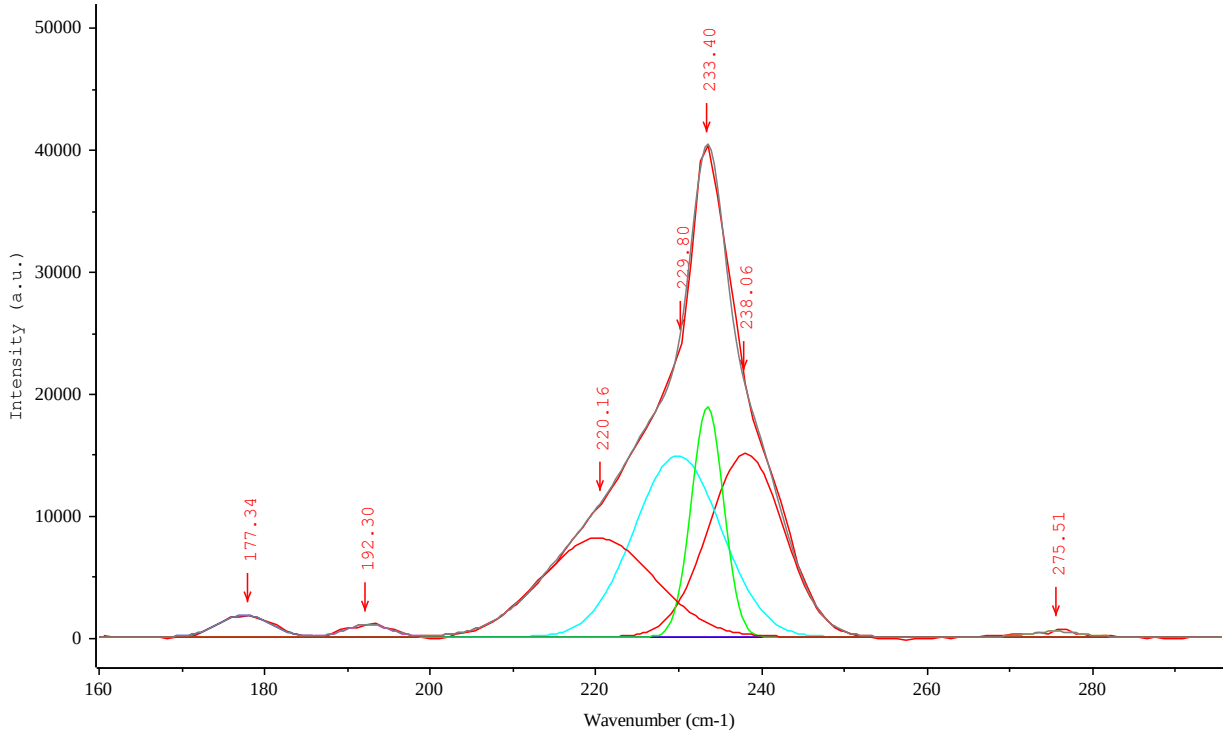

Figure 92 Raman spectra of sample SL1 with HeNe laser (632.8 nm)

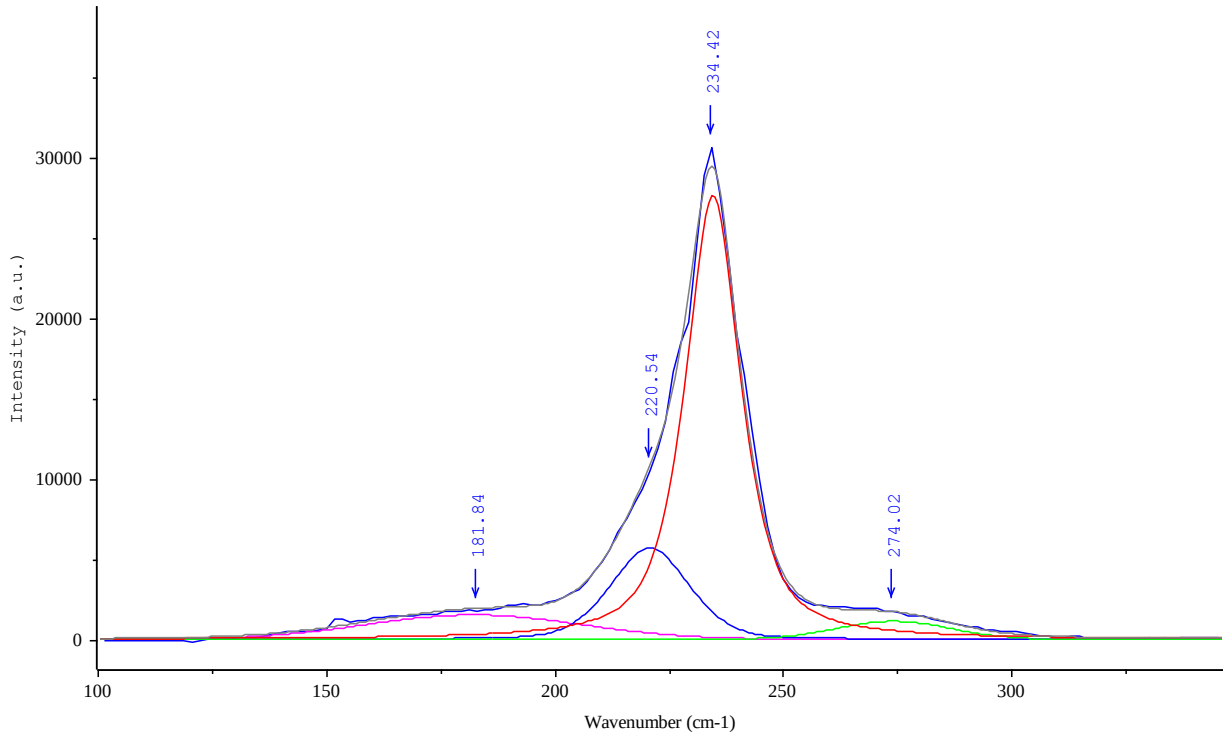

Figure 93 Raman spectra of sample SL1 with Ar+ ion laser (514.5 nm)

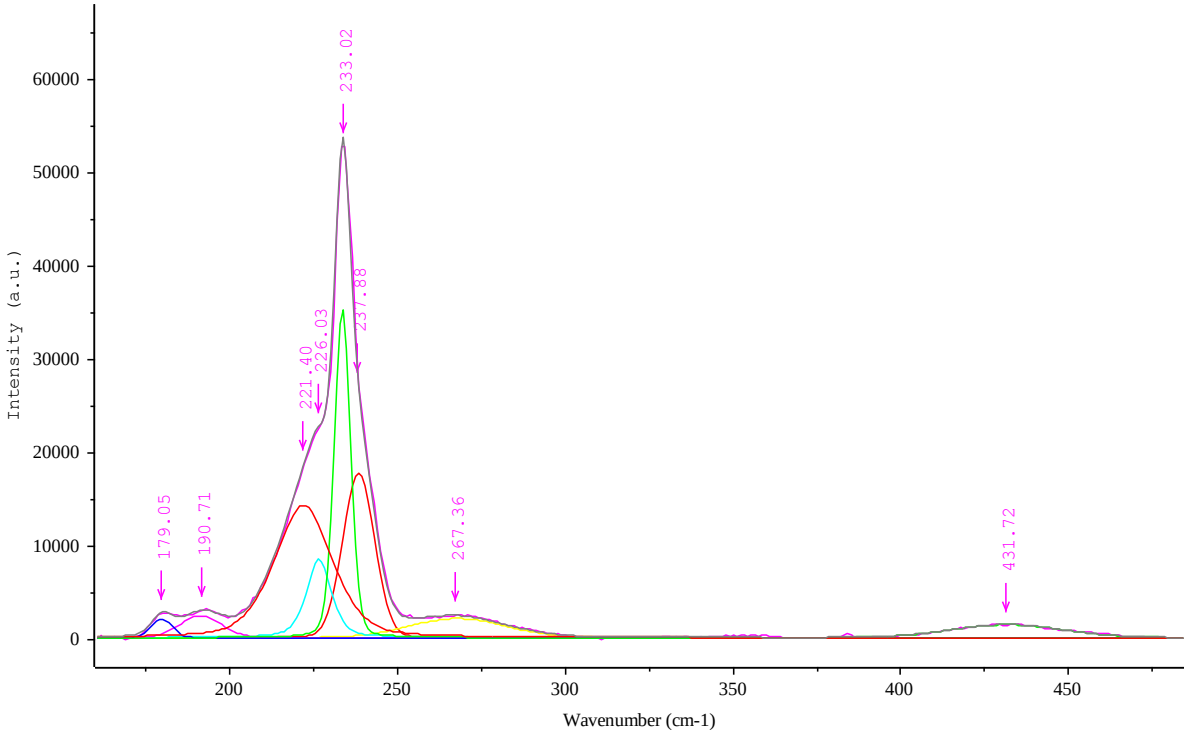

Figure 94 Raman spectra of sample SL2 with HeNe laser (632.8 nm)

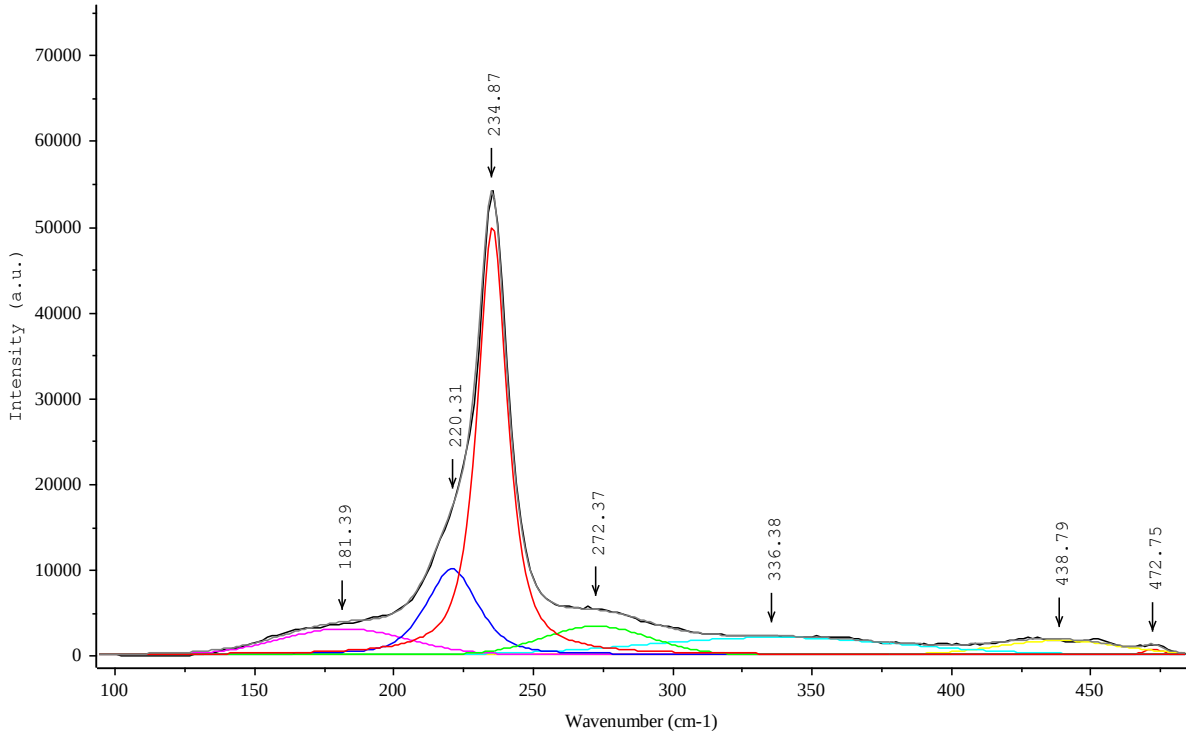

Figure 95 Raman spectra of sample SL2 with Ar+ ion laser (514.5 nm)

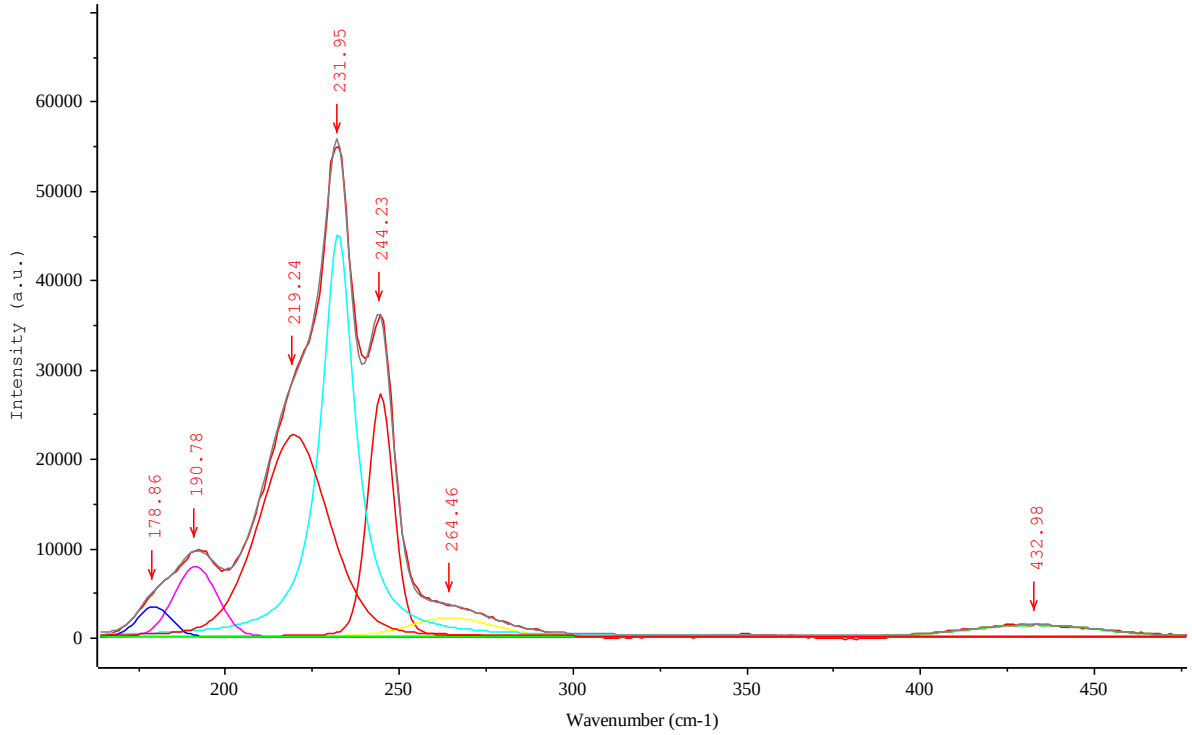

Figure 96 Raman spectra of sample SL3 with HeNe laser (632.8 nm)

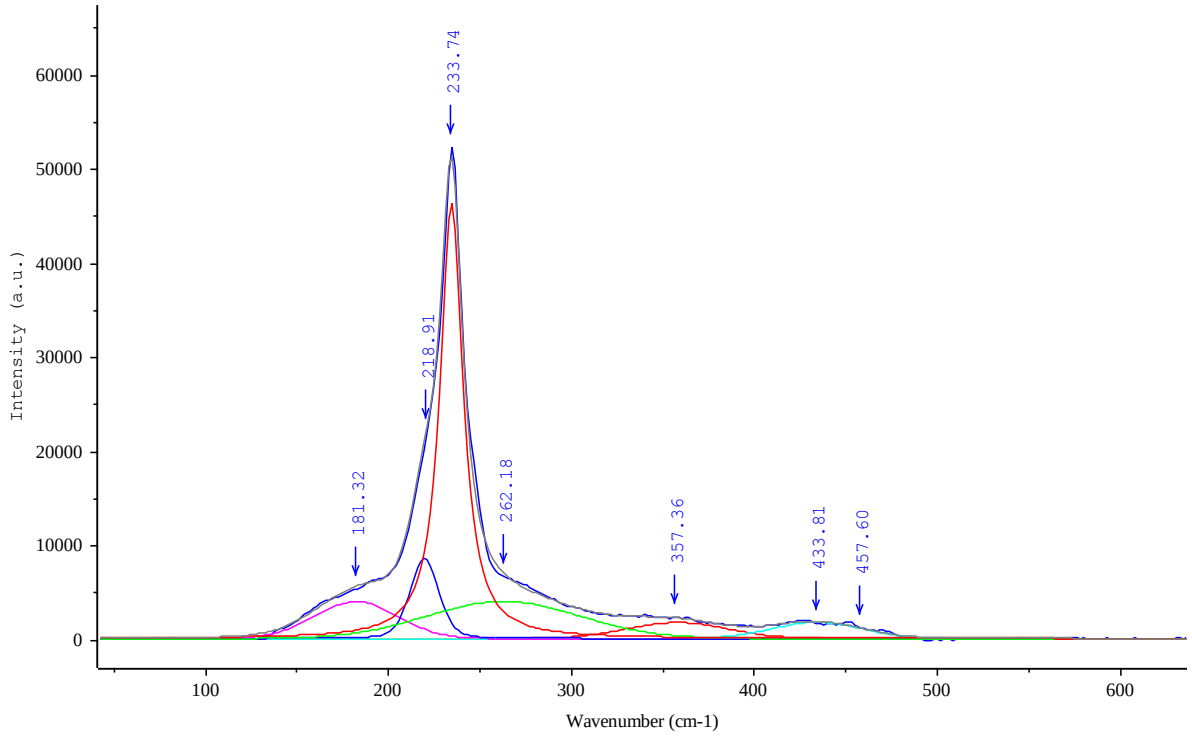

Figure 97 Raman spectra of sampleSL3 with Ar+ ion laser (514.5 nm)

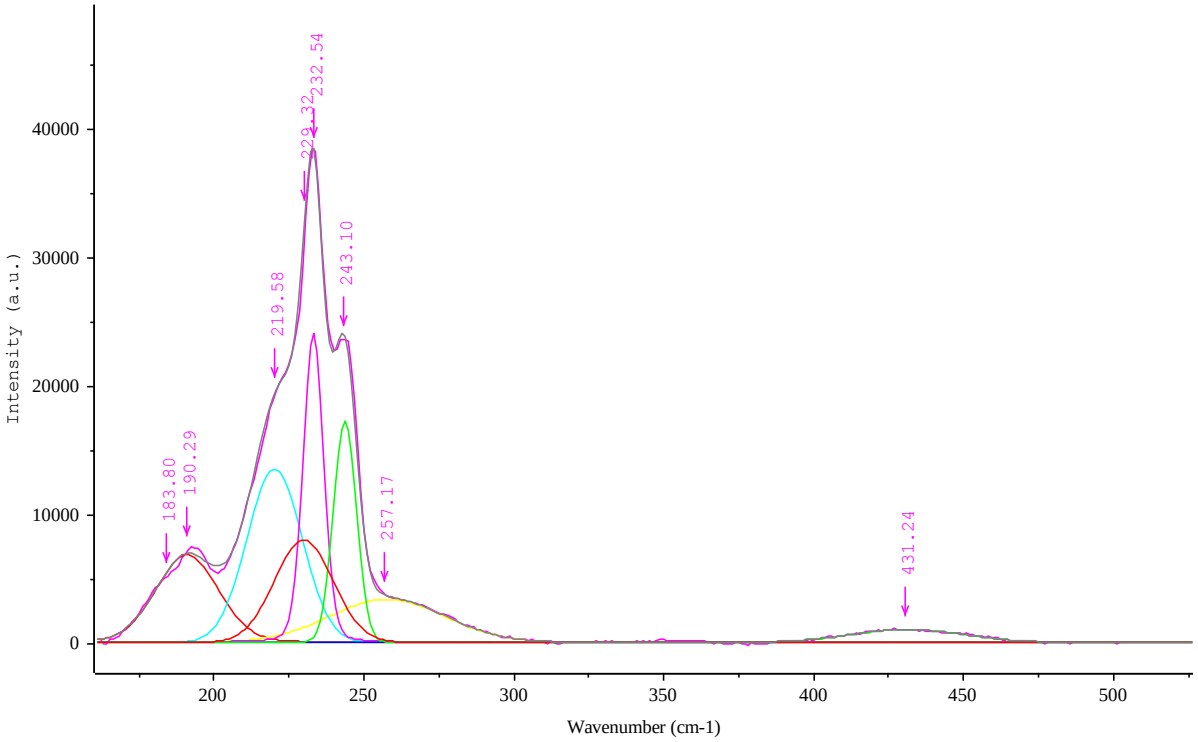

Figure 98 Raman spectra of sample SL4 with HeNe laser (632.8 nm)

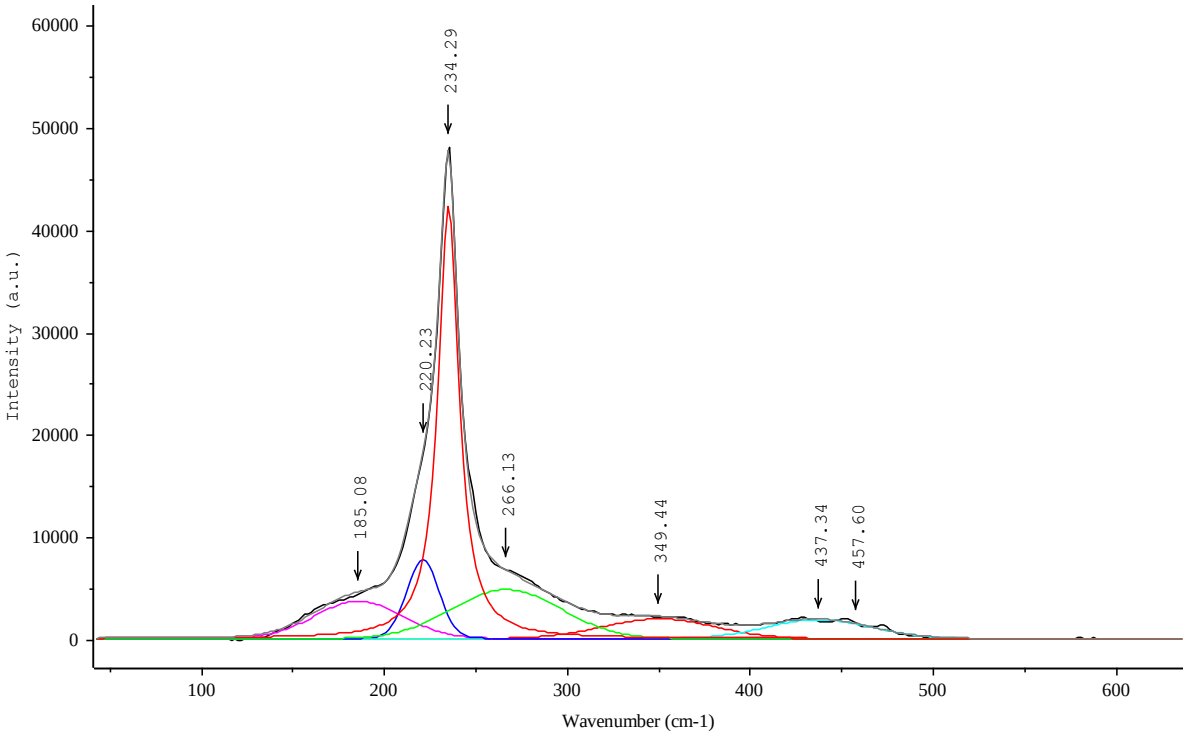

Figure 99 Raman spectra of sample SL4 with Ar+ ion laser (514.5 nm)

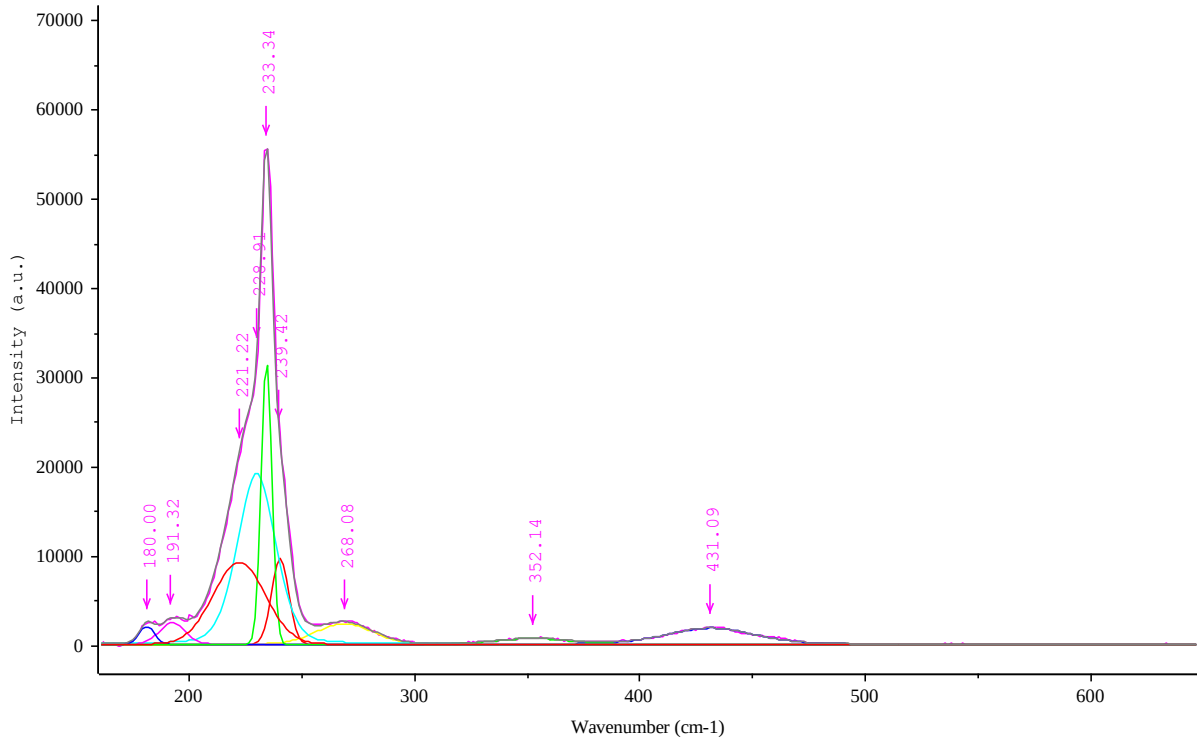

Figure 100 Raman spectra of sample SL5 with HeNe laser (632.8 nm)

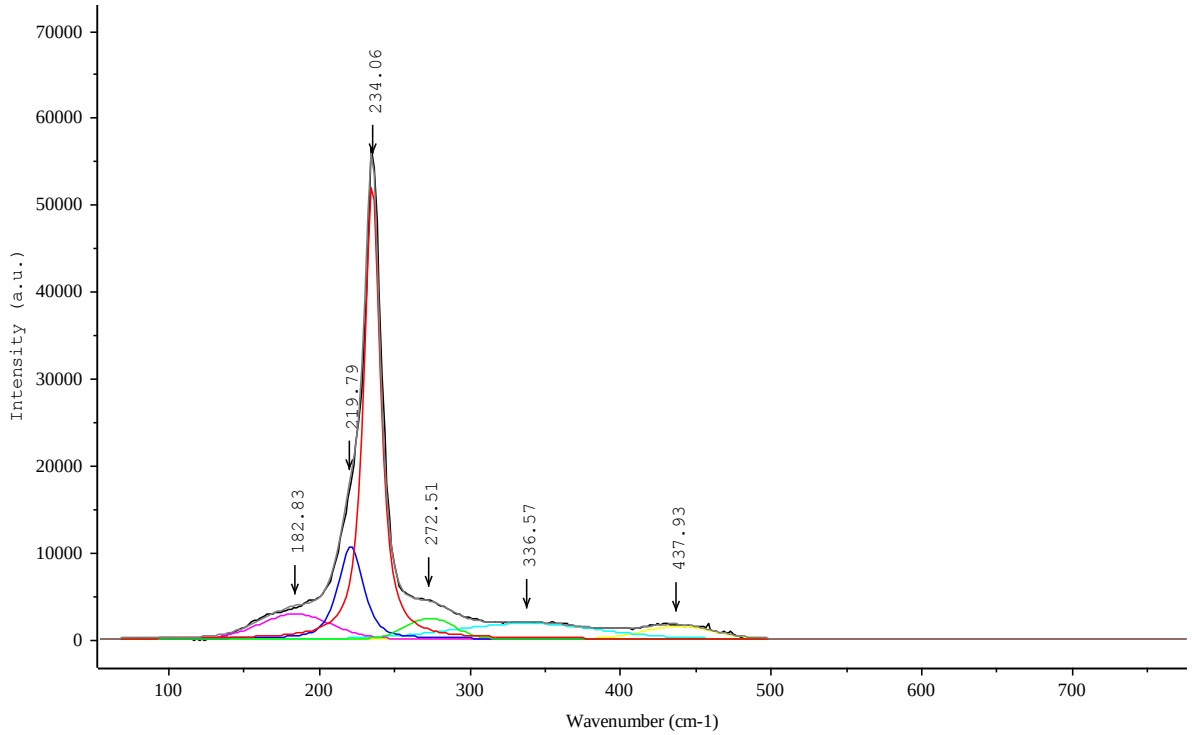

Figure 101 Raman spectra of sample SL5 with Ar+ ion laser (514.5 nm)

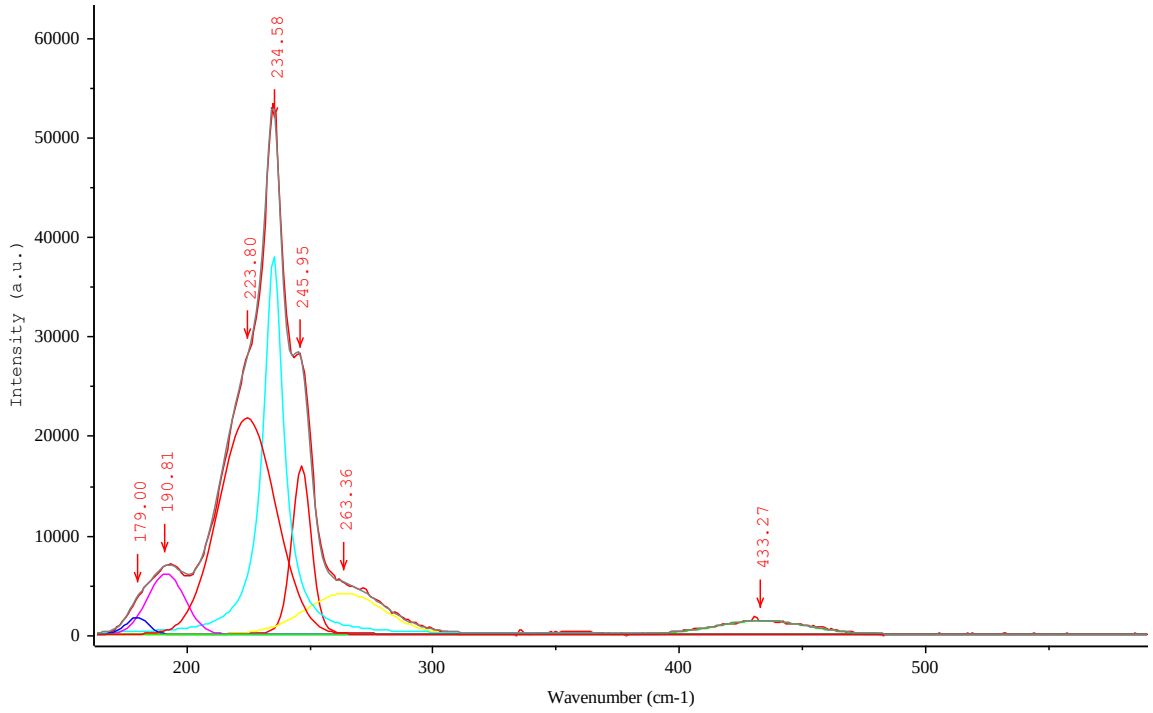

Figure 102 Raman spectra of sample SL6 with HeNe laser (632.8 nm)

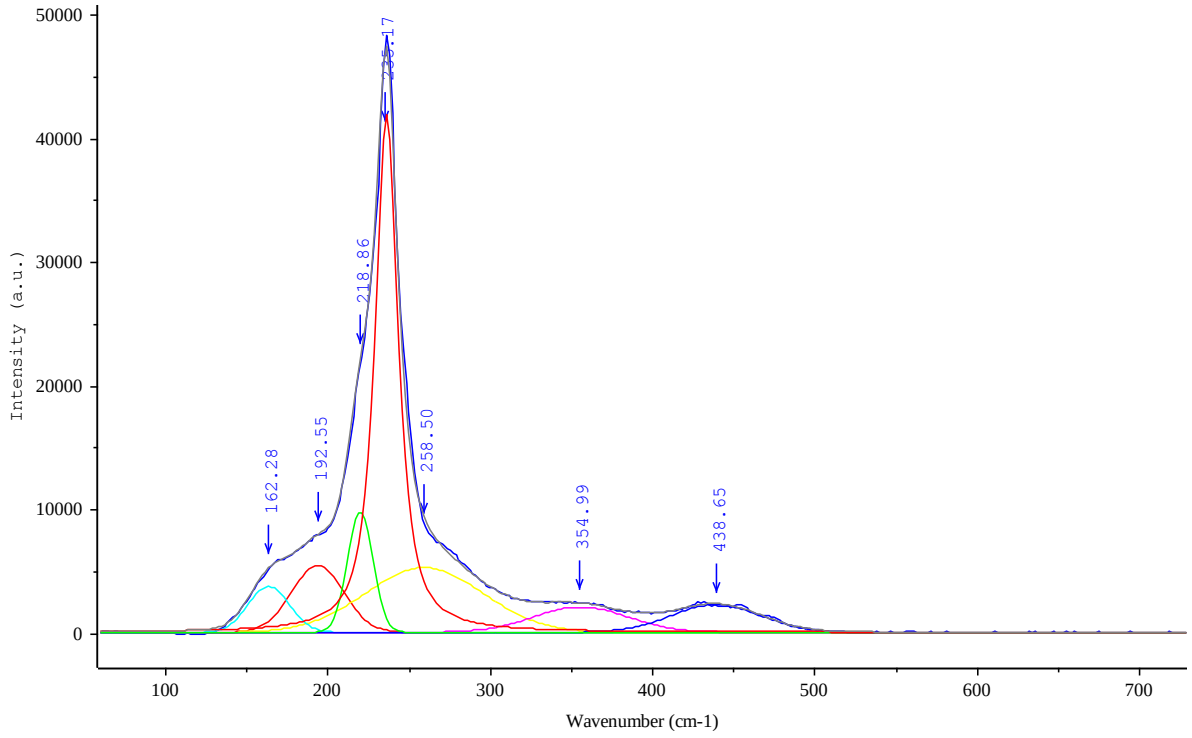

Figure 103 Raman spectra of sample SL6 with Ar+ ion laser (514.5 nm)

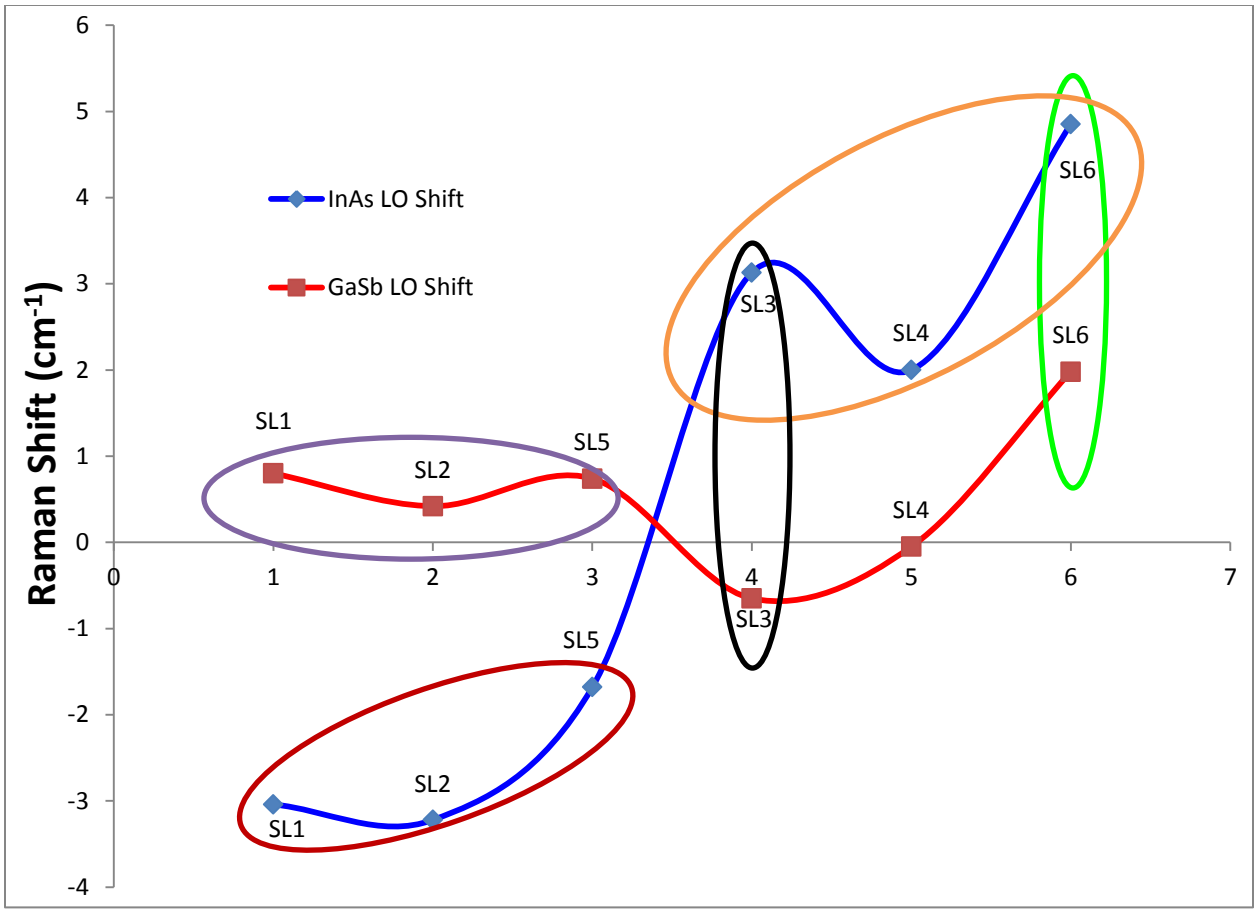

Figure 104 Raman shift for InAs (LO) and GaSb (LO)

Table 27

Sample SL1 analysis from Raman spectra

Laser	Band	Position (cm^{-1})	Stress (GPa)	Width (cm^{-1})
633 nm				
	InAs (LO)	238.06	-0.67	8.93
	GaSb (LO)	233.40	0.18	3.81
	GaSb (TO)	229.80		10.35
	InAs (TO)	220.16		13.34
	InSb (LO)	192.30		5.09
	InSb (TO)	177.34		6.09
	GaAs	275.51		5.73
514 nm				
	GaSb (LO)	234.42		13.52
	InAs (TO)	220.54		17.80
	InSb (TO)	181.84		47.16
	GaAs	274.02		25.08

Table 28

Sample SL2 analysis from Raman spectra

Laser	Band	Position (cm^{-1})	Stress (GPa)	Width (cm^{-1})
633 nm				
	InAs (LO)	237.88	-0.70	9.46
	GaSb (LO)	233.02	0.09	3.81
	GaSb (TO)	226.03		7.92
	InAs (TO)	221.40		18.07
	InSb (LO)	190.71		12.43
	InSb (TO)	179.05		6.3
	GaAs (TO)	267.36		28.77
	InAs 2(TO)	431.72		
514 nm				
	GaSb (LO)	234.88		12.12
	InAs (TO)	220.31		19.99
	InSb (TO)	181.39		44.82
	GaAs	272.37		38.08
	InAs 2(TO)	438.79		
	GaSb 2(LO)	472.75		

Table 29

Sample SL3 analysis from Raman spectra

Laser	Band	Position (cm^{-1})	Stress (GPa)	Width (cm^{-1})
633 nm				
	InAs (LO)	244.23	0.68	7.41
	GaSb (LO)	231.95	-0.14	10.69
	InAs (TO) and/or GaSb-like (TO)	219.24		20.19
	InSb (LO)	190.78		12.15
	InSb (TO)	178.86		3.39
	GaAs (TO)	264.46		23.76
	InAs 2(TO)	432.98		
514 nm				
	GaSb (LO)	233.74		14.92
	InAs (TO) and/or GaSb-like (TO)	218.91		16.11
	InSb (TO)	181.32		45.40
	GaAs	262.18		83.63
	InAs 2(TO)	433.81		
	GaSb 2(LO)	457.6		
	InSb 2(TO)	357.36		

Table 30

Sample SL4 analysis from Raman spectra

Laser	Band	Position (cm^{-1})	Stress (GPa)	Width (cm^{-1})
633 nm				
	InAs (LO)	243.10	0.44	7.69
	GaSb (LO)	232.55	-0.01	6.90
	GaSb-like(LO)	229.32		19.55
	InAs (TO) and/or GaSb-like(TO)	219.58		18.29
	InSb (LO)	190.29		21.21
	InSb (TO)			
	GaAs (TO)			
	InAs 2(TO)	431.24		
514 nm				
	GaSb (LO)	234.29		13.50
	InAs (TO) and/or GaSb-like(TO)	220.23		17.79
	InSb (TO)	185.08		47.95
	GaAs	266.13		59.51
	InAs 2(TO)	266.13		
	GaSb 2(LO)	437.34		
	InSb 2(TO)	457.6		

Table 31

Sample SL5 analysis from Raman spectra

Laser	Band	Position (cm^{-1})	Stress (GPa)	Width (cm^{-1})
633 nm				
	InAs (LO)	239.42	-0.37	7.57
	GaSb (LO)	233.34	0.16	4.70
	GaSb (TO)	228.91		17.46
	InAs (TO)	221.22		23.13
	InSb (LO)	191.32		11.35
	InSb (TO)	180.00		6.85
	GaAs	268.08		25.02
	InAs 2 (TO)	431.09		
	InSb 2 (TO)	352.14		
514 nm				
	GaSb (LO)	234.06		12.14
	InAs (TO)	219.80		18.09
	InSb (TO)	182.83		46.44
	GaAs	272.51		31.22
	InAs 2 (LO)	272.51		

Table 32

Sample SL6 analysis from Raman spectra

Laser	Band	Position (cm^{-1})	Stress (GPa)	Width (cm^{-1})
633 nm				
	InAs (LO)	245.95	1.06	7.78
	GaSb (LO)	234.58	0.43	9.15
	InAs (TO) and/or GaSb-like (TO)	223.80		22.80
	InSb (LO)	190.81		14.87
	InSb (TO)	179.00		8.83
	GaAs (TO)	263.36		31.44
	InAs 2 (TO)	433.27		
514 nm				
	GaSb (LO)	235.17		
	InAs (TO) and/or GaSb-like (TO)	218.86		15.70
	InSb (LO)	192.55		32.10
	InAs 2 (TO)	354.99		
	InSb 2 (TO)	438.65		

5.8 Optical Results and Analysis

5.8.1 Transmission. The transmission spectra shown in Figure 106 is bulk $Ga_{(x)}In_{(1-x)}Sb$ a GaSb substrate. For the bulk GaInSb samples a noticeable shift to a higher wavelength occurred with an increase in In composition with respect to the GaSb substrate.

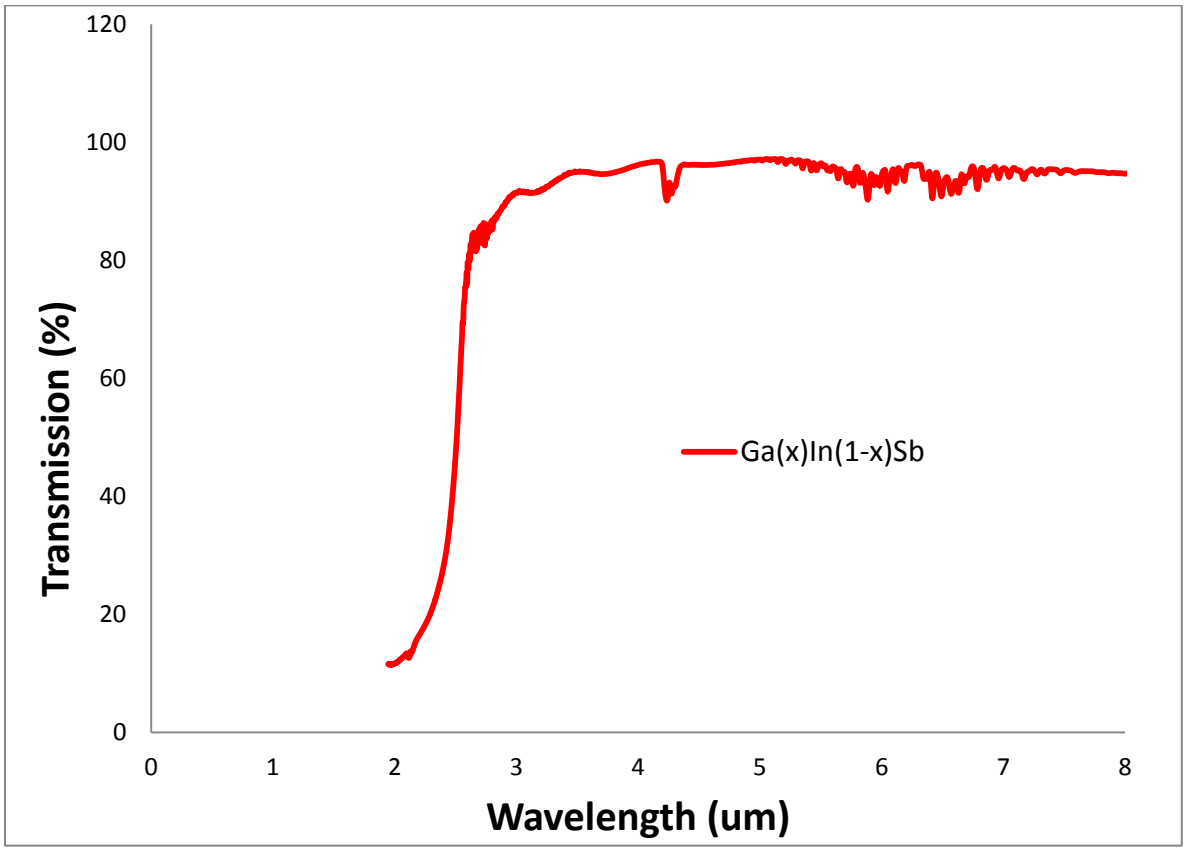

Figure 106 Transmission of $Ga_{(x)}In_{(1-x)}Sb$ bulk layer grown on a GaSb substrate

5.8.2 Optical band gap of GaInSb. Figure 107 shows and alpha squared energy squared plot of the same GaInSb epilayer (same sample as Figure 106) as a function of energy. The optical band gap of the sample was determined by the point of where extrapolation of the straight-line cuts the energy scale. The optical band gap was found to be around 485 meV which is equivalent to an elemental composition of $Ga_{.70}In_{.30}Sb$ at room temperature.

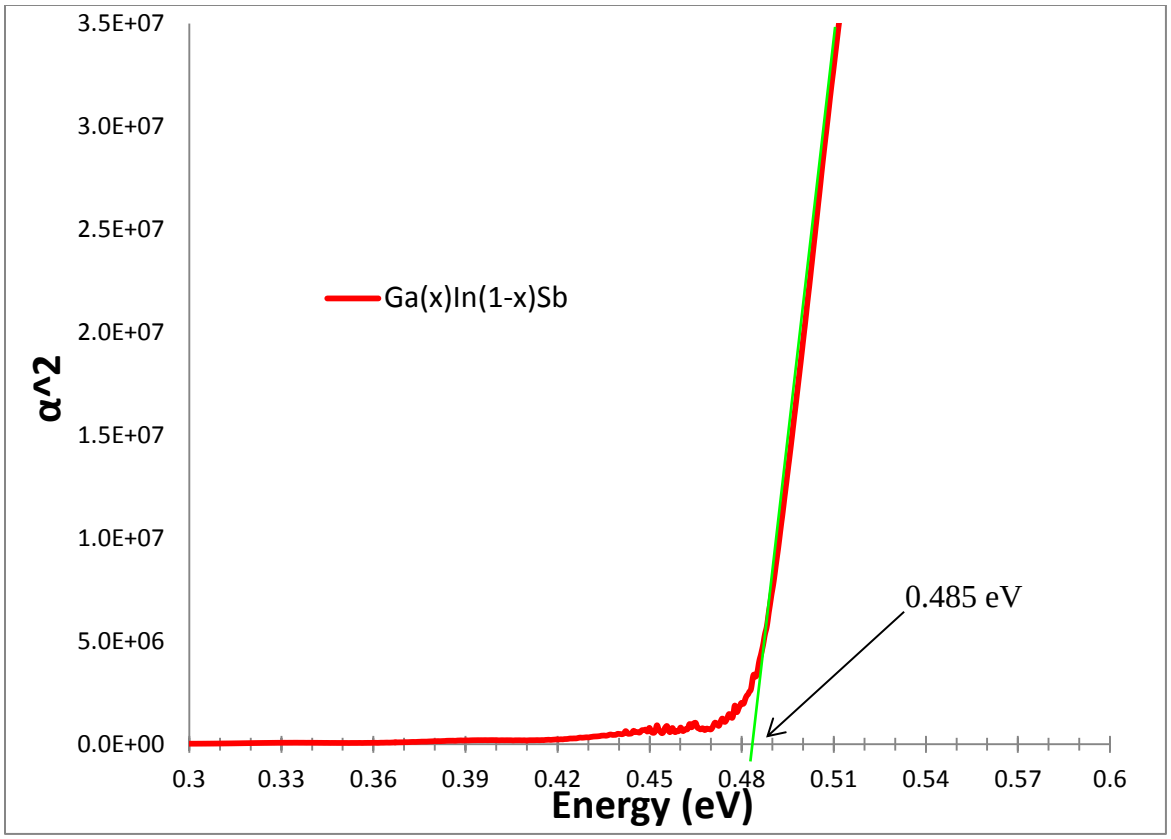

Figure 107 Optical band gap of $Ga_{(x)}In_{(1-x)}Sb$ bulk layer grown on a GaSb substrate

5.8.3 SL absorption spectra. Figure 108 shows an absorption comparison of 5 of the 6 SL structures studied in this work, excluding SL1. Sample SL2 has the highest overall absorption while SL3 exhibits the lowest. SL4 and SL6 had showed similar absorption spectra even though SL4 is non-nitride and SL6 is a nitride sample. SL5 has the highest absorption amongst nitrides and the second highest overall. SL5 also has a sharp absorption at 100 meV which is very distinct. The absorption coefficient was calculated using equation was (3)

$$\alpha = \frac{1}{t_f} ln \frac{100}{T} cm^{-1} \quad (3)$$

where, α is the absorption coefficient of the SL layer, t_f is the thickness of the SL layer and T is the % transmission of the SL minus the % transmission of the GaSb reference, which was measured by FTIR. Structure SL2 has energy of 62 meV (20 μm) which is the lowest amid the

non-nitride samples. The shape of the optical absorption spectra for ternary barrier is slightly different from those of all binary ones with the optical absorption coefficient increasing gradually with the wavelength as opposed to somewhat faster change in the absorption coefficient in all binary SL. SL3 has an optical cut off energy of 63 meV, which is very close to that of SL2. SL4 shows the largest blueshift, at 87 meV or 14.2 μm. The nitride structure SL5 exhibits the lowest optical cut off wavelength at 60 meV. SL6 has the highest energy amid the nitride samples at 72 meV which corresponds to 17.2 μm.

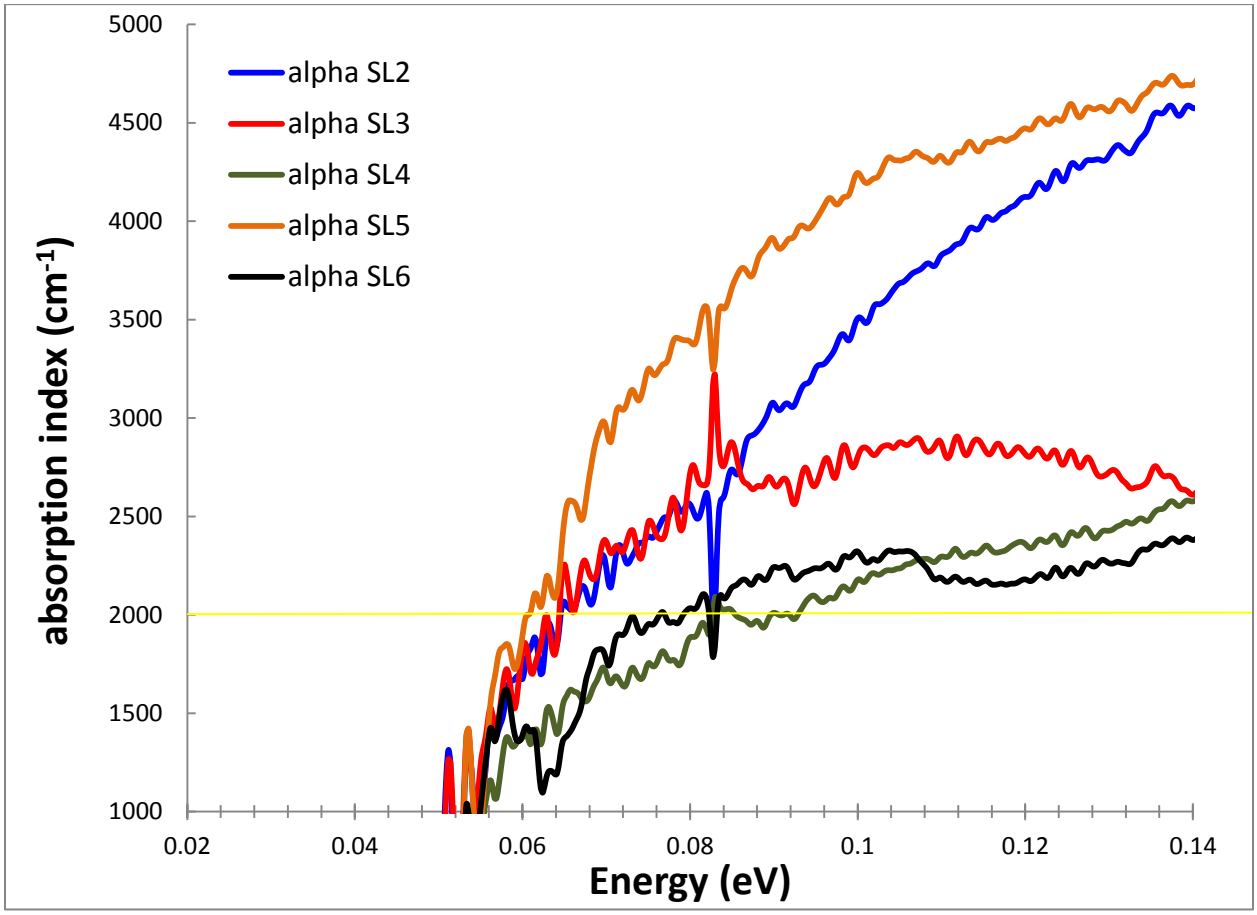

Figure 108 Absorption index of SL2, SL3, SL4, SL5, and SL6 at 2000 cm^{-1}

5.9 Discussion

All the superlattices grown were of excellent structural quality with no extended defects present as attested by the HRXRD spectra and presence of at least 7 diffraction satellite peaks,

from RSM spectra as well as the STEM images exhibiting sharp interfaces and well defined sublayers. The thickness determined from the RHEED oscillations, HRXRD spectra and STEM images were in excellent agreement within the (+/-) 1 ML. The optical cut off wavelength defined as the wavelength where the absorption coefficient reaches 2000 cm^{-1} was found to be in the range of 14.6 μm to 20.6 μm. Following is the salient differences between the different SLs investigated.

The two binary SLs are quite similar in most of their characteristics with the optical cut off length around 20 μm, though the surface morphology is somewhat different. SL2 exhibits pronounced undulations, characteristic of tensile strain within the SL layer. Raman InAs (LO) FWHM is worse for SL2. With the introduction of GaInSb barrier, Raman FWHM of GaSb (LO) gets worse. SL3 which does not have any intentional interfacial layer exhibits the highest structural and interfacial quality as attested by the presence of largest number of diffraction satellite peaks up to 9 in the (004) HRXRD data as opposed to the 7 satellite peaks observed in other SLs investigated. This is further attested by the lowest FWHM of the SL^{0th} and SL^{1st} order satellite peaks in the range of 34 - 42 arc-seconds. These also exhibit the lowest RMS roughness of 0.24 nm less than 1 ML, lowest Raman FWHM for InAs LO and highest intensity of InAs (LO), GaSb (LO) and InAs LO/TO peak intensity ratio. However Raman shifts indicate the most tensile stress for GaInSb consistent with the (004) HRXRD peak indicative of tensile strained SL though the entire stack is pseudomorphically lattice matched to the substrate. The optical absorption edge of this sample is around 19.6 μm. With the addition of the InSb interfacial layer and simultaneously increasing the InAs layer thickness resulted in the next best FWHM of 44 arc-seconds for the SL^{0th} order satellite peak of structure SL4.

Addition of N to InAs with the GaSb barrier layer improved the FWHM of the SL^{0th} satellite peak from 82 arc sec to 57 arc-sec for corresponding constituent layer thicknesses, with the AFM roughness decreasing from 2.59 nm to 1.88 nm. Surface morphology does not exhibit any change exhibiting terracing with the edges being more rounded hillocks as in the non-nitride SL. InAs (LO) and GaSb (LO) FWHM as well as their LO/TO ratios for both the samples are similar. However, InAs is more compressive when N is added which is not clearly understood. Both of them exhibit broadening to the right indicative of layer being tensile strained with partial relaxation. The FWHM of the SL^{1st} order is complimentary i.e. the SL^{+1} is better in nitride SL in comparison to non-nitride SL. Thus, nitride layers appear to be somewhat better than their binary non-nitride counterpart. The optical cut off wavelength was around 20.6 µm, the longest wavelength amongst all the samples investigated. In the case of GaInSb barrier the addition of N to InAs again compressively strains the SL stack as in the case of GaSb. Also in this case, the Raman shifts were positive for both GaSb and InAs unlike any other samples investigated The SL^{0th}order in the (004) HRXRD peak could not be resolved due to the broad HRXD peak. Further, drastic degradation in the quality of the SL structures is evident from the highest FWHM exhibited by x-ray rocking curve of the first as well as higher order satellite peaks and largest AFM RMS roughness amongst all the samples examined. All the satellite peaks show a shoulder on the left side which is more likely due to the compositional gradient as also confirmed by the broadening of the reciprocal lattice point in the vertical (Qy) direction. The optical cut-off wavelength for this structure was 17.2 µm.

Thus, the crystal and morphology of the nitride SL with GaSb barrier appears to be the best amongst the samples grown with the longest cut-off wavelength of 20.6 µm with high absorption coefficient. STEM images of these samples indicate sharp and clear interfaces for the

non-nitride as well as the nitride sample with GaSb being the barrier. InSb of 1ML is also succinctly seen thus at least showing no evidence of interface mixing as predicted by the HRXRD. However, it is to be noted the substantial difference between the two analysis are that the HRXRD data represents the average characteristics of the sample while the STEM sampling is only a very small area and hence not representative of the entire sample.

CHAPTER 6

Conclusion and Future Work

6.1 Conclusion

In this work a comprehensive study of InAs/GaSb, InAs/GaInSb, InAsN/GaSb and InAsN/GaInSb SLs grown by MBE, have been carried out using different characterization techniques. The contributions from this work are individually listed below.

1. MBE growth of 4 different types of high quality SLs and a systematic and comprehensive study has been made correlating the structural quality with the vibrational modes, STEM micrographs and optical properties.
2. The SLs exhibit excellent structural quality as attested by the HRXRD diffraction satellite peaks up to 7^{th} order and extending up to the 9^{th} order on the best SL. Most of the SLs except one were tensile strained and pseudomorphic lattice matched to GaSb substrate. All the SLs were defect free with sharp interfaces and well defined sublayers as attested by HRXRD and asymmetric RSM spectra as well as STEM images.
3. A cut-off wavelength of 20 μm was achieved in majority of SLs
4. Amongst the non-nitride SL investigated InAs/GaInSb SL (SL3) without an intentional interfacial layer was found to be pseudomorphically lattice matched to GaSb substrate and excellent structural quality exhibiting a cut off at 20 μm and high absorption coefficient.
5. The nitride SL (SL5) with a GaSb barrier also exhibited excellent structural quality with an optical cut off wavelength of 20.6 μm. These are the first reports on the InAsN/Ga(In)Sb SL to the best of our knowledge.

6. The nitride SL (SL6) with a GaInSb barrier exhibited the worst structural characteristics as attested by broad HRXRD satellite peaks as well as broad RSM spectra. The corresponding optical absorption coefficients were also low in the VLWIR region.
7. The interfacial layers play an important role in strain balancing. The SLs with overall strain less than -9.49×10^{-4} and with the resultant stress towards the tensile stress is found to provide the best results.

These are preliminary data and there is considerable room for improvement in the nitride layer in particular with GaSb as the barrier layer

6.2 Future Work

This work was started by first optimizing the well-studied InAs/Ga(In)Sb material systems. An extensive investigation was done to optimize the SL structure in preparation of a dilute amount of N being added to InAs. The addition of N to InAs proved to be challenging but the results of the InAsN/GaSb SL were comparable and in most cases better than the non-nitride SLs. More work needs to be done in the optimization of the InAsN/GaInSb SL which includes different N incorporation in addition to the standard parameters used in the optimization of the SL structure. Also these could be investigated for higher temperature operation for LWIR region.

With that being said, after further optimization of the nitride SL's the next step should be device fabrication. The SL optimization in this work has produced the quality necessary for these structures to be fabricated into PIN single pixel photodetector devices. With a photodetector structures can now be measured to show their spectral response, and responsivity to determine the quantum efficiency. Also the I-V measurements can be investigated to determine the current-voltage relationship.

As Shockley Read Hall (SRH) current is shown to be the dominant factor in comparison to Auger, measurement of the lifetime of the carrier is important. In particular this becomes more important in the nitride structures as N is known to degrade the lifetime of the carriers. However, in our work the N concentration was intentionally kept very low to reduce this effect. Also other modifications of the structure, such as nBn structure being developed by Dr. Sanjay Krishna's group [99, 100] has shown to significantly decrease the SRH currents.

Demonstrations of dilute nitride SLs for VLWIR in this work opens up another possibility of fabricating two color detectors. A combination of LWIR and VLWIR with dilute nitride may be extended to a three color detector.

References

1. Meimei Z, T., *Type II strained layer superlattice: A potential future IR solution.* Infrared Physics & Technology, 2009. **52**(6): p. 322-325.

2. Zheng, L., *Type II strained layer superlattice: a potential infrared sensor material for space.* Proc. SPIE, 2008. **6900**(1): p. 69000F.

3. Rogalski, A., *Infrared detectors: status and trends.* Progress in quantum electronics, 2003. **27**(2): p. 59-210.

4. Rogalski, A. and P. Martyniuk, *InAs/GaInSb superlattices as a promising material system for third generation infrared detectors.* Infrared Physics & Technology, 2006. **48**(1): p. 39-52.

5. Ashley, T., *Dilute antimonide nitrides for very long wavelength infrared applications.* Proc. SPIE, 2006. **6206**(1): p. 62060L.

6. Jefferson, P.H., et al., *Growth of dilute nitride alloys of GaInSb lattice-matched to GaSb.* Journal of Crystal Growth, 2007. **304**(2): p. 338-341.

7. Aina, L., et al., *High detectivity dilute nitride strained layer superlattice detectors for LWIR and VLWIR applications.* Infrared Physics & Technology, 2009. **52**(6): p. 310-316.

8. Buckle, L., et al., *Growth and characterisation of dilute antimonide nitride materials for long-wavelength applications.* Microelectronics Journal, 2009. **40**(3): p. 399-402.

9. Krishna, S., *The infrared retina.* Journal of Physics D: Applied Physics, 2009. **42**: p. 234005.

10. *The Electromagnetic Spectrum* 02-25-2012]; Available from: http://www.cyberphysics.co.uk/topics/light/emspect.htm.

11. Razeghi, M., *Technology of quantum devices*. 2010: Springer Verlag.

12. Hoffman, D., *The importance of band alignment in VLWIR type-II InAs/GaSb heterodiodes containing the M-structure barrier.* Proc. SPIE, 2009. **7222**(1): p. 722215.

13. Razeghi, M., *Type-II superlattice photodetectors for MWIR to VLWIR focal plane arrays.* Proc. SPIE, 2006. **6206**(1): p. 62060N.

14. Aifer, E., *Dual band LWIR/VLWIR type-II superlattice photodiodes.* Proc. SPIE, 2005. **5783**(1): p. 112.

15. Kim, S.-H. and S.S. Li, *Theoretical investigation of InAs/GaInSb type-II superlattice infrared detectors for long wavelength and very long wavelength infrared applications.* Physica E: Low-dimensional Systems and Nanostructures, 2003. **16**(2): p. 199-208.

16. Brown, G., *Type-II superlattice photodiodes: an alternative for VLWIR detection.* Proc. SPIE, 2003. **5074**(1): p. 191.

17. Sarney, W.L., et al., *New Approaches to Direct Bandgap III-V Materials for LWIR Detector Applications.* AIP Conference Proceedings, 2011. **1416**(1): p. 59-61.

18. Razeghi, M., et al., *Recent Advances in LWIR Type-II InAs/GaSb Superlattice Photodetectors and Focal Plane Arrays at the Center for Quantum Devices.* Proceedings of the IEEE, 2009. **97**(6): p. 1056-1066.

19. Hill, C.J., et al., *MBE grown type-II MWIR and LWIR superlattice photodiodes.* Infrared Physics & Technology, 2007. **50**(2-3): p. 187-190.

20. Tidrow, M. and W. Dyer, *Infrared sensors for ballistic missile defense.* Infrared Physics & Technology, 2001. **42**(3-5): p. 333-336.

21. *Image at various wavelengths*. 03-01-2012]; Available from: http://www.openscenegraph.org/projects/osg/wiki/Screenshots/SE-FAST-IR.

22. Rogalski, A., *New material systems for third generation infrared photodetectors.* Opto-Electronics Review, 2008. **16**(4): p. 458-482.

23. Manasreh, M.O. and G.J. Brown, *Semiconductor Quantum Wells and Superlattices for Long-Wavelength InfraredDetectors, ed*. Artech House. 1993. 1-2.

24. *Blackbody Spectrum*. 02-25-2012]; Available from: http://commons.wikimedia.org/wiki/File:BlackbodySpectrum_loglog_150dpi_en.png.

25. *Atmospheric Transmission*. 02-25-2012]; Available from: http://www.globalwarmingart.com/wiki/File:Atmospheric_Transmission_png.

26. Rogalski, A., J. Antoszewski, and L. Faraone, *Third-generation infrared photodetector arrays.* Journal of applied physics, 2009. **105**(9): p. 091101.

27. Lawson, W., et al., *Preparation and properties of HgTe and mixed crystals of HgTe-CdTe.* Journal of Physics and Chemistry of Solids, 1959. **9**(3-4): p. 325-329.

28. Rogalski, A., *HgCdTe infrared detector material: history, status and outlook.* Reports on Progress in Physics, 2005. **68**: p. 2267.

29. Plis, E., et al., *Molecular beam epitaxy growth and characterization of type-II InAs/GaSb strained layer superlattices for long-wave infrared detection.* Journal of Vacuum Science & Technology: Part B, 2010. **28**(3): p. C3G13-C3G18.

30. Chu, J. and D. Tang, *Recent progress on HgCdTe at the national laboratory for infrared physics in china.* Journal of electronic materials, 1996. **25**(8): p. 1176-1182.

31. Capper, P., *Bulk Growth of Mercury Cadmium Telluride (MCT).* Mercury Cadmium Telluride, 2011: p. 1-20.

32. Kim, H., et al., *Performance improvement of InAs/GaSb strained layer superlattice detectors by reducing surface leakage currents with SU-8 passivation.* Applied physics letters, 2010. **96**: p. 033502.

33. Rogalski, A., *Fundamentals of infrared detector technologies*. 2009: CRC.

34. Varshni, Y.P., *Temperature dependence of the energy gap in semiconductors.* Physica, 1967. **34**(1): p. 149-154.

35. Herbert, K., *The 6.1Å family (InAs, GaSb, AlSb) and its heterostructures: a selective review.* Physica E: Low-dimensional Systems and Nanostructures, 2004. **20**(3-4): p. 196-203.

36. Razeghi, M. and B.M. Nguyen, *Band gap tunability of Type II Antimonide-based superlattices.* Physics Procedia, 2010. **3**(2): p. 1207-1212.

37. Sai Halasz, G., R. Tsu, and L. Esaki, *A new semiconductor superlattice.* Applied physics letters, 1977. **30**(12): p. 651-653.

38. Sai-Halasz, G., L. Esaki, and W. Harrison, *InAs-Gasb superlattice energy structure and its semiconductor-semimetal transition.* Physical Review B, 1978. **18**(6): p. 2812.

39. Claessen, L., et al., *Pressure dependence of band offsets in an InAs-GaSb superlattice.* Physical review letters, 1986. **57**(20): p. 2556-2559.

40. Mohseni, H., *Growth and characterization of InAs/GaSb photoconductors for long wavelength infrared range.* Appl. Phys. Lett., 1997. **71**(10): p. 1403.

41. Mohseni, H., et al., *Uncooled InAs-GaSb type-II infrared detectors grown on GaAs substrates for the 8-12-μm atmospheric window.* Quantum Electronics, IEEE Journal of, 1999. **35**(7): p. 1041-1044.

42. Olafsen, L., et al., *Negative luminescence from type-II InAs/GaSb superlattice photodiodes.* Applied physics letters, 1999. **74**: p. 2681.

43. Wei, Y., *Advanced InAs/GaSb superlattice photovoltaic detectors for very long wavelength infrared applications.* Appl. Phys. Lett., 2002. **80**(18): p. 3262.

44. Brown, G.J., S. Houston, and F. Szmulowicz, *Type-II InAs/GaSb superlattices for very long wavelength infrared detectors.* Physica E: Low-dimensional Systems and Nanostructures, 2004. **20**(3-4): p. 471-474.

45. Haugan, H., *Band gap tuning of InAs/GaSb type-II superlattices for mid-infrared detection.* J. Appl. Phys., 2004. **96**(5): p. 2580.

46. Liu, C., Y. Li, and Y. Zeng, *Progress in Antimonide Based III-V Compound Semiconductors and Devices.* 2010.

47. Huang, Y., *InAs/GaSb type-II superlattice structures and photodiodes grown by metalorganic chemical vapor deposition.* Appl. Phys. Lett., 2010. **96**(25): p. 251107.

48. Walther, M., *Defect density reduction in InAs/GaSb type II superlattice focal plane array infrared detectors.* Proc. SPIE, 2011. **7945**(1): p. 79451N.

49. Esaki, L. and R. Tsu, *Superlattice and Negative Differential Conductivity in Semiconductors.* IBM Journal of Research and Development, 1970. **14**(1): p. 61-65.

50. Kapon, E., M.C. Tamargo, and D.M. Hwang, *Molecular beam epitaxy of GaAs/AlGaAs superlattice heterostructures on nonplanar substrates.* Applied physics letters, 1987. **50**(6): p. 347-349.

51. Esaki, L., *InAs-GaSb superlattices—synthesized narrow-gap semiconductors and semimetals.* Narrow Gap Semiconductors Physics and Applications, 1980: p. 302-323.

52. Grein, C., P. Young, and H. Ehrenreich, *Minority carrier lifetimes in ideal InGaSb/InAs superlattices.* Applied physics letters, 1992. **61**(24): p. 2905-2907.

53. A, R., *Material considerations for third generation infrared photon detectors.* Infrared Physics & Technology, 2007. **50**(2-3): p. 240-252.

54. *Band Energy Shifts Under Strain*. 02-25-2012]; Available from: http://inst.eecs.berkeley.edu/~ee232/fa08/lectures/EE232-15.pdf.

55. Brown, G.J. and F. Szmulowicz, *InAs/InGaSb superlattices for very long wavelength infrared detection.* SPIE Proceedings on Photodetectors: Materials and Devices VI, 2001. **4288**: p. 200-208.

56. Youngdale, E., *Auger lifetime enhancement in InAs-Ga1-xInxSb superlattices.* Appl. Phys. Lett., 1994. **64**(23): p. 3160-3162.

57. Young, P.M., et al., *Superlattice excitons and optical absorption.* Journal of applied physics, 1993. **74**(12): p. 7369-7378.

58. Romanov, A.E., et al., *Threading dislocation reduction in strained layers.* Journal of applied physics, 1999. **85**(1): p. 182-192.

59. Heller, E.R., et al., *Superlattice parameters for optimum absorption in InAs/InxGa1-xSb superlattice infrared detectors.* Journal of applied physics, 1995. **77**(11): p. 5739-5746.

60. Johnson, J.L., et al., *Electrical and optical properties of infrared photodiodes using the InAs/Ga[sub 1 - x]In[sub x]Sb superlattice in heterojunctions with GaSb.* Journal of applied physics, 1996. **80**(2): p. 1116-1127.

61. Fuchs, F., *High performance InAs/Ga1-xInxSb superlattice infrared photodiodes.* Appl. Phys. Lett., 1997. **71**(22): p. 3251.

62. Lin, C.H.T., et al. *Mid-infrared photodetectors based on the InAs/InGaSb type-II superlattices*. 1998. SPIE.

63. Lin, C.H.T., et al. *Type-II InAs/InGaSb SL photodetectors*. 2000. SPIE.

64. Anselm, K., et al., *Long-wavelength infrared InAs/InGaSb type-II superlattice photovoltaic detectors.* Proc. SPIE, 2001. **4288**(1): p. 183.

65. Yang, Q.K., et al., *Investigation of trap-assisted tunneling current in InAs/(GaIn)Sb superlattice long-wavelength photodiodes.* Applied physics letters, 2002. **81**(25): p. 4757-4759.

66. Loehr, J.P., *(InAs)n/(InxGa1-xSb)m superlattice structures for optimal miniband-edge absorption.* Applied physics letters, 1995. **67**(17): p. 2509-2511.

67. Roslund, J. and T. Andersson, *Structural investigations of InAs/Ga1-xInxSb strained layer superlattices.* Opto-Electron. Rev., 1997. **5**(2): p. 129-132.

68. Bürkle, L. and F. Fuchs, *Handbook of Infrared Detection Technologies ed M Henini and M Razeghi*. 2002, London: Elsevier. p. 159-189.

69. Brown, G., *Type-II InAs/GaInSb superlattices for infrared detection: an overview.* Proc. SPIE, 2005. **5783**(1): p. 65.

70. Young, M.H., et al., *Recent advances in Ga1−xInxSbInAs superlattice IR detector materials.* Applied Surface Science, 1998. **123–124**(0): p. 395-399.

71. Hoffman, C., et al., *Interface roughness scattering in semiconducting and semimetallic InAs Ga1-xInxSb superlattices.* Applied physics letters, 1993. **63**(16): p. 2210-2212.

72. Daly, M., et al., *Interface composition dependence of the band offset in InAs/GaSb.* Surface science, 1996. **361**: p. 205-208.

73. Thibado, P., et al., *Origins of interfacial disorder in GaSb/InAs superlattices.* Applied physics letters, 1995. **67**: p. 3578.

74. Tomich, D., et al., *Study of interfaces in GaInSb/InAs quantum wells by high-resolution X-ray diffraction and reciprocal space mapping.* Journal of Crystal Growth, 1999. **201**: p. 868-871.

75. Wagner, J., et al., *InAs/(GaIn)Sb superlattices for IR optoelectronics: Strain optimization by controlled interface formation.* Physica E: Low-dimensional Systems and Nanostructures, 1998. **2**(1–4): p. 320-324.

76. Fuchs, F., et al. *Optoelectronic properties of photodiodes for the mid-and far-infrared based on the InAs/GaSb/AlSb materials family*. 2001.

77. Wei, Y., *High quality type II InAs/GaSb superlattices with cutoff wavelength ~3.7 µm using interface engineering.* J. Appl. Phys., 2003. **94**(7): p. 4720.

78. Wei, Y., *High-performance type-II InAs/GaSb superlattice photodiodes with cutoff wavelength around 7 µm.* Appl. Phys. Lett., 2005. **86**(9): p. 091109.

79. Plis, E., *Midwave infrared type-II InAs/GaSb superlattice detectors with mixed interfaces.* J. Appl. Phys., 2006. **100**(1): p. 014510.

80. Rodriguez, J.B., et al., *MBE growth and characterization of type-II InAs/GaSb superlattices for mid-infrared detection.* Journal of Crystal Growth, 2005. **274**(1-2): p. 6-13.

81. Shan, W., et al., *Band anticrossing in GaInNAs alloys.* Physical review letters, 1999. **82**(6): p. 1221-1224.

82. Wu, J., W. Shan, and W. Walukiewicz, *Band anticrossing in highly mismatched III–V semiconductor alloys.* Semiconductor Science and Technology, 2002. **17**: p. 860.

83. Buckle, L., et al., *Growth of dilute GaNSb by plasma-assisted MBE.* Journal of Crystal Growth, 2005. **278**(1-4): p. 188-192.

84. Smith, D. and C. Mailhiot, *Proposal for strained type II superlattice infrared detectors.* Journal of applied physics, 1987. **62**(6): p. 2545-2548.

85. Rogalski, A. and F. Sizov, *Terahertz detectors and focal plane arrays.* Opto-Electronics Review, 2011. **19**(3): p. 346-404.

86. Wu, L., *MBE growth and properties of GaAsSbN/GaAs single quantum well heterostructures*, in *Electrical and Computer Engineering*. 2005, North Carolina A&T State University

87. Nunna, K., *Effects of N incorporation on the properties of GaAsSbN single quantum wells and light emitting devices in the 1.55 micron wavelength region*, in *Electrical and Computer Engineering*. 2007, North Carolina A&T State University.

88. Bharatan, S., *MBE growth of lattice-mattched GaAsSbN/GaAs and InGaAsSbN/GaSb quantum wells for optoelectronic devices*, in *Electrical and Computer Engineering* 2009, North Carolina A&T State University.

89. Yang, M., *Determination of temperature dependence of GaSb absorption edge and its application for transmission thermometry*. J. Appl. Phys., 1999. **85**(9): p. 6632.

90. Bracker, A.S., et al., *Surface reconstruction phase diagrams for InAs, AlSb, and GaSb.* Journal of Crystal Growth, 2000. **220**(4): p. 384-392.

91. Wang, Z., et al., *Quantitative Z-contrast imaging in the scanning transmission electron microscope with size-selected clusters.* Physical Review B, 2011. **84**(7): p. 073408.

92. Abstreiter, G., et al., *Strain-Induced Two-Dimensional Electron Gas in Selectively Doped Si/Si(x)Ge(1-x) Superlattices.* Physical review letters, 1985. **54**(22): p. 2441.

93. Menéndez, J., *Characterization of bulk semiconductors using Raman spectroscopy*, in *Raman Scattering in Materials Science*. 2000, Springer. p. 55-103.

94. Sela, I., et al., *Raman scattering study of InAs/GaInSb strained layer superlattices.* Journal of applied physics, 1991. **70**(10): p. 5608-5614.

95. Lyapin, S., et al., *Raman selection rules for the observation of interface modes in InAs/GaSb superlattices.* Physical review letters, 1995. **74**: p. 3285-3288.

96. Schmitz, J., et al., *Optical and structural investigations of intermixing reactions at the interfaces of InAs/AlSb and InAs/GaSb quantum wells grown by molecular-beam epitaxy.* Journal of Crystal Growth, 1995. **150**: p. 858-862.

97. Bennett, B.R., et al., *Control of interface stoichiometry in InAs/GaSb superlattices grown by molecular beam epitaxy.* Applied physics letters, 1993. **63**(7): p. 949-951.

98. Aoki, K., E. Anastassakis, and M. Cardona, *Dependence of Raman frequencies and scattering intensities on pressure in GaSb, InAs, and InSb semiconductors.* Physical Review B, 1984. **30**(2): p. 681.

99. Khoshakhlagh, A., et al., *Long-wave InAs/GaSb superlattice detectors based on nBn and pin designs.* Quantum Electronics, IEEE Journal of, 2010. **46**(6): p. 959-964.

100. Gautam, N., et al., *Barrier Engineered Infrared Photodetectors Based on Type-II InAs/GaSb Strained Layer Superlattices.* 2013.